EXPERIMENTAL AND ANALYTICAL STUDY ON TWO-PHASE IMPINGEMENT COOLING WITH AND WITHOUT ELECTRIC FIELD

A Dissertation

Presented to

the Faculty of the Graduate School

University of Missouri-Columbia

In Partial Fulfillment of the Requirements for the Degree

Doctor of Philosophy

By

XIN FENG

Dr. James E. Bryan, Dissertation Supervisor

December, 2007

The undersigned, appointed by the Dean of the Graduate School, have

examined the dissertation entitled

EXPERIMENTAL AND ANALYTICAL STUDY ON TWO-PHASE IMPINGEMENT COOLING WITH AND WITHOUT ELECTRIC FIELD

Presented by Xin Feng

A candidate for the degree of Doctor of Philosophy

and hereby certify that in their opinion it is worthy of acceptance

Dr. James E. Bryan

Dr. Robert Tzou

Dr. Scott Kovaleski

Dr. Hongbin Ma

Dr. Yuwen Zhang

Dr. Qingsong Yu

ACKNOWLEDGEMENTS

I sincerely thank Dr. James Bryan, who has served as my research advisor. Thank for your fully support, patience and guidance. I'll remember those days and nights in which we work together.

I wish to thank Dr. Robert Tzou, Dr. Hongbin Ma, Dr. Yuwen Zhang, Dr. Qingsong Yu and Dr. Scott Kovaleski who served as my dissertation committee member and provided incisive remarks and suggestions.

I wish to thank Brian Samuels and Joshua Hensley who provide me tremendous help on experiment design and manufacture processes.

This research has been kindly supported by grants from the Office of Naval Research (ONR).

Finally, I want to thank my parents for your foresight education since my childhood. Thank for, my wife, Yamin Luo. This work could not be completed without her support and love.

TABLE OF CONTENTS

LIST OF TABLES

LIST OF FIGURES

LIST OF SYMBOLS

A	Area	
A_s	Area of heating surface	
Bo	Bond number	$Bo_d = \frac{\rho_l g d^2}{\sigma}$
C	Constant	
D	Diameter of heating surface	
d	jet diameter	
d_i	inner diameter of nozzle	
d_o	outside diameter of nozzle	
E	Electric field intensity	
F	Area percentage of regime 1 on the whole surface	
f	Force	
Fr	Froude number	$Fr_\delta = \frac{u_\delta}{\sqrt{g \cdot \delta}}$
Fe	Nondimensional charge mobility	$F_E = \frac{f k_i}{\varepsilon}\left(\frac{\rho}{\varepsilon_0}\right)^{1/2}$
g	Gravity constant	
H	Distance from EHD nozzle tip to ground plane	
h	Heat transfer coefficient	
h_0	Average heat transfer coefficient without EHDA enhancement	
h_E	Average heat transfer coefficient with EHDA enhancement	

h_{fg}	Latent heat	
I	Current	
K	Thermal conductivity	
K_{el}	Liquid electric conductivity	
k	wave number	
ki	the electrical mobility of the ions forming the cone jet spray charge	
L	Characteristic length of heating surface	
M	Properties	
N	Number of micro jets	
Nu	Nussult Number	
P	Pressure	
P_J	Jet array pattern	
Pr	Prandtl number	
Q	Volume flowrate	
q	Heat or power	
q”	Heat flux	
R	Thermal Resistance	
Re	Reynolds number	$\mathrm{Re}_d = \frac{u_e \cdot d}{\upsilon}$
r	Radius	
T	Temperature	
t	time	

t_0	Time scale	$t_0 = \sqrt{\dfrac{\rho r_0^3}{\sigma}}$
U	Velocity	
V	Applied voltage	
W_J	Distance between impinging jets	
We	Weber number	$We_d = \dfrac{\rho_l u_l^2 d}{\sigma}$
X	Final nondimensional parameter of hydraulic effect	
Y	Final nondimensional parameter of electric effect	
z	Vertical distance above the testing surface during jet impingement	

Greek symbols

Γ_0	Taylor number	$\Gamma_0 = \dfrac{\varepsilon_0 A E_{n0}^2}{2\sigma}$
Π_μ	Nondimensional Liquid properties	$\Pi_\mu = (\sigma^2 \rho_l t_e)^{1/3} / \mu$
Φ	Nondimensional Critical Heat Flux	
α	The fraction of liquid converted into droplets	
α_s	EHD spray angle	
β	Electric susceptibility	
ε_0	Electric constant	
γ	Density ratio between liquid density and vapor density	
λ_H	the Helmholtz critical wavelength	
δ	Liquid thickness of the wall jet	
δ_c	Liquid sublayer	

δ_m	The mean liquid film thickness over the heating surface.
ξ	Nondimensional current $\xi = I / \sigma(\varepsilon_0 / \rho_l)^{1/2}$
μ	Dynamic viscosity
ν	Kinetic viscosity
η	Nondimensional flowrate $\eta = \left(\rho_l KQ / \sigma\varepsilon\varepsilon_0\right)^{1/2}$
ρ	Density
σ	Surface tension
σ_e	Surface charge density
σ_0	Surface charge density $\sigma_0 = \sqrt{\frac{\sigma\varepsilon_0}{r_0}}$
ν^*	Nondimensional viscosity $\nu^* = \sqrt{\frac{\rho\nu^2}{\sigma r_0}}$
τ_e	Electrical relaxation time

Subscripts

A1	Regime 1 in micro jet impingement cooling
A2	Regime 2 in micro jet impingement cooling
b	Boundary between region 1 and region 2
bl	Boundary layer reaching the top of liquid film
bu	Vapor bubble at CHF condition
le	Exiting jet from the nozzle
ef	Heat transfer effective region of a bubble at CHF condition
CHF	Critical heat flux

Cond 1	Inlet temperature of Condenser 1
Cond 2	Inlet temperature of Condenser 2
Cou	Coulomb force
Copper	copper heat sink or copper coupon
DEP	Dielectrophoretic force
e	Liquid exiting velocity at nozzle tip
E	Electric properties
Fe	Feeding liquid via nozzle
gra	Gravity force
i	Inside diameter
J	Jet
l	liquid
L	Characteristic length for multi micro jet impingement cooling
m	Maximum velocity in the velocity profile of the wall jet
m1	Region 1 in the CHF model of multi micro jet impingement cooling
m2	Region 2 in the CHF model of multi micro jet impingement cooling
mom	Momentum force
ml	Liquid momentum force
ms	Maximum heat flux by saturation incoming flow
mv	Vapor momentum force
n	Normal orientation
o	Outside diameter

pat	Cooling pattern (Free surface jet or submerged jet et al.)
s	Surface tension
s1	Region 1 in the CHF model of single micro jet impingement cooling
s2	Region 2 in the CHF model of single micro jet impingement cooling
sat	Saturation
sub	Subcooling fluid
sur	Surface tension force
v	Vapor
VM	Monde’s V-Correlation for multi jet impingement cooling
vis	Viscous force
W	Surface temperature
WB	Temperature inside the copper coupon

ABSTACT

The power electronics elements of the next generation would dissipation much high heat flux. Among their thermal management solutions, two-phase jet impingement cooling and spray impingement cooling are two promising methods. Due to the mechanism of generating spray and jet, it is hard to compare those two methods in the consistent conditions. In the first part of this study, electrohydrodynamic atomization (EHDA) method is used to generate spray from the same capillary, from which the jet could be generated either, so that two different impingement cooling methods could be compared in the consistent conditions.

Before the experiment of EHDA impingement cooling, 14 EHDA modes are classified in the testing range with ethanol. Two nondimensional parameters are developed, in order to clearly lay out 11 EHDA modes within the EHDA mode map.

Experiments of EHDA impingement cooling are conducted in various nozzles and conditions. It is found that the EHDA cooling could enhance the heat transfer coefficient in most conditions. As the CHF, EHDA cooling has little benefit. The electric repulse force causes the wide spray angle, which could reduce the CHF by losing certain amount of impingement flux, no matter with single or multi EHDA impingement cooling.

In the second part of this study, single and multi micro jet impingement cooling (MJIC) are investigated with three kinds of fluids and three types of microjet nozzles. The

experimental results indicate that the existing CHF correlations could not predict experiment data of single MJIC. Based on experimental observation and theoretical analysis, a semi-theoretical CHF mode is proposed that divided the whole surface into two characteristic regimes. The experimental results of water and ethanol are coincided with the prediction by the new CHF correlation based on the model. And the CHF prediction process is discussed and presented with purpose of real application. That CHF correlation over predicts the CHF for HFE7000, possible reasons are discussed in the paper. An interesting and unique trend are found in the CHF test for saturated HFE7000 and subcooled ethanol, our new CHF model shows the potential to explain the unique feature.

Three CHF correlations with the CHF experiments results for the multi MJIC. Monde's V-correlation and the semi-theoretical CHF correlation could not predict very well. The correlation obtained by data regression, works better than the other two. The experimental results show that the heat transfer enhancement by multi MJIC depends on fluids and testing conditions. This approach normally could achieve high CHF at same Re number, but at same flowrate. It might cause negative, neutral and positive effect on water, ethanol and HFE7000, respectively. The heat transfer coefficient could be improved by using multi MJIC with water. However, in case of MJIC with ethanol and HFE7000, multi MJIC shows very little advantages over the single MJIC.

INTRODUCTION

As the technologies developing, high energy CPU and other power electronics elements are generating more significant concerns on their thermal management. So far the single phase cooling method is typical choice in most cases of thermal management. However, due to the limitation of the single-phase heat transfer and the demands for power electronics with high energy dissipation, technology conflicts seem much serious than before.

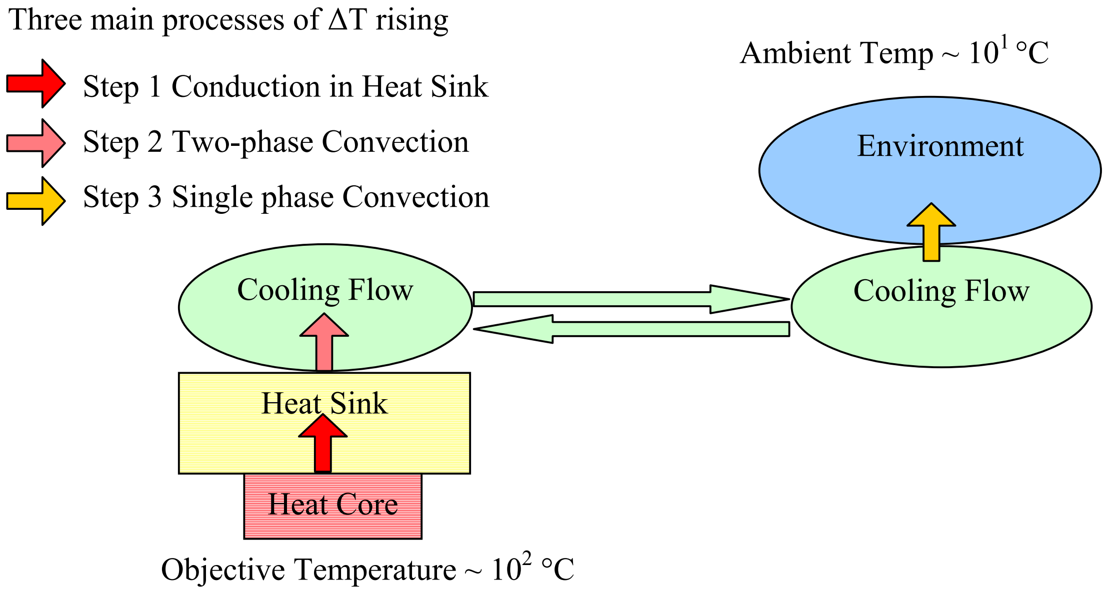

Fig. 1 Heat dissipation sketch of power electronics element

I would like to have an example to remove 1 kW from a power electronic element with the area of 1 cm^2. The restrictions of the process are coming from the temperatures limitations at two ends. One is the maximum temperature of the heat source, which usually is required below 100 °C. The other is the minimum temperature of cooling fluid, which is about room temperature. Then we could divide the process into 3 steps. The heat transfer process is shown in the Fig. 1.

Based on the known properties and parameters, we could calculate the heat transfer processes by following equations.

$$Q = A_{chip} \cdot q''_{chip} = A_{HS} \cdot \frac{K_{copper}}{\delta_{copper}} \cdot \Delta T_{HS} = A_f \cdot h_f \cdot \Delta T_f = A_a \cdot h_a \cdot \Delta T_a \tag{9.1}$$

Some simple calculation results are shown in Table 1, according to the heat transfer coefficient summarized by I. Mudawar [1] in the Fig. 2.

Table 1 Heat Dissipation Process for q = 10^3 W, S = 1 cm^2

	Step 1	Step 2	Step 3
q" (W/m^2)	10^7	10^6	10^4
S (m^2)	10^{-4}	10^{-3}	10^{-1}
Δ T (ºC)	10^1	10^1	10^1
R (K·m^2/W)	10^{-6}	10^{-5}	10^{-3}
h (W /K·m^2)	NA	10^5	10^3
δ_{copper} (m)	10^{-3}	NA	NA

Now we could find one problem in the example, which is different from the current thermal management problems. We find that there is substantial temperature drop inside the copper heat sink. That means people would no long treat this kind of problem as before. For an instance, people had used the heat sink with the length of couple centimeter, to reduce the heat flux density to one or two order of magnitude less within acceptable ΔT. However, for the thermal problems with high flux density up to 10^7 W/cm^2, the copper heat sink could not thicker than 1 mm if people want to control the temperature rising under 30°C. That requirement means at least two opportunities to improve the cooling process. One is better design for heat sink at 1mm level with purpose of reducing heat flux density. The other is to enhance the heat transfer processes at step 2, which might be a better design for two-phase cooling above the heat sink.

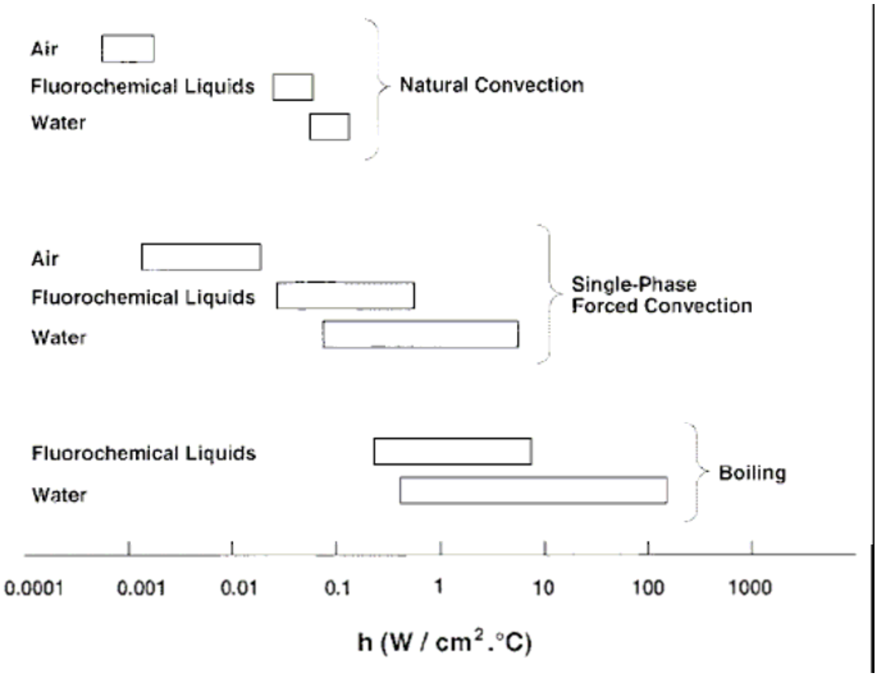

Fig. 2 Heat transfer coefficients attainable with different cooling methods [1]

In the present study, we plan to explore the two-phase impingement cooling with and without electric field. In the first part, we would use EHDA method to compare the spray and jet cooling. In the second part we plan to investigate the single and multi micro jet impingement cooling (MJIC), in which the jet diameter is 1 order of magnitude lower than the traditional jet studied in the past. A semi-theoretical CHF correlation would be developed to predict the CHF in single MJIC. The content of this work would have two parts and 5 sections. The organization chart is shown in Fig. 3.

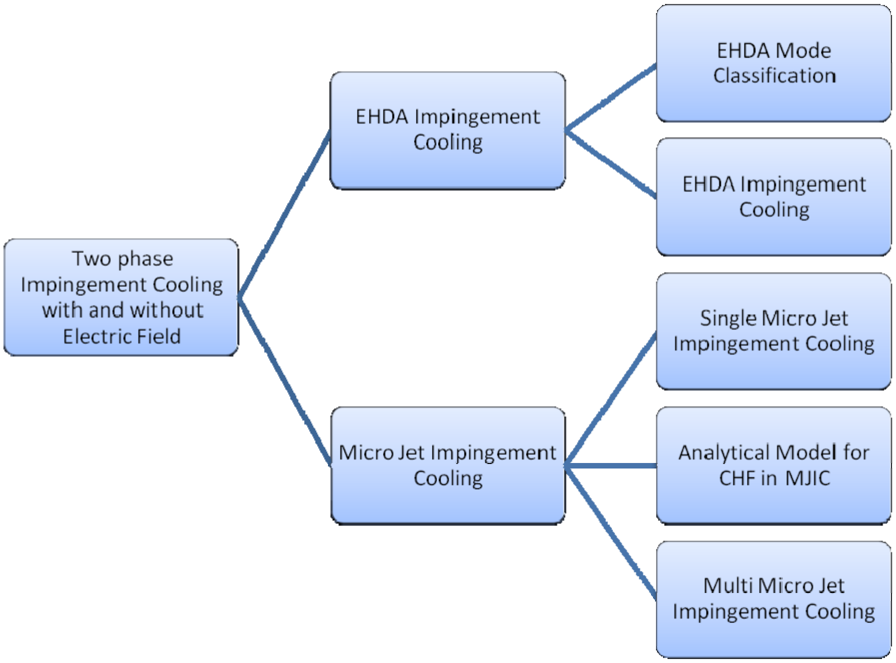

Fig. 3 Organization chart of this study

OBJECTIVES

I have following objectives in this study

1. Improve classification of EHDA modes. This will be accomplished by experimental observation and force analysis for EHDA tests.
2. Investigate the effect of EHDA on two-phase impingement heat transfer. The effect would be shown in the comparison of the heat transfer coefficient and CHF.
3. Experimental investigate micro jet two-phase impingement cooling. The existing CHF correlations would be verified.
4. Develop a CHF for micro jet two-phase impingement cooling. The results and challenges would be discussed.
5. Investigate the effect of multi micro jets two-phase impingement cooling. Available CHF correlations would be used to study the feasibility of prediction.

PART I. EHDA IMPINGEMENT COOLING

CHAPTER 1. LITERATURE REVIEW OF EHDA IMPINGEMENT COOLING

In the chapter, we would answer the question why we plan to investigate the impingement cooling with electric field. Literature reviews would cover the works about two-phase impingement cooling and fundamental of electrohydrodynamic atomization (EHDA) method.

First we would describe the process of two-phase impingement cooling. During the impingement cooling, nucleate boiling would occur (onset of nucleate boiling: ONB) by increasing the heat flux, and then dominate the surface (Fully nucleate boiling: FNB) until the surface dry-out and critical heat flux (CHF) finally occurs. There are two important parameters to describe the cooling performance. One is the CHF, and the other is the heat transfer coefficient (h). The CHF is used to evaluate the upper limitation of heat flux. After reaching CHF condition, the surface will experience a fast dynamic process, in which the surface would dry out and jump to an extremely high temperature. Sometimes the CHF condition is called as DNB (departure of nucleate boiling) or burnout. Other people had argued about this term decades ago. For example, As G. F. Hewitt had written in his book [2], "*The CHF is confusing since the phenomenon is not associated with a particular critical flux. The DNB is actually incorrect because, in a large number of cases, nucleate boiling is actually suppressed well before the burnout point*". Using dryout in the book, he was still waiting for a better term to describe that specific condition. In this study, we choose CHF since most researchers use this term in the recent literatures.

The heat transfer coefficient is about the thermal resistance or wall superheat between the surface and impinging liquid. And it also determines the temperature difference (wall superheat) with a constant heat flux. Those two parameters would be influenced by operation condition, fluid properties, test configuration and surface condition. Those factors could be expressed in the equation(10.1).

$$\begin{pmatrix} q'' \\ h \end{pmatrix} = f \begin{bmatrix} \left(Q, T_{Sub}, P_{Sat}, M_{Pat}\right), \\ \left(\sigma, \mu_l, \rho_l, H_{fg}, K_l, \rho_v, \mu_v\right), \\ \left(D_i, D_o, M_{jet}, Num\right), \\ \left(D_{Sur}, W_{Sur}, \theta\right) \end{bmatrix} \tag{10.1}$$

In the equation above, we could find impingement pattern is one parameter could affect the heat transfer performance. In the following section, we will review the heat transfer processes with two impingement pattern, free boundary jet impingement and spray impingement in section 1.1 and 1.2. After that, we would show the past works on comparison of jet and spray cooling in Section 1.3. Finally we introduce the EHDA methods in Section 1.4.

1.1 Two-phase Jet Cooling Reviews

Liquid jet impingement cooling is one of the simple and effective way to cooling the objects. Plenty of works had been done from last century, including single phase and two-phase jet impingement cooling [3-6]. Most application backgrounds were related with steel industry and nuclear engineering. The two-phase jet impingement cooling is extremely nonlinear and complex. Therefore, a large number studies were based on experiments. Now a few of CFD researchers are able to simulate some two-phase process correctly, such as a single droplet drying on a dry surface, or a single bubble growing below a liquid film. However, the real impingement cooling is composted by numerous dynamic processes of droplet and bubbles, and those processes are also coupled with the upstream flow. So that numerical simulation could not completely reveal the actual boiling process in a large scale. So far most of works on two-phase jet impingement cooling still based on experimental observation, data and correlations.

1.1.1 Classification of two-phase jet impingement cooling

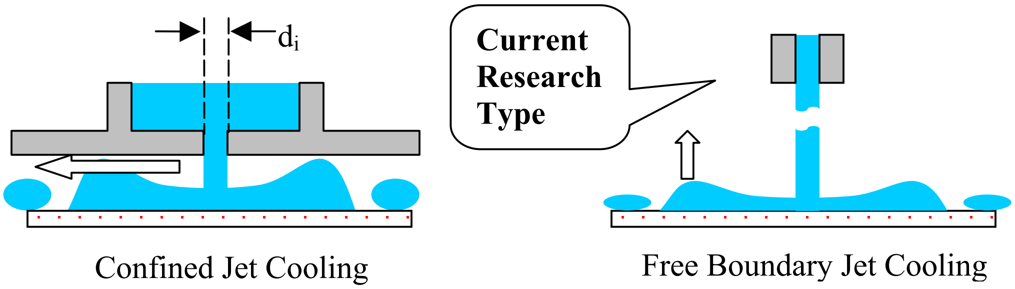

Fig. 4 Sketch of impingement cooling by confined jet and free boundary jet

As to the jet impingement configuration, D.H. Wolf et al. classified into five categories in their reviews of two-phase jet impingement [4]. Those are free surface, jet plunging jet, confined jet, submerged jet and wall jet. Other people also could be classified into two. One is confined jet and submerged jet, and the other is free surface jet. The two types of jet cooling are illustrated in the Fig. 4. Since they have different configures, their heat transfer performance could be quite different in the two-phase cooling. For example, the vapor bubbles could be released easily by the free surface jet, while they are restricted in confined jet and submerged jet. In present study, we will focus on the free boundary jet cooling. Without further notification, jet impingement cooling would be referred to free boundary impingement cooling.

The two-phase jet impingement cooling also had been divided by the size of heating zone [7], which has been illustrated in the Fig. 5. When the characteristic dimension of heating zone is close to the impinging jet diameter, the cooling process is accomplished in the stagnant zone. The highest records of CHF have been reported by using this kind of jet cooling [8, 9]. However the efficiency of that type of cooling is very low, less than 0.01% liquid is evaporated.

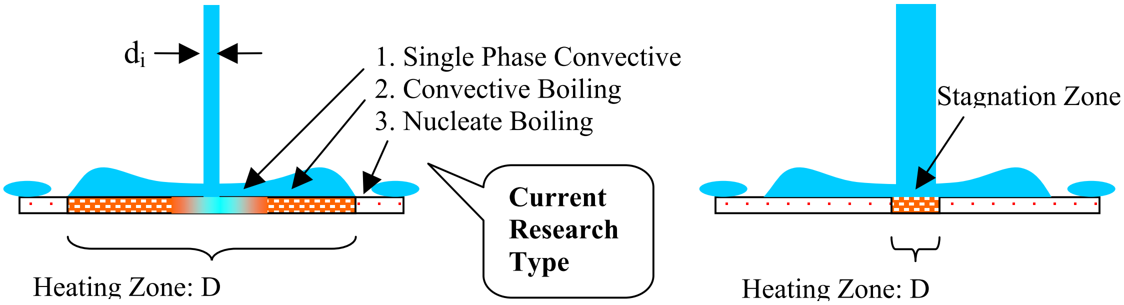

Fig. 5 Sketch of impingement cooling on different heating surfaces

In the present study, we choose and study the free boundary jet to impinge on relative large heating zone. Without further notification, the impingement spot is located at the center for the single jet cooling.

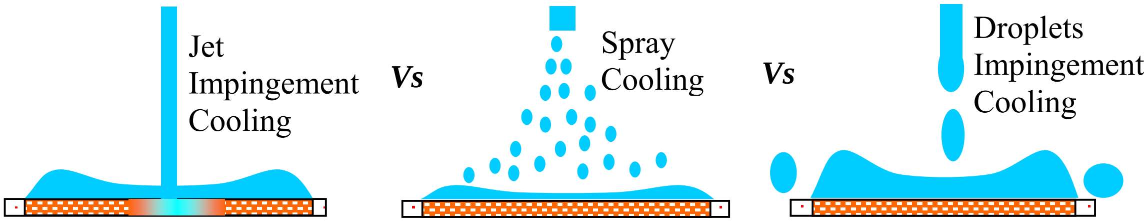

Fig. 6 Sketch of jet impingement cooling vs. spray cooling vs. droplets impingement cooling

In the Fig. 6, three types of impingement patterns are illustrated. They are study topics in the first part of this work. The heat transfer performance between jet impingement cooling, spray cooling, which includes the transition type, droplets impingement cooling. The reviews about experimental and analytical works on jet impingement cooling, would be presented in the second part of this dissertation, in which micro jet impingement cooling (MJIC) would be investigated.

1.2 Two-phase Spray Cooling Reviews

Two-phase spray cooling has been employed in the quenching of metals for a long time. In that condition, the bulk liquid cannot wet the surface above Leidenfrost temperature, while the spray droplets can tough the surface by their momentum. Most of recent studies are related to electronic cooling [10-16].

According to the methods to breakup liquid, sprays processes usually could be classified into pressure sprays and gas assisted sprays. Pressure sprays are formed by supplying liquid at high pressure through a small orifice; while gas assisted sprays employ a high-pressure gas (air or vapor) to assist the liquid breakup. Despite gas assisted sprays has high cooling performance in open environment, they are difficult to incorporate in a closed loop cooling system because the secondary gas would drastically reduce the condenser efficiency.

The recent researches on spray cooling are related to electronics cooling, which focus on the nucleate boiling rather than the film boiling in quenching process. K. A. Estes and I. Mudawar [10] developed a CHF correlation for the pressure spray cooling, in terms of Sauter mean diameter (SMD) based on their testing data. In their testing, the droplet sizes are range from 100μm to several hundred μm by different fluids. And they concluded that the small droplets diameters can increase the value of CHF. J. R. Rybicki and I. Mudawar tested the surface orientation with PF5052 [12]. According to their results, the CHF correlation previously developed for downward oriented spray was equally successful at predicting the upward oriented spray. The spray orientation showed no measurable influence on either single phase or two-phase cooling.

L. C. Chow and his co-workers did many experimental works on spray cooling [15-19]. They believed that heat transfer mechanisms in spray cooling are consisting of three key mechanisms [15]: nucleate boiling due to surfaces and secondary nuclei, convective heat transfer, and direct evaporation from the surface of the liquid film. And they also ranked the dominant factors in spray cooling [17]. The mean droplet velocity had the most dominant effect on CHF and the heat transfer coefficient. The second factor is the mean droplet flux. The Sauter mean diameter did not appear to have an effect on CHF in their tests. They also found a dilute spray with large droplet velocities appears to be more effective in increasing CHF than a denser spray with lower velocities for a given droplet flux. And the mass flow rate was not a controlling parameter of CHF. Some of their conclusions did not agree with other people proposed [10, 11, 15, 17].

1.3 Past Works on Comparison of Two-phase Spray and Jet Cooling

Spray and free surface jet cooling are often considered competing options for electronic cooling. During the spray process, the liquid breaks up into fine droplets which impinge individually upon the heated wall. The droplet impingement both enhances the spatial uniformity of heat removal and delays the liquid separation from the wall during vigorous boiling. Despite these advantages, sprays have not gained popularity in electronic cooling because the intricate flow features within spray nozzle increase the likelihood of clogging. Furthermore, spray nozzles require careful periodic testing to ensure predictable and repeatable impact pattern. Even seemingly identical nozzles from the same production batch often fail to produce identical spray patterns.

On the other hand, jet impingement cooling device could be very simple and robust. And the highest record of CHF is obtained with jet impingement cooing. However, one disadvantage of jet impingement cooling is the concentration of heat removal within the impingement zone causes relatively large temperature gradients within the cooled device. Jet impingement cooling is also prone to separation of the wall liquid layer emanating from the impingement zone during vigorous boiling.

C. Cho and K. Wu did their test with R113 and found the same level of CHF for both methods, while the spray cooling has better and uniform temperature distribution [20].

K. Estes and I. Mudawar compared three types of slot jets created by small orifice and three types of industrial nozzles (Spraying System Unijet full cone series) with different spray angle [21]. They found that the spray and jet cooling depend on liquid subcooling. Spray and jet impingement cooling have comparable CHF at high subcooling with FC-72, and at low subcooling due to weak attachment of liquid film, spray cooling is better than jet.

M. Fabbri et al. tested an industrial nozzle (HAGO DFN-B100) and an array of micro jet (0.14mm) on a 0.5 cm^2 surface [22]. Their results showed that micro jet array required less pumping power per unit of power removed. The heat transfer coefficient of micro jet array is better than that with HAGO nozzle at same pump head. However, at same flowrate, the HAGO nozzle is better at heat transfer coefficient.

All those comparison between jets and spray were conducted with different nozzles, therefore the flowrate would be different at same pressure head. And as to the spray nozzles, the spray droplet diameter and velocity are coupled with the pressure. So it is difficult to make a comparison between spray and jet impingement cooling. To do a good comparison, it is needed to generate spray and jet by same level of parameters, including pressure drop, flowrate, and flow exiting area and so on. That means, the desirable situation to compare the spray and jet cooling is to create the spray and jet by same capillary, and compare them in same testing environment.

In order to clarify those questions, we are going to introduce a new spray method for spray cooling, electrohydrodynamic atomization (EHDA), sometimes called electrostatic spray.

1.4 EHDA Reviews

The phenomenon of EHDA was first found by J. Zenely [23]. He found the phenomena by applying an external electrical field in a dielectric flow. Many experimental and analytical studies had been carried out in the last century [24-29]. J.B. Fenn won the Nobel prize for his contribution in mass spectrometry, where he used electrospray ionization technique (EHDA) to break biological macromolecules [24].

A typical EHDA apparatus is a point-plane (Orifice-Plane) structure. During typical testing, dielectrical liquid is driven through an orifice and be charged by an electronode. Since the point-plane configuration would create a large gradient electrical field, different EHD free boundary flow behaviors would generated during the process of the flow reaching the ground plane. Those EHD flow behaviors are named as EHDA in this study, including EHD dropping, EHD jet, EHD spray, et al.

The EHDA method could generate spray by a capillary, which enable to switch between jet and spray controllably. Some benefits and challenges by using EHDA method to compare spray and jet impingement cooling are listed in the Fig. 6 and Table 2.

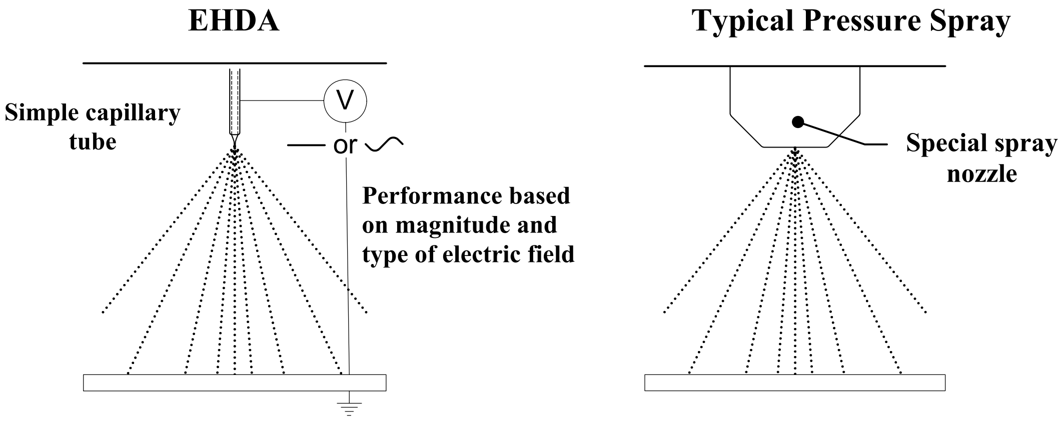

Fig. 7 Sketch of EHDA and typical pressure spray

Table 2 The benefits and challenges by using EHDA in stead of traditional spray

	EHDA	**Typical pressure spray**
Benefits	Low pressure	High pressure
	Controllable modes from dripping to jet to spray	Nozzle to nozzle variation
	Flow rate and spray controlled independently	Coupled flow rate and drop size for given nozzle
Challenges	Working flowrate just meet the limitation for electronics cooling	Surface is likely overflowed
	High voltage source required (typically $10^3 \sim 10^4$V)	No voltage source required
	Low droplets momentum	High droplets momentum

People had observed EHDA phenomena with different fluids. For example, J.M. Grace and J.C.M. Marijnissen had reviewed the past works on EHDA, and they listed over 50 types of fluids in a table of EHDA fluids [29]. In the present study, considering the properties requirement for electronics cooling, we had tried three types of fluids, such as water, ethanol and HFE7000. After we get the preliminary results, (see Appendix A), we choose ethanol as our working fluid for EHDA mode classification and impingement cooling. So we review past EHDA studies with ethanol and list their main testing conditions in the following chart, with comparison of our testing range.

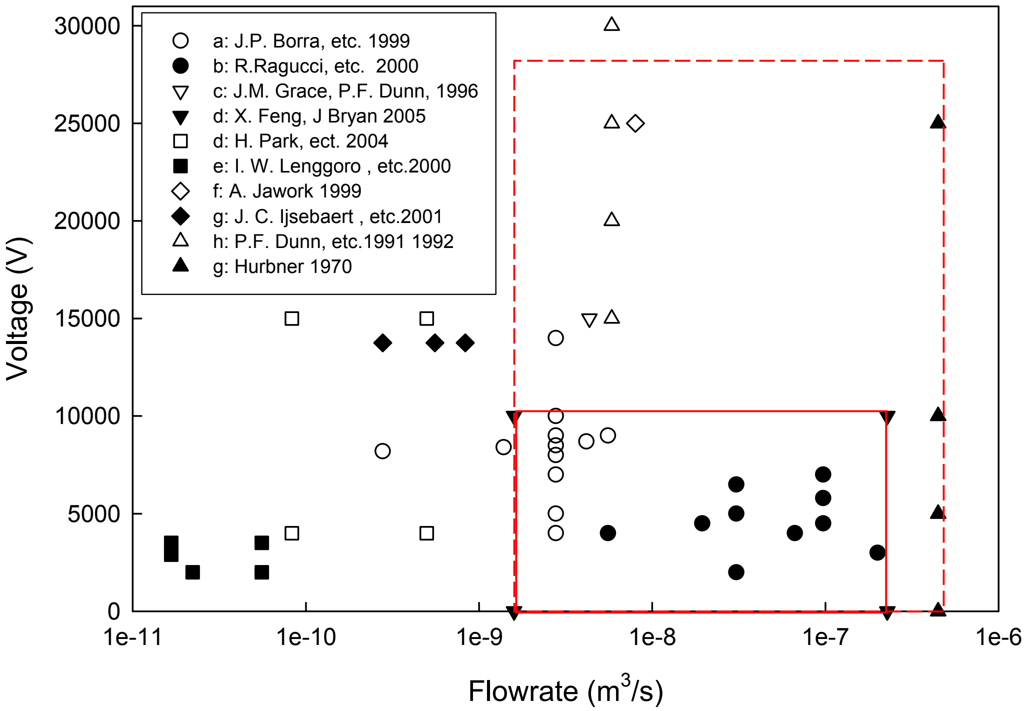

Fig. 8 Former studies of EHD free boundary flow of Ethanol (a-g: [30-40])
(Our Testing Range during EHDA mode classification —— Our Testing Capability – – –)

1.4.1 EHDA mode classification

The EHDA flow patterns or EHDA modes could be changed dramatically under various testing conditions. The EHDA modes could be affected by many parameters, some of which are listed in the equation(10.2).

$$EHDA_{\mathrm{mode}} = f\left[\left(V,Q,H\right),\left(\sigma,\mu,\rho_l,K_l,\varepsilon_l,\rho_v,K_v,\varepsilon_v\right),\left(D_i,D_o,M_{Jet}\right)\right] \tag{10.2}$$

G. I. Tayler 1964 first demonstrated the theoretical analysis of liquid meniscus of Cone Jet Spray mode [28]. After that people usually call that mode as Taylor Cone Jet mode or Taylor Cone Spray Mode. So far most of researches are still focusing on this mode.

In 1994, M. Cloupeau and B. Prunet-Foch summarized their observation classified 6 modes based on water and various organic products [41]. They sketched the flow behavior for each mode and compare their definition with other people observation. All of the most stable and semi-stable modes were shown in their work. But they had not clearly addressed those unstable modes when they discuss those transient modes.

J.M. Grace and J.C.M. Marijnissen also reviewed the past work and presented a flow chart that described how to get 11 EHDA modes by changing parameters [29]. In their work, some unstable modes were discussed, which were accepted other researcher later. But no images or sketches were presented, so it is difficult to compare their classification with other studies. For example, one mode called DAG mode, which is a unique mode they distinguished from other modes, is not clear without pictures

In 1999 A. Jaworek and A. Krupa demonstrate 10 modes by the static image and a sketch [36]. So far it is the most completed classification for EHDA. Most operating parameters have been reported except for distance between electronodes. Most of the stable and semi stable modes are described clearly, even including some modes generated in the corona. In this study, we would not apply high voltage to create the corona during the experiments. When we observe some new modes, we will try to keep consistent with the former classifications.

Most of past studies were conducted in a certain working range with their application background. That means, most of mode classifications are extracted in limited working conditions. In this study, the EHDA cooling experiment have following requirement due to its research background, electronics cooling.

1. Arcing or discharging need to avoid inside the chamber.
2. The bridging modes are not suitable for cooling.
3. The protection gas is also not allowed in a close system.

CHAPTER 2. EXPERIMENTAL SETUP OF EHDA IMPINGEMENT COOLING SYSTEM

One testing bench is built during the present study, which could be used as two experiment systems. One system is for the EHDA mode classification, and serves for EHDA impingement cooling. The other system is built for the micro jet impingement cooling (MJIC). Two systems share most components, such as pump, plumbing, heat exchanger, testing chamber. In this chapter, we would first introduce the EHDA cooling systems and some key components, such as testing nozzle, heating coupon and surface. The uncertainly analysis and data reduction would be discussed.

2.1 EHDA Cooling Test Setup

The test bench for EHDA experiment is shown in the Fig. 9. There are five function modules on this test bench, which is listed in the Table 3.

Table 3 The Experiment Module in the EHDA testing

Module	Component
Liquid Supply	Pump
	Flowmeter
	Testing chamber
High Voltage Supply	Oscilloscope
	Function generator
	High voltage power supplier
Heating Source	Heating power supplier
	Heater
Cooling Source	Condenser
	In-line heater exchanger
	Chiller
Observation & Measurement	High speed camera
	Microscope
	High frequency light
	Data acquisition system

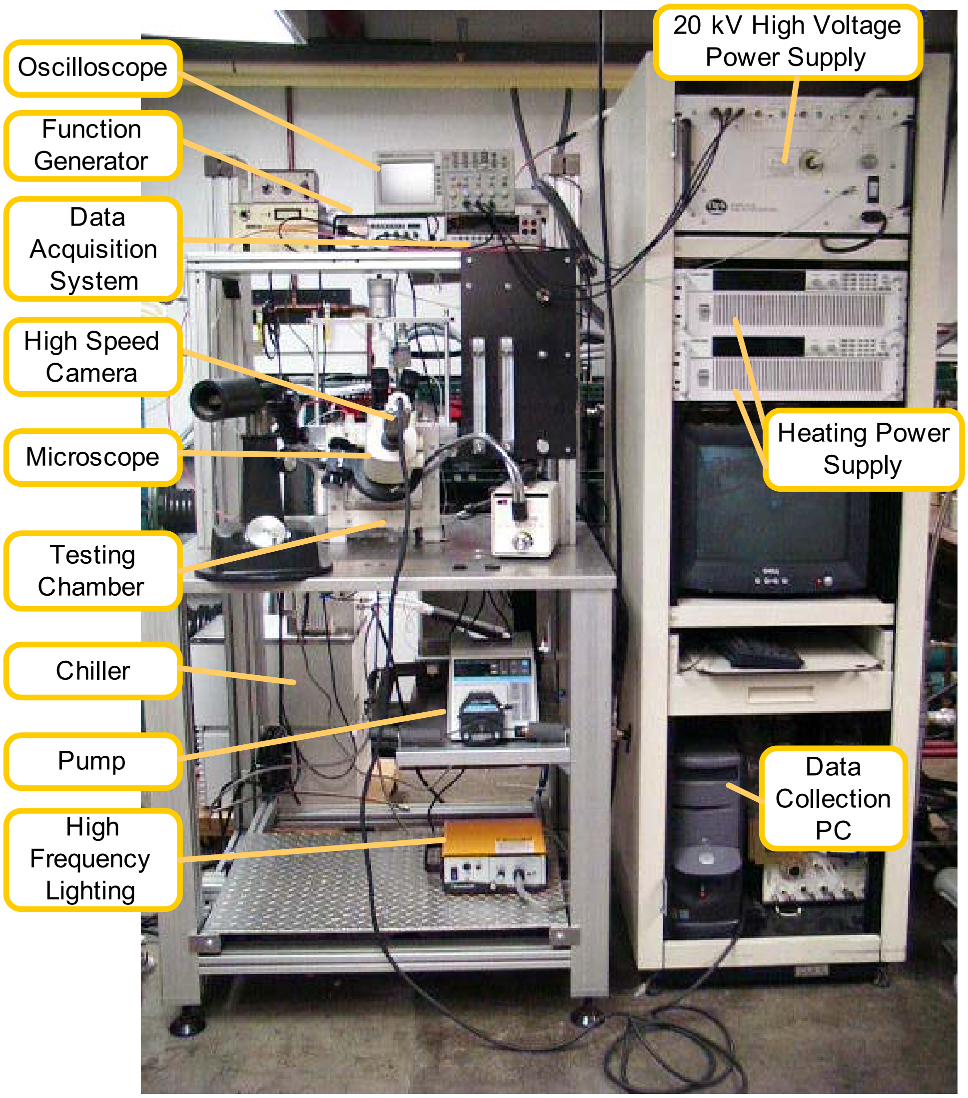

Fig. 9 Photo of the test bench for two-phase EHDA impingement cooling

In the experiment, the EHDA modes are observed in a point-plane configuration. That means the nozzle was linked to the high voltage power supplier, and testing surface is grounded. The details of testing chamber are shows in the Fig. 10. The test setup and flow path is shown in Fig. 11. During the test, a squeezing pump drives the testing liquid to passes the flow-meter. After the liquid entering the nozzle house, it would be charged by an electrode then exiting the nozzle. The liquid flow would be deformed and hit the ground plane in the electrical field. During the cooling test, part of the liquid would become the vapor. And it would be condensed into liquid and collected inside the chamber.

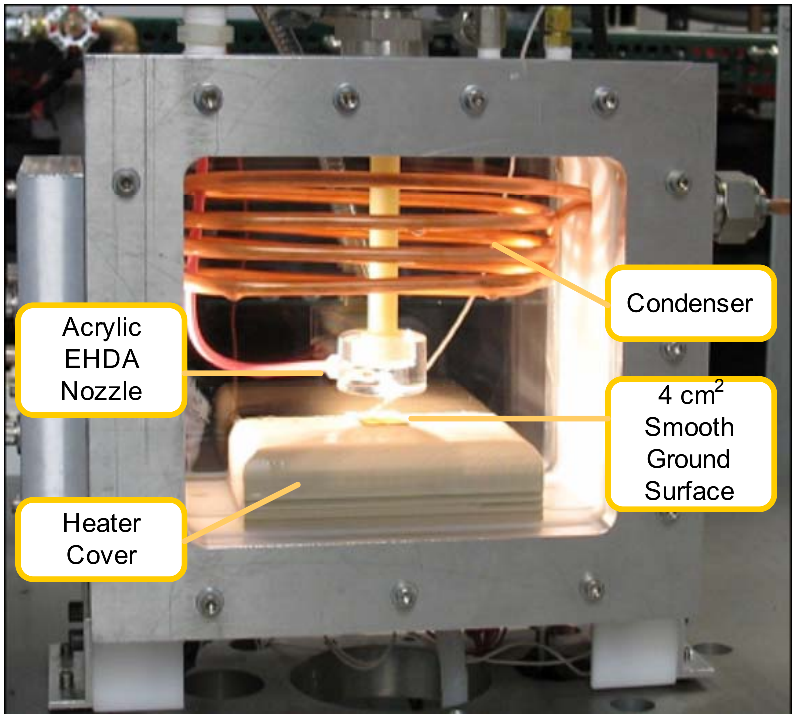

Fig. 10 Photo of the spray chamber for EHDA impingement cooling

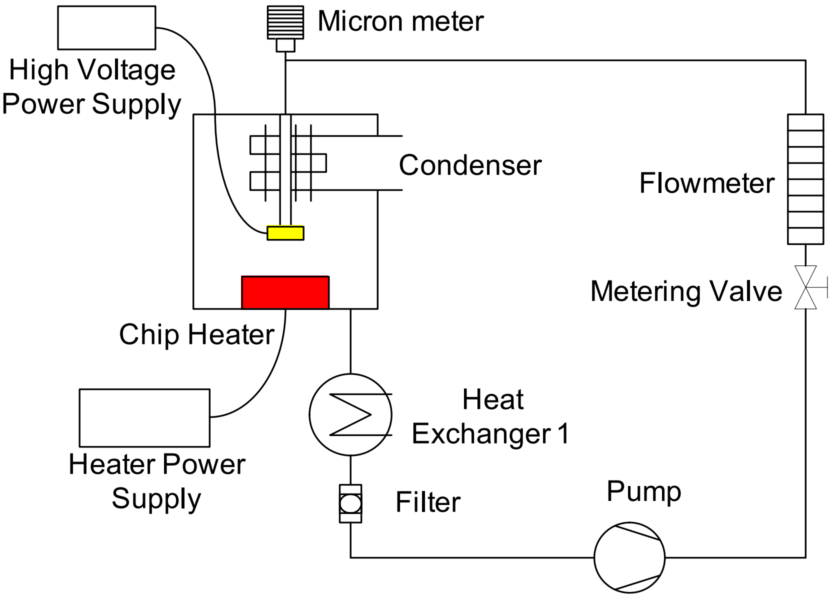

Fig. 11 Sketch of EHDA impingement cooling system

During the testing, N_2 gas is induced into the chamber to prevent arcing. The high voltage supply (Bertan 230) provides DC voltage from 0 to 10 kV. The distance from capillary tip to the ground plane, H, is adjusted by the micrometer from 5 to 50 mm.

As the fluid circulating in the loop, the fluid electric conductivity, σ_e, would change during tests. An YSI Model 35 Conductance Meter was used to measure σ_e. After the ethanol filled into the testing system, σ_e of sample would stay at about 5 10^{-5} S/m for more than 24 hours. A high speed digital camera (Fastcam PCI R-2 by Photron) and high frequency lighting source (ELSV-60 by Everest VIT) are used to capture images of the EHDA modes, which are recorded at 60 to 500 frames per second (fps).

2.2 Testing Heater and Surface Setup

During the testing, we develop a method to make the thick film heater for both EHDA cooling and MJIC system. The heater consists of three components, such as copper coupon, film resistor and alloy foil. We first manufactured copper coupons, then use a thin alloy foil (Coining, 1 mil, Au 80 Sn 20) to bond the copper coupon with semi conduct chip heater (Barry Industries, 100 Ω). That process is carried in a vacuum oven with H_2N_2 mixture gas, so that the finishing surface is very shiny (see Fig. 12). Various testing heater coupons and their surfaces are shown in Fig. 13.

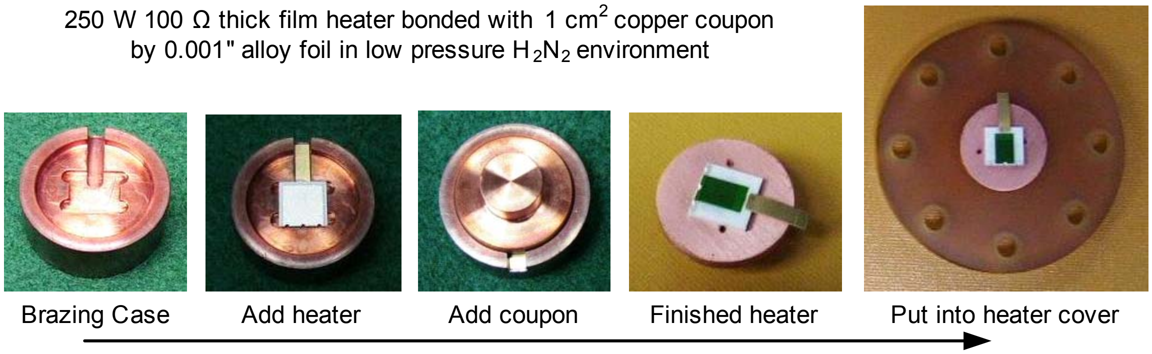

Fig. 12 Manufacture process of thick film resistor heater

0.5 cm^2 smooth surface 1 cm^2 smooth surface 1 cm^2 structure surface 4 cm^2 square surface

Fig. 13 Tested copper coupon in EHDA mode classification and impingement cooling tests

Two slope holes are drilled at the back side of copper coupons, which are used for embedding thermocouples. Since it is possible to generate arc or glow between the electronodes and copper coupon, we choose ungrounded T-type thermocouple to prevent hurting of the data acquisition system. The tips of thermocouples are located on the center line of the copper coupon. The top one is located at 1mm under the surface, and the bottom one is at a distance of 3.7mm.

The copper coupon is covered and held by the PEEK mounting surface and sealed with silicone o-rings. The special plastic material could resist 250ºC. Two kinds of heat cover are made, one is flat cover and the other is 9° slope cover. (See Fig. 14)

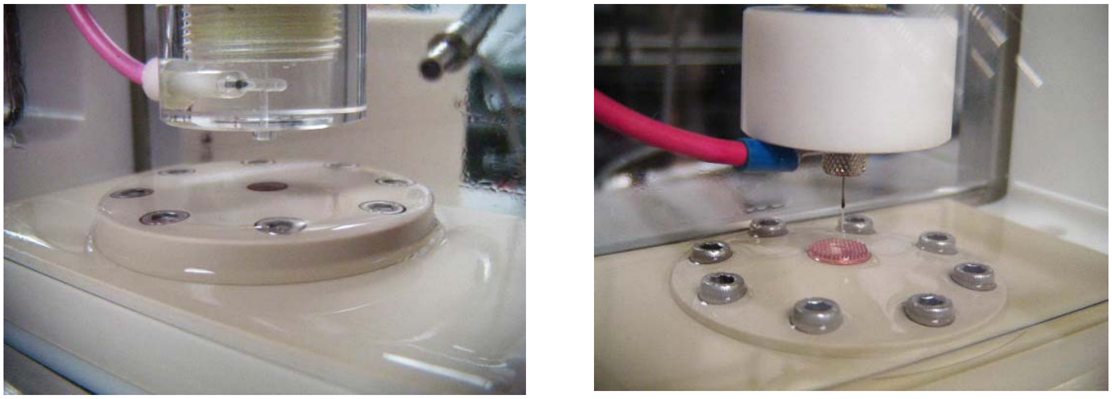

Acrylic nozzle D_i = 1mm, D_o = 4mm
a 0.5 cm^2 smooth surface with flat cover

S.S. nozzle D_i = 0.25mm, D_o = 0.47mm
1 cm^2 structure surface with 9° slope cover

Fig. 14 Photographs showing EHDA nozzles, heater coupon, and mounting surface configurations

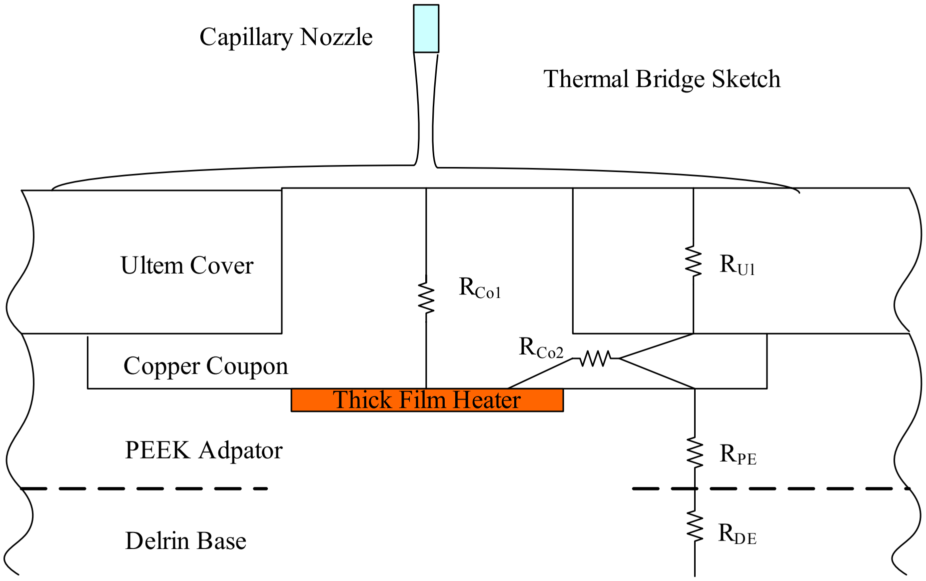

Fig. 15 Thermal bridge sketch of heater coupon and surrounding components

In order to evaluate the heat loss from the thick film heater, it is necessary to analyze the thermal bridge near the testing surface. In Fig. 15, we illustrate the thermal resistance from the heater. And their values are calculated and shown in Table 4.

Table 4 Thermal resistance surrounding the heater

Component	Material	A_S	k	δ	A·R
		cm^2	W/m-K	cm	K/W
Heater Coupon	Copper	1	400	0.86	**0.2**
Heater Cover	ULTEM/PEEK	5.98	0.13	0.55	**71**
Heater Supporter	PEEK	4.57	0.25	1	**88**
Testing Chamber	Delrin	4.57	0.36	4	**243**

According to the thermal resistance table, the thermal bridge through the mounting surfaces had thermal resistance 2 orders of magnitude greater than the resistance from the thick film resistor to the impingement surface. The thermal resistance of impinging flow would depend on the testing condition. At the heat flux condition of 35 W/cm^2, the heat loss did not exceed 2%, and the value would increase with decreasing heat flux. At the heat flux of 5 W/cm^2, the heat loss did not exceed 20%. Therefore we could use the power of heater to determine the heat flux instead of the measured temperature difference within the copper coupon, because the heat loss is low for this type of compact heater.

2.3 Other EHDA Test Setup

EHDA flow loop is design to control the flowrate, applied voltage and the nozzle height. The operational parameters in preliminary test are shown in the Table 5. During the preliminary testing, some interesting phenomena are recorded and shown in Appendix A. In experiments of EHDA mode classification and EHDA impingement cooling, the upper limitation would not be reached (See Table 9).

Table 5 Experimental parameters during EHDA preliminary test

	Operation Parameters			Fluid	Nozzle Type		
	Q (ml/min)	V (kV)	H (cm)		Material	d_i (mm)	d_o (mm)
Min	0.1	0	0.5	Ethanol	Delrin	1	4
Max	20	28	5	HFE7000	Acrylic	0.5	9
				Water	Brass	0.25	0.47
					S. Steel		3

2.3.1 EHDA fluid selection

A great amount of static and dynamic images were captured in thousands of conditions. Keeping the final application in our mind, we could find that ethanol is the best fluid among the three candidates because of the conductivity. Water is so conductive that the severe arcing could happen as low as 6 kV with a height of 1 cm. And many EHDA flow patterns about water are companied with corona. As to HFE7000, it is so dielectric so that we need to apply over 15 kV to change the flow pattern slightly. Though its conductivity might be enhanced by adding additives, in this study, we try to focus our topic on pure fluids. So we are going to show the EHDA modes of ethanol in the following sections. The fluid properties are listed in the Table 6. Some interest EHDA of Water and HFE7000 would be shown in the appendix.

Table 6 Fluid properties at room temperature

Fluid	ρ_l	ρ_v	μ_l	σ	h_{fg}	K_l	K_{el}
	kg/m^3	kg/m^3	μN·s/m^2	N/m	kJ/kg	W/m-K	S/m
Water	997.8	0.019	0.931	0.0726	2450	0.606	1~3 E-4
Ethanol	787.2	0.122	1.156	0.0222	963	0.167	5~8 E-5
HFE7000	1423.2	5.297	0.378	0.0137	28	0.073	<1 E-6

2.3.2 EHDA nozzle setup

We prepare different type nozzles in order to study the effect of d_i, d_o and nozzle material. In preliminary tests, we tried several nozzles with different outside diameters. However, the large outside diameter would not benefit the cooling process. Because the liquid molecules would be repel each other, and flow towards rim at high voltages. That process would waste quite amount of liquid by discharging out of the target surface. As to the nozzle made by S.S. capillary, it has a very small outside diameter. But it is quite difficult to observe and capture the flow structure less than 1mm. Because it needs high resolution camera and lens to capture the images. So the nozzle with D_o = 4 mm is selected for EHDA mode classification.

As to EHDA impingement cooling, we manufactured two types of nozzles. One type of nozzle is made of Acrylic and Delrin. The electronic node is embedded inside the nozzle house. Inside diameter of the nozzles, D_i, are 0.25, 0.5 and 1 mm, outside diameters, D_o, is fixed at 4 mm. The other type of nozzle is made of S.S steel capillary. Commercial capillaries are used to build both single jet and jets array. In the current research, D_i and D_o, is 0.25 and 0.47 mm respectively. Table 7 shows the nozzles that we have tested. The photos of various nozzles are shown in the Fig. 14.

Table 7 Nozzles used in EHDA Impingement Cooling Experiments

Nozzle Type	Jet Number N	D_i (mm)	D_o (mm)	Jet distance W_J (mm)
Single Jet	1	1	4	NA
	1	0.5	4	NA
	1	0.25	4	NA
	1	0.25	0.43	NA
Jet Array	4	0.25	0.43	4.3

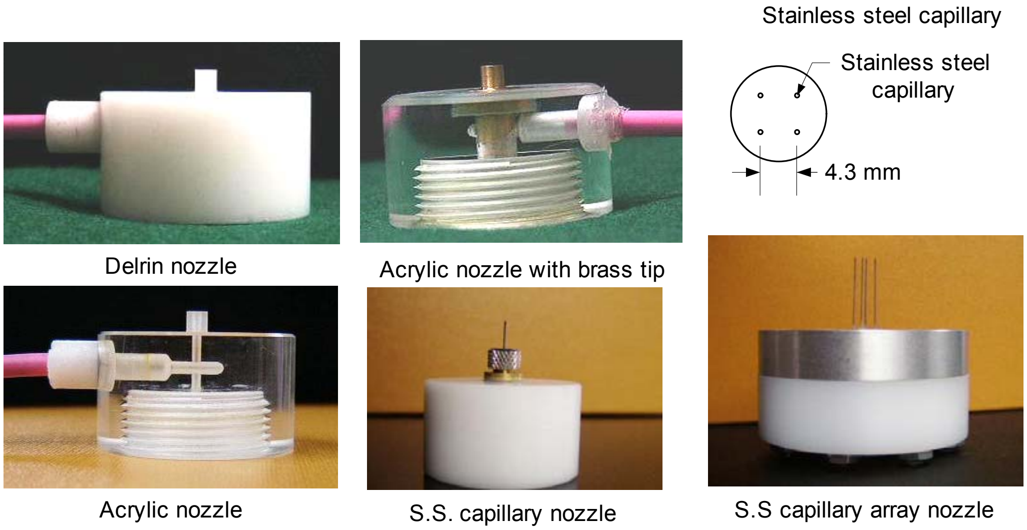

Delrin nozzle

Acrylic nozzle with brass tip

Acrylic nozzle

S.S. capillary nozzle

S.S capillary array nozzle

Fig. 16 EHDA nozzles and their configuration

2.4 Uncertainty and Data Reduction

The periodic pump (Masterflex L/S) provides relative stable flowrate compare with gear pump. According to calibration data, the transient flows disturb is less than 3%. Two

Neslab RTE chillers are hock up with condenser coil and heat exchanger. During the testing process, their uncertainty is about 0.05°C. A digital DC power supply (Xantrex, XDC 150-40) is used to provide constant power output and small derivation (± 0.1 V, ± 0.01A). An absolute pressure sensor (Valihyne, DP-10) is used to measure the chamber pressure. All data for the setup was taken by a Keithley 2701/ExceLINX data acquisition system. A high speed digital camera and high frequency lighting were used to capture the flow structure of the impinging mass and the two-phase heat transfer characteristics.

In order to get the CHF value and heat transfer coefficient, we need to determine the heat flux from the power of heater. The heat flux to the surface is determined as

$$q'' = \frac{W}{A_{TD}} = \frac{V^2}{R \cdot A_{TD}} \tag{11.1}$$

Where: W is the power input by the power supplier.

The resistance of chip heater is about 100 ± 0.5 ohms, and the value would increase slightly as heating. With current supply, the largest error would happen at low heat flux 5 W/cm^2, which 0.89 %, and the error would decrease to 0.28 % as heat flux goes to 50 W/cm^2. During the tests to determine the CHF, the power increment is 1 Watt until it reaching CHF.

After getting the heat flux, the heat transfer coefficient is determined from

$$\bar{h} = \frac{q''}{\left(\bar{T}_s - \bar{T}_i\right)} \tag{11.2}$$

The surface temperature, T_s, was determined from the probe temperature 1 mm beneath the surface. For comparison purposes, the enhanced heat transfer coefficient due to capillary or surface structure was compared to a heat transfer coefficient without any enhancement feature. For the results presented, measurements were obtained once steady state was reached, defined as less than 0.2% temperature change over 5 minutes. However, we found that the surface temperature would oscillate in certain conditions. For example, when the input heat flux approaching the CHF or ONB (onset nucleation boiling), the surface temperature would have large fluctuation. In that kind of condition, we would define the steady state when the average surface temperature within 2 minutes changes less than 0.2%. After we confirm the steady state comes, T_{wb},T_b, T_v, T_i, P_c were measured to get 40 sets of data, which would finally used to calculate the various average temperature.

During the experiment, most tests were carried out in saturated environments with low subcooling temperature (about 5 °C), while a few of tests have high subcooling temperature (about 55°C), in which they were conducted at atmospheric pressure. Before each test, liquid was circulated for at least 10 minutes to eliminate the vapor bubble in the loop. In the meanwhile, we also heat the testing surface to minimize the dissolution gas inside the liquid, especially for water. Typical uncertainties of the three testing fluid are shown in Table 8.

Table 8 Uncertainty values during EHDA impingement cooling with ethanol

Smooth Surface, Jet Array	T_{WB}	T_W	T_e
Average	0.007%	0.008%	0.002%
Maximum	0.021%	0.028%	0.002%
Minimum	0.002%	0.002%	0.002%

Smooth Surface, Single Jet	T_{WB}	T_W	T_e
Average	0.015%	0.015%	0.002%
Maximum	0.163%	0.140%	0.002%
Minimum	0.001%	0.002%	0.002%

Structure Surface	T_{WB}	T_W	T_e
Average	0.053%	0.055%	0.003%
Maximum	0.183%	0.180%	0.004%
Minimum	0.005%	0.005%	0.002%

CHAPTER 3. EHDA MODE CLASSIFICATION AND ANALYSIS

Various EHDA flow patterns could be obtained by changing controllable parameters, such as Q, V, H and d_i. Before investigating EHDA method to impingement cooling, it is necessary to determine the available EHD flow patterns or modes in the testing range. Based on the reviews of EHDA modes, we found the classification of EHDA mode is not well established. Therefore it is needed to identify and classify the EHDA modes for EHDA impingement cooling.

3.1 EHDA Mode Classification

Thousands of videos are recorded during the EHDA experiments with different fluids and nozzles. Some interesting phenomena have not been found in previous literatures. (See Appendix A) With the purpose of investigation of EHDA cooling, we choose ethanol as working fluid (See section 2.3.1). Testing condition is listed in the Table 9.

Table 9 Testing range during EHDA mode classification

	Operation Parameters			
	Q (mL/min)	V (kV)	H (cm)	d_i (mm)
Min	0.1	0	0.5	0.25
Max	14	10	5	1

By analyzing those images, we finally classify those data into 3 categories and 14 modes among 1320 conditions (See Appendix B). Those 14 modes are listed in Table 10 and relative images are shown in Fig. 17 - **Error! Reference source not found.**.

Table 10 Summary of classified EHDA modes

Category	Mode Name	Abbreviation	Observable Frequency
Stable Modes	Jet	J	Negligible Turbulence on the Surface
	Bridging	RJ	Negligible Turbulence on the Surface
	Cone Jet Spray	CJS	Very high Frequency
	Multi Cone Jet Spray	MJS	Very high Frequency
Unstable Modes	Dripping	D	One Low Frequency
	Ramified Jet Spray	RJS	One High Frequency
	Ramified Jet Spray with Cone Jet Spray	MJS+CJS	One Frequency on Each Stream
	Droplet Spray	DS	One High Frequency
	Bridging Dripping	BD	One Low Frequency
	Oscillating Bridging	OB	One Low Frequency
	Spindle	S	One High and One Low Frequencies
	Oscillating Ramified Jet Spray	ORJ	One High and One Low Frequencies
	Oscillating Multi Cone Jet Spray	OMJS	One High and One Low Frequencies
	Oscillating Jet	OJ	One High and One Low Frequencies

The stable modes normally have a stable configure, even the local velocity at certain locations could be very high, such as cone jet spray. There is no obvious wave developing on the free boundary surface. The unstable modes usually have a major frequency, while the transition modes have two observable frequencies. One frequency is relative high and one is relative low. In most of cases, it is suspected that the high frequency wave is caused by electric instability and the low frequency wave is caused by the hydrodynamic instability. Some of the instability analysis would be shown in the Appendix C.

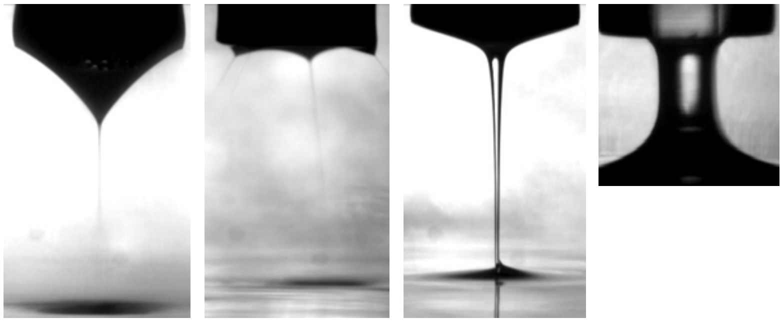

Fig. 17 High speed images of EHDA stable modes

Oscillating Bridging

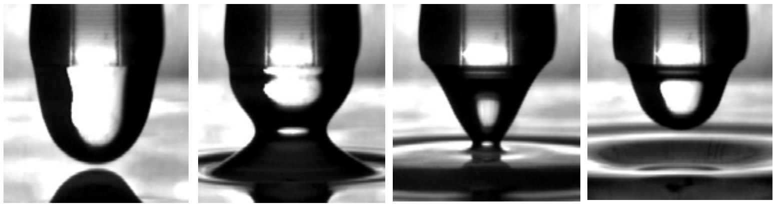

t = 0 t = 12 ms t = 24 ms t = 36 ms

Bridging Dripping

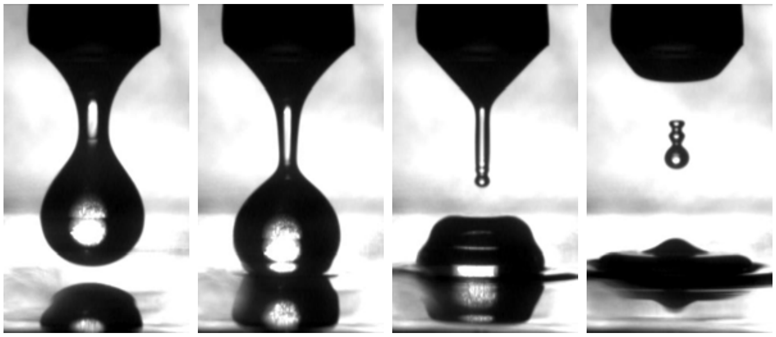

t = 0 ms t = 4 ms t = 6 ms t = 8 ms

Fig. 18 High speed images of EHDA unstable modes: part 1

Dripping

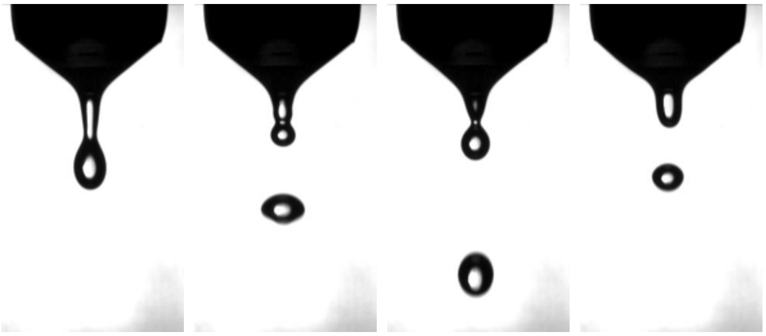

Droplet Spray

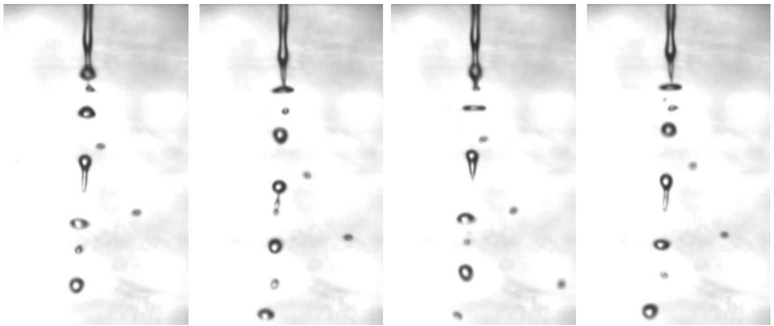

Ramified Jet Spray

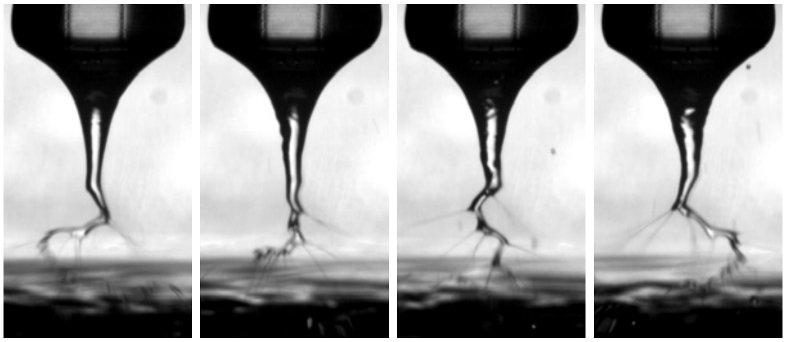

Fig. 19 High speed images of EHDA unstable modes: part 2

Ramified Jet Spray Companied with Cone Jet Spray

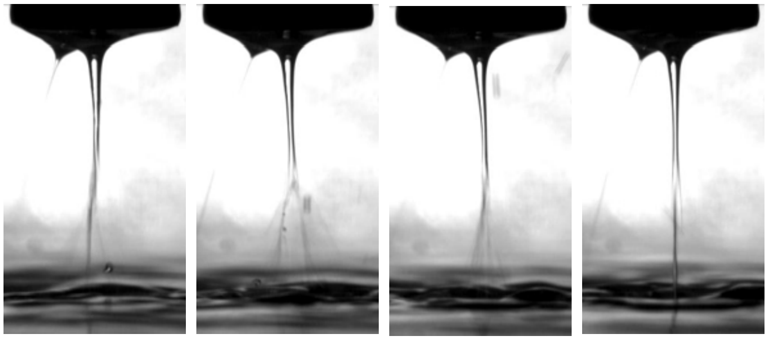

t = 0 t = 2 ms t = 4 ms t = 6 ms

Spindle Spray

t = 0 ms t = 4 ms t = 8 ms t = 12 ms

Oscillating Ramified Spray

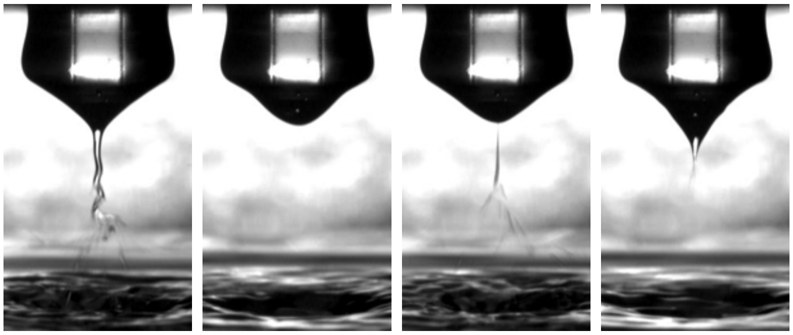

t = 0 ms t = 2 ms t = 6 ms t = 8 ms

Fig. 20 High speed images of EHDA unstable modes: part 3

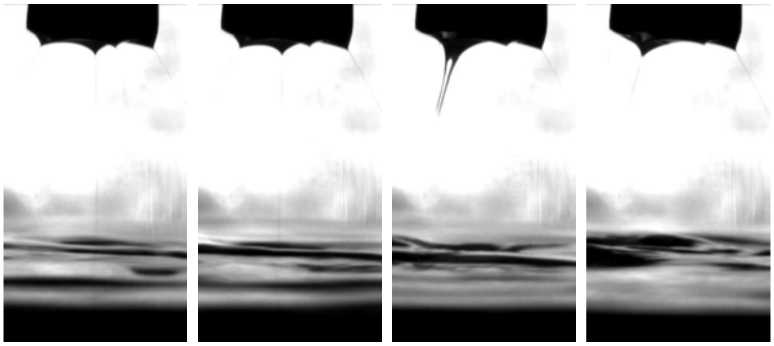
Oscillating Multi Cone Jet Spray

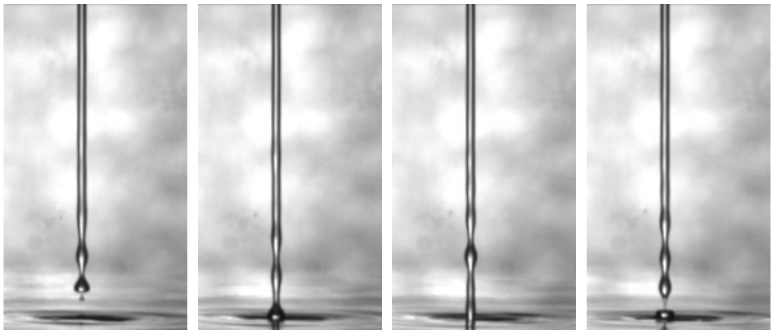
Oscillating Jet

Fig. 21 High speed images of EHDA unstable modes: part 4

3.2 EHDA Mode Analysis

3.2.1 EHDA modes affected by testing parameters

In Fig. 22, we illustrate five sets of static EHDA images. Those images are selected to show the effect of V, Q, H and d_i.

The first row of images is captured at H = 0.5 cm, which means the nozzle tip very close to the ground plane. We could observe the growing of Reversed Jet. The jet diameter of the reversed jet would become bigger as increasing the voltage, and the liquid column gains strong tolerance to resist external turbulence.

The second row of images is obtained at H =1 cm. An obvious transition of EHDA modes is observed, from bridge dripping, spindle spray, cone jet spray and multi cone jet spray. The location of the breaking spots or spray spots is found to move upwards as increasing the voltage.

The third row of images is gotten from the same testing condition, except for the flowrate. In that condition, we find a different mode transition from the previous condition. By increasing the voltage, the EHDA mode would start with bridge dripping, then switch to spindle spray, jet and ramified jet spray.

The testing condition in the fourth rows of images is same as the third one, except for the inner diameter. Since the liquid momentum force becomes much stronger with the help of small d_i, the liquid jet could not break into droplets until the applied voltage reaches 10 kV.

The last row of images is show the impingement mass at a situation with high flowrate and large height. We could find that the impingement format could be changed by applied voltage. Dripping, jet and spray impingement patterns could be generated in a same chamber without changing flowrate or nozzle.

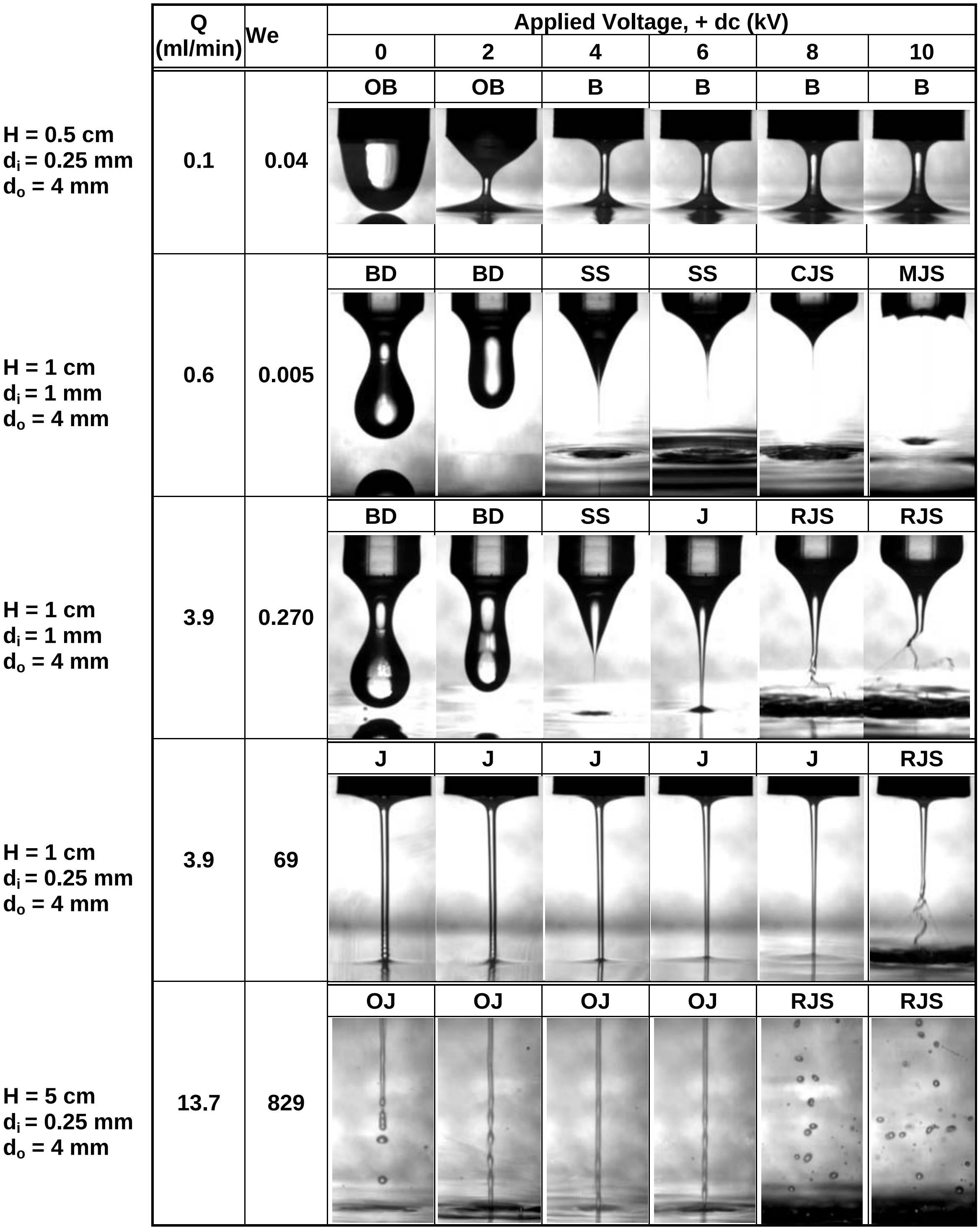

	Q (ml/min)	We	Applied Voltage, + dc (kV)					
			0	2	4	6	8	10
H = 0.5 cm d_i = 0.25 mm d_o = 4 mm	0.1	0.04	OB	OB	B	B	B	B
H = 1 cm d_i = 1 mm d_o = 4 mm	0.6	0.005	BD	BD	SS	SS	CJS	MJS
H = 1 cm d_i = 1 mm d_o = 4 mm	3.9	0.270	BD	BD	SS	J	RJS	RJS
H = 1 cm d_i = 0.25 mm d_o = 4 mm	3.9	69	J	J	J	J	J	RJS
H = 5 cm d_i = 0.25 mm d_o = 4 mm	13.7	829	OJ	OJ	OJ	OJ	RJS	RJS

Fig. 22 EHDA modes transition with effects of V, H, Q, d_i

3.2.2 Dimensional EHDA mode map

Over 1000 data have been corrected during the experiment of mode classification. It would be valuable to use those data to generate an EHDA mode map, like the two-phase map for the flow inside tubing. Relative past works have been reviewed.

EHDA Modes Map Part 1

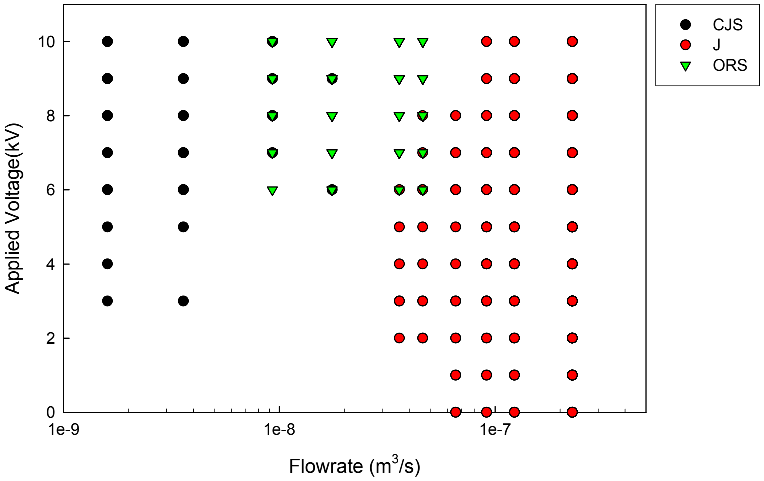

EHDA Modes Map Part 2

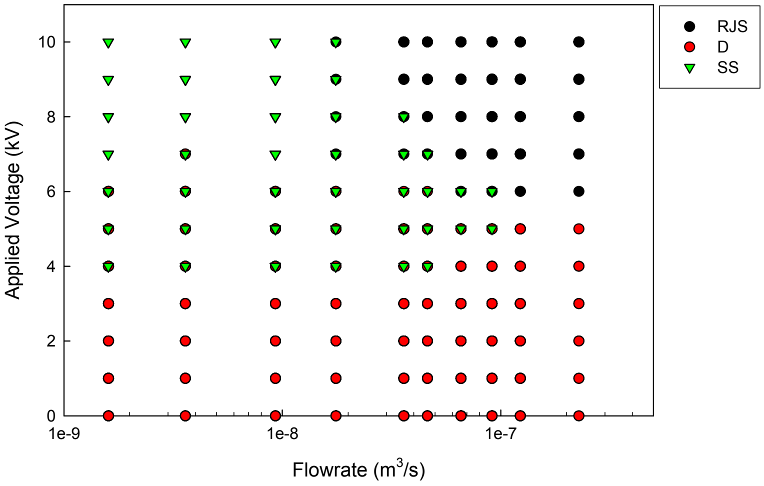

Fig. 23 Preliminary map for EHDA modes plotted as flowrate Vs. applied voltage

R. Ragucci et al had tried to investigate EHDA modes by changing flowrate and voltage [31]. A two dimensional diagram was provided for EHDA modes distribution. Despite that they had not provided mode definition or images in that paper, that method was perfect to illustrate the EHDA modes with 2 variables (Q, V). However, it is not valid for tests with multiple variables in current study. In Fig. 23, we use the same method as R. Ragucci's, selecting flowrate and applied voltage as two axes to display the distribution of EHDA modes. But it is obvious that just three of 11 EHDA modes could cover the whole figure. It is definitely not make sense by piling thousand data, based on testing parameters. We could image that the different type EHDA modes would overlay each other if total 11 modes was shown in the same figure.

When M.M. Hohman et al. studies the stabilities of EHD Jet [42, 43], they adopted a diagram to indicate the instability in terms of electrical field intensity and flowrate. They said they tried to comparing that diagram with the results of M. Cloupeau [44], but unfortunately they gave up because some of key parameters were missing. His work would be very critical if he could link his theoretical analysis with fundamental experimental observation.

M.M. Hohman's work reminds us that it needs to find the fundamental parameters in order to build the right EHDA mode map. The difficulties lie in three aspects in order to express the testing data in a nondimensional diagram.

1. EHDA is generated in the point-plane configuration. The E field is extremely nonlinear. Though we know local electric field intensity is one of the important parameter, it is difficult to predict it at breaking spot or other critical spots, where the local E field is couple with the surface charge of the free boundary flow.
2. The hydraulic effect could not be simply expressed by the flowrate. With the influence of electric field, the liquid meniscus, pending jet or even droplets would change dramatically.
3. The liquid sitting on the ground plane or nozzle tip would be influenced by the local electrical force. Those secondary charges would affect the flow pattern with assistance of surface tension. For example, the bridging mode and reverse jet mode are caused by the strong surface charges. Therefore we could find that it is necessary to examine the local electric field in several other critical spots, beside the flow breaking spot. Because it is important to determine the local electric field at the nozzle rim or the liquid film on the ground plane.

Considering our application requirement, three problems would be treated by using different strategies.

1. As to the first and second problems, we will solve them by adopting and modifying the developed analytical studies. There are plenty of theoretical studies on cone jet spray, and it is possible to expand those studies to fit in our testing conditions.

2. As to the third problem, we would avoid the problem by confine our study area in impingement region. In other words, some "slow" and "weak" modes would be eliminated from the scope of mode map, such as Bridging, Bridging Dripping Oscillating Bridging. Those modes are strongly affected by the stability theory under gravity and surface tension effect. In order to simplify the problem, it is better to take them out of the current study. Back to our research background, we definitely prefer strong momentum impingement pulse, instead of slow flow. So total modes at impingement region are 11 modes. Some of them are basic modes, CJS, J, RJS, MCJ, D, CJS+RJS. Others are transient modes between them, such as SS, DS, ORS, OJ, and OMS.

3.2.3 Preliminary nondimensional EHDA model

The fundamental forces during EHDA process are listed in following equation.

$$\begin{aligned}\text{EHDA}_{\text{mode}} &= f\left[f_{mom}, f_{sur}, f_{Cou}, f_{DEP}, f_{vis}, f_{gra} \right] \\ &= f\left[\frac{1}{2}\rho_l u^2, \frac{\sigma}{d}, \varepsilon_e E^2, -\frac{1}{2}E^2\nabla\varepsilon, \mu\frac{\Delta u}{\Delta\delta}, \rho_l g D \right]\end{aligned} \tag{3.1}$$

In the equation above, the Coulomb force and polarization force (DEP force) belong to the electrical force. Momentum force, surface tension and viscosity force are considered as hydraulic forces. Since the local electrical field and local charge density are coupled with flow boundary, it is difficult to directly calculate each force in such a wide testing range. Obviously, nondimensional force ratio might is a good choice to reveal the nature of various EHDA modes. Some nondimensional parameters are listed in the Table 11.

Table 11 Nondimensional parameters used in previous studies

Nondimensional Parameters	
Nondimensional flowrate[45]	$\eta = \left(\rho_l KQ / \sigma\varepsilon\varepsilon_0\right)^{1/2}$
Nondimensional length[45]	$r^* = \left(Q\varepsilon\varepsilon_0 / K\right)^{1/3}$
Nondimensional liquid properties[45]	$\Pi_\mu = (\sigma^2\rho_l t_e)^{1/3} / \mu$
Nondimensional current[45]	$\xi = I / \sigma(\varepsilon_0 / \rho_l)^{1/2}$
Nondimensional charge mobility [45]	$F_E = \frac{fk_i}{\varepsilon}\left(\frac{\rho}{\varepsilon_0}\right)^{1/2}$
Taylor number [46]	$\Gamma_0 = \frac{\varepsilon_0 A E_{n0}^2}{2\sigma}$
Nondimensional electric voltage[47]	$\Gamma_V = V\left(\frac{\varepsilon_0}{\sigma d_0}\right)^{1/2}$

J. Fenandez De La Mora and I.G. Loscertales [45, 48] introduced the first four nondimensional parameters that listed in the Table 11. By analyzing the flow and electric field near the Taylor cone, they found two relationships. One is about flowrate and current, which have following relationship:

$$I = f\left(\varepsilon\right)\left(\frac{\sigma Q K_e}{\varepsilon}\right)^{1/2} \tag{3.2}$$

Another relationship of the droplets diameter and flowrate are also found as following:

$$d_j = 0.4 \cdot r^* \tag{3.3}$$

Those two equations success in predicting the test for high conductive fluid ($K_e > 10^{-5}$ S/m). Other researchers verified and expanded their work in to a wide condition. A. M. Ganan-Calvo et al. [47], repeated the test similar with what J. Fenandez De La Mora did. His results confirmed what J. Fenandez De La Mora found for high conductive and viscosity fluids. And he claimed for low conductive and viscous fluids, the current in the Cone Jet Spray is proportional to $Q^{1/4}$, and droplet diameter is proportional to $Q^{1/2}$. L.T.

Cherney did a similar analysis and J. Fenandez De La Mora's correlation is validated by his deductions and tests.

Since the electric current has been successfully related to the nondimensional parameter η, the hydraulic effect might evolve with the nondimensional parameter η as well. So we choose η as the basic parameter to express the hydraulic effect during EHDA process.

$$\eta = \left(\rho_l KQ / \sigma\varepsilon\varepsilon_0\right)^{1/2} \tag{3.4}$$

Among the existing literature, there are two basic methods of represent electric field intensity. One is using electric current and liquid conductivity[45, 49]. The other is using electric potential and testing configuration[50-53]. We choose the second method in order to incorporate the effect of test setup. At a distance from the nozzle tip, the local electrical field was given as following[50]:

$$E\left(r,z\right) = \frac{V}{Log\left(8H / D_O\right)} Log\left\{ \frac{\left[r^2 + \left(1-z\right)^2\right]^{1/2} + \left(1-z\right)}{\left[r^2 + \left(1+z\right)^2\right]^{1/2} - \left(1-z\right)} \right\} \tag{3.5}$$

Neglecting the effect of radius distance, the simplify form could be expressed as following[51]:

$$E_0 = \frac{4V}{D_O \cdot Log\left(8H / D_O\right)} \tag{3.6}$$

By using the similar method as A.M. Gana-Calvo[47], following nondimensional electric field intensity could be yielded:

$$\Gamma = \frac{4V}{D_O \ln(8H / D_O)} \left(\frac{\varepsilon_0 D_0}{\gamma} \right)^{1/2} \tag{3.7}$$

where: the term of $\left(\frac{\varepsilon_0 D_0}{\gamma} \right)^{1/2}$ represent the basic electric field intensity, which has a same force level of surface tension at the nozzle tip.

This nondimensional number Γ is combined with η to build the secondary mode map (See Fig. 24).

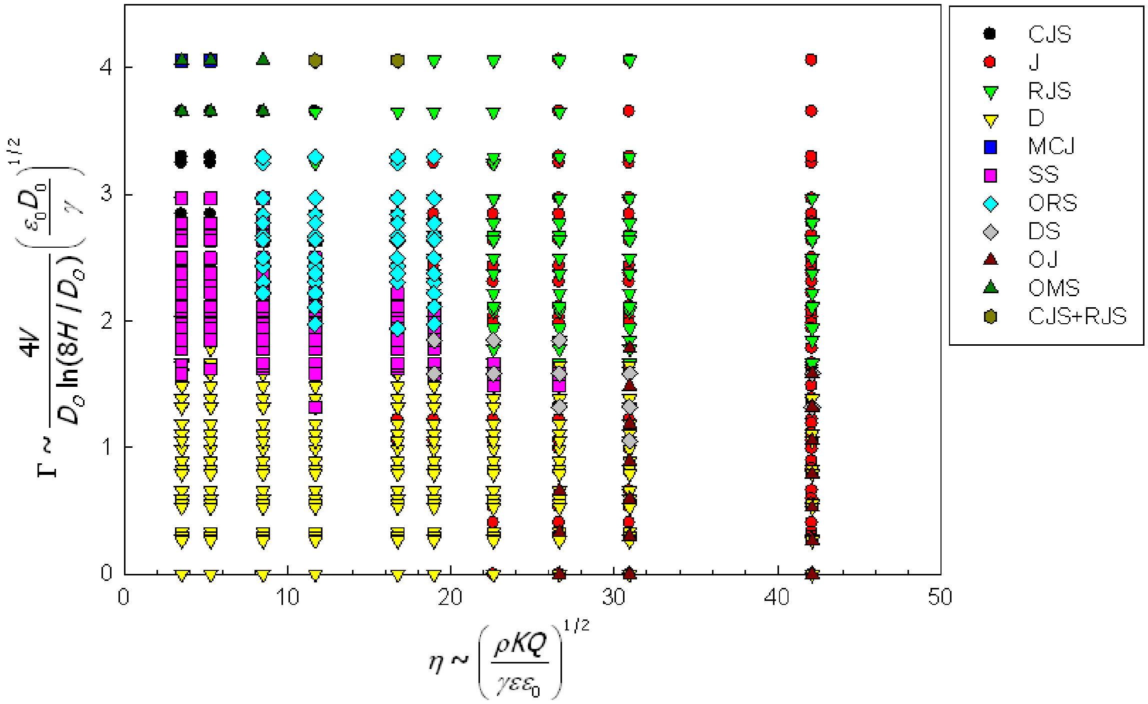

Fig. 24 Preliminary map of EHDA modes plotted by η and Γ

Compare with the previous mode map by using voltage and flowrate, the new mode map is much better. Some of the modes could appear clearly in the new mode map. However, there is no clear boundary between those modes. For example, the J and RJS are overlapped at right up corner in the figure. That indicates that the parameters, η and Γ, are not effective to disclose the fundamental mechanism qualitatively, since η and Γ are normally used in the studies, which are different from our study. The main difference of those studies with current work lies in two aspects.

1. In previous work, their testing condition is relative low, so that the hydrodynamic effect is not strong or sometime could be neglected. In our test, we would reach much high flowrate due to our application. And most of the reported researches are related to a specific mode, cone jet spray. Therefore many assumption made in previous studies might not fit in the current study.
2. During the tests, they tested quite a few of fluids, whose properties are various. In other words, researchers used fluid properties as variables to study the fundamental force balance and developed the correlations. In this study, we only change the operation parameters, in stead of the properties.

3.2.4 Final nondimensional EHDA mode map

The first question is how to modify the nondimensional electric field intensity, Γ. In the form of Γ, there is no factor from the flowrate. However, it is observed, when the flowrate is high, the breakpoint would move from meniscus to the end of pending jet, until the jet mode occurs. The length of the pending jet without electrical field should be considered. In case of EHDA process, several characteristic dimensions might be evolved into the final form of nondimensional electric field intensity:

$$D_{Bo} = \sqrt{\frac{\gamma}{\rho g}} \tag{3.8}$$

$$D_e = \sqrt[3]{Q t_e} \tag{3.9}$$

Where: $t_e = \dfrac{K}{\varepsilon \varepsilon_0}$

By numerous tests, we selected the following nondimensional parameters:

$$Y \sim \Gamma \cdot \left(\frac{D_0^2 D_{Bo}^2}{H D_e^3} \right)^{1/8} \tag{3.10}$$

$$X \sim \eta \cdot \left(\frac{D_0 D_{Bo}^2}{D_i H^2} \right)^{1/4} \tag{3.11}$$

By using those two nondimensional parameters, 11 modes are sitting in the diagram with a clearly boundary (See Fig. 25). A sketch of mode relationship could be extracted from the EHDA map. (See Fig. 26) Dripping, jet, multi cone jet spray modes are at the border of the map. Cone jet spray mode is located in the mid of multi cone jet spray and dripping. Ramified jet spray is between jet and multi cone jet spray. Oscillating modes fill the gap between those modes.

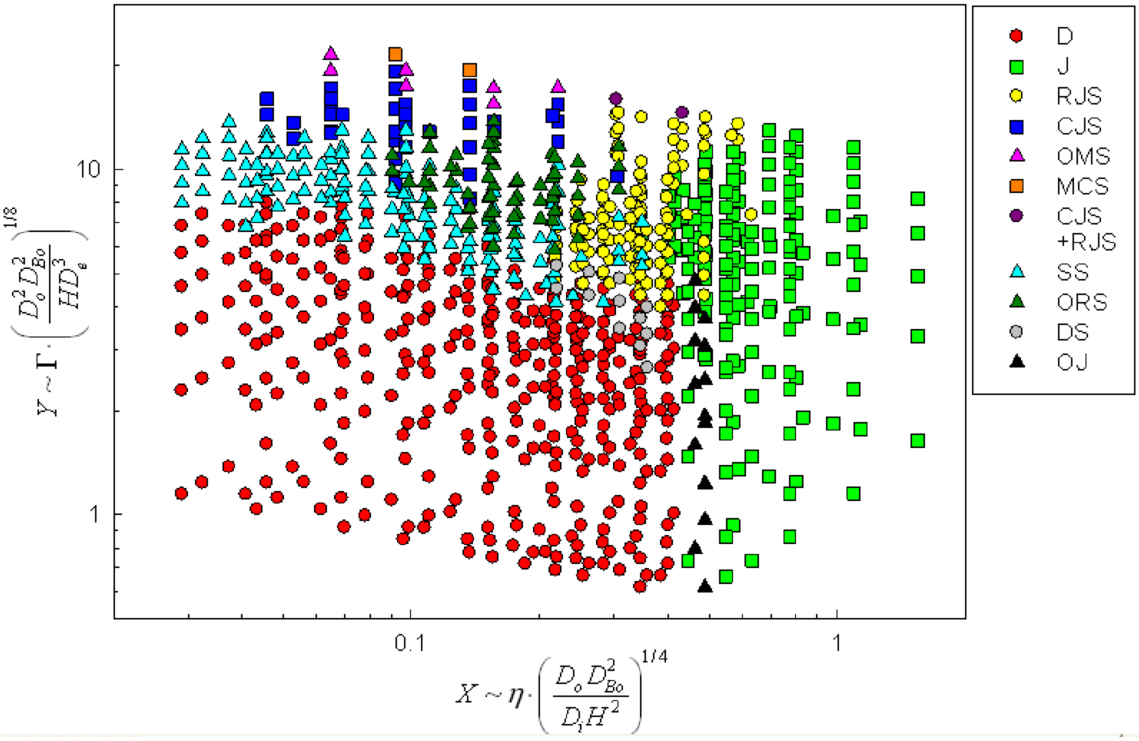

Fig. 25 EHDA Mode Map of Ethanol

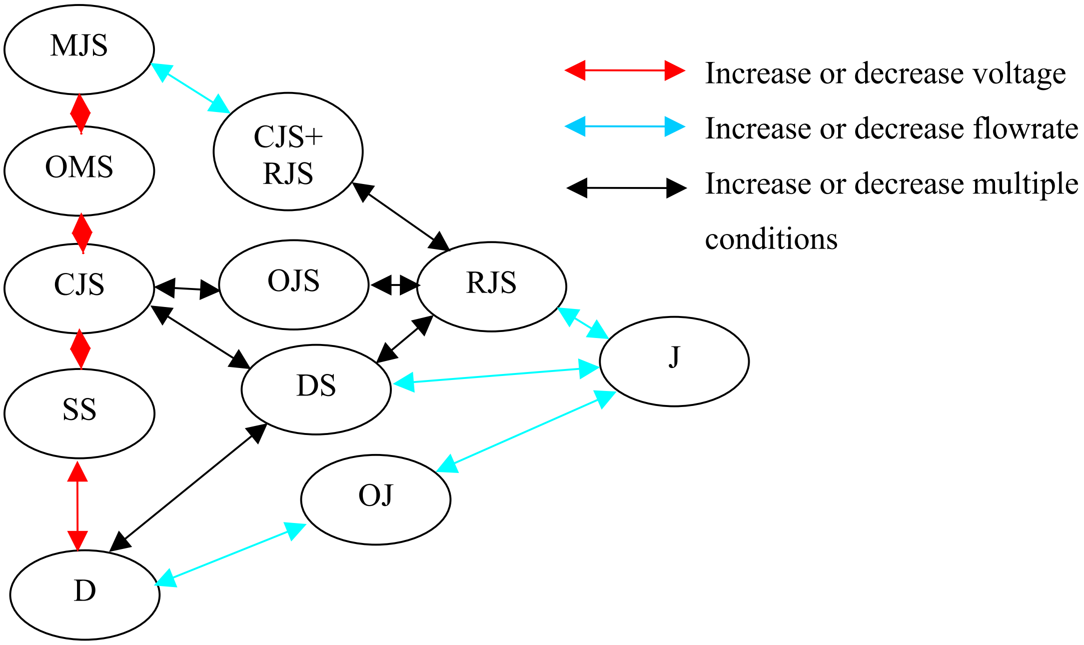

Fig. 26 Sketch of EHDA modes transition

From literature reviews, we could arrange some reported EHDA modes into our diagram. (see Fig. 27) Though those works dealt with different fluids in different testing configuration, their modes sit at the suitable place in the diagram.

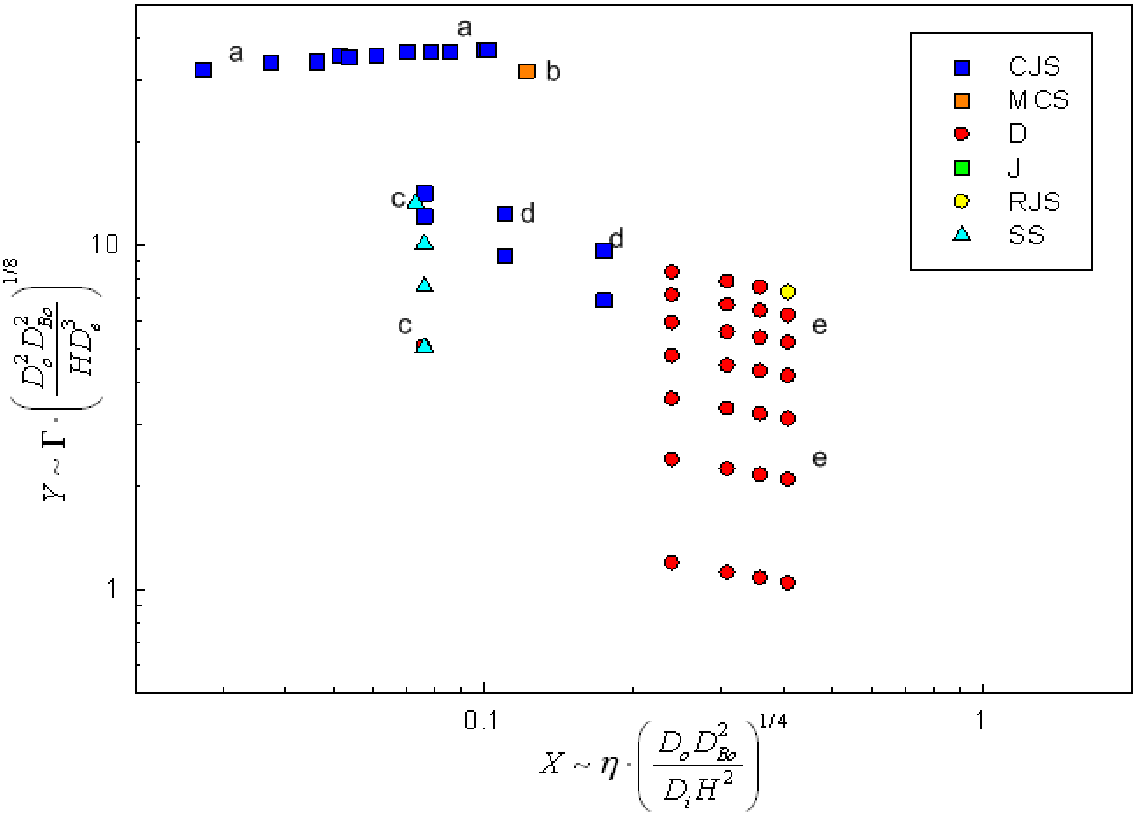

Fig. 27 Some reported EHDA mode results plotted in our EHDA Mode Map

Note: a: J. Rosell 1994 [48], b: A. Jaworek 1999[36], c: A. Jaworek 1999 [54], d: H. Park 2004 [34], e: K. Sung 2004 [55]

3.3 EHDA Mode Study Summary

Dynamic and static images were captured in various EHDA conditions. There are total 3 categories and 14 modes that had been classified clearly. By using nondimensional analysis, we developed an EHDA mode diagram which could separate each mode in our testing condition. That mode map could match with other reported EHDA modes with different fluids, nozzle dimension and operation parameters.

CHAPTER 4. TWO-PHASE EHDA IMPINGEMENT COOLING

With previous part of study on EHDA modes, we are able to explore the process of two-phase change under EHD effect. The goal is to better understand:

1). How EHDA will affect two-phase impingement heat transfer?

2) Could EHDA be used as a tool to study the effect of impinging mass form (drops, jets, or sprays) on heat transfer?

4.1 Effect of Flow Rate

Using the acrylic capillary, the impingement heat transfer was studied as a function of volumetric flow rate and applied voltage. For a given capillary dimension, the magnitude of the flow rate will establish the hydrodynamic nature of the flow exiting the capillary. The flow, whether it is surface tension or momentum dominated, can be characterized with the Weber number, defined here as

$$We_{d_i,d_o} = \frac{4\rho_l d_o Q^2}{\pi d_i \sigma} \tag{13.1}$$

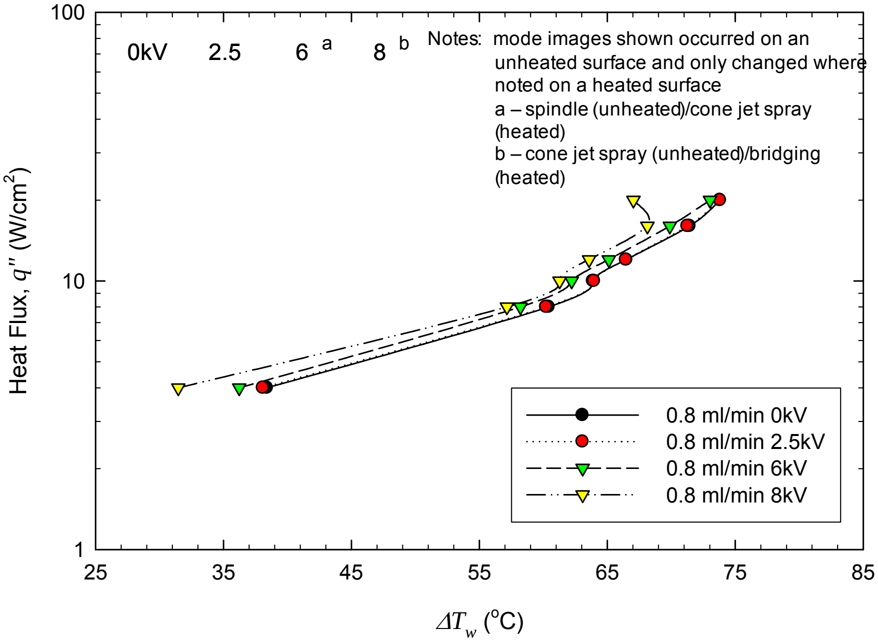

Fig. 28 EHDA effect on two-phase impingement heat transfer at $A_s = 0.5$ cm^2 and H = 1 cm on flat mounting surface

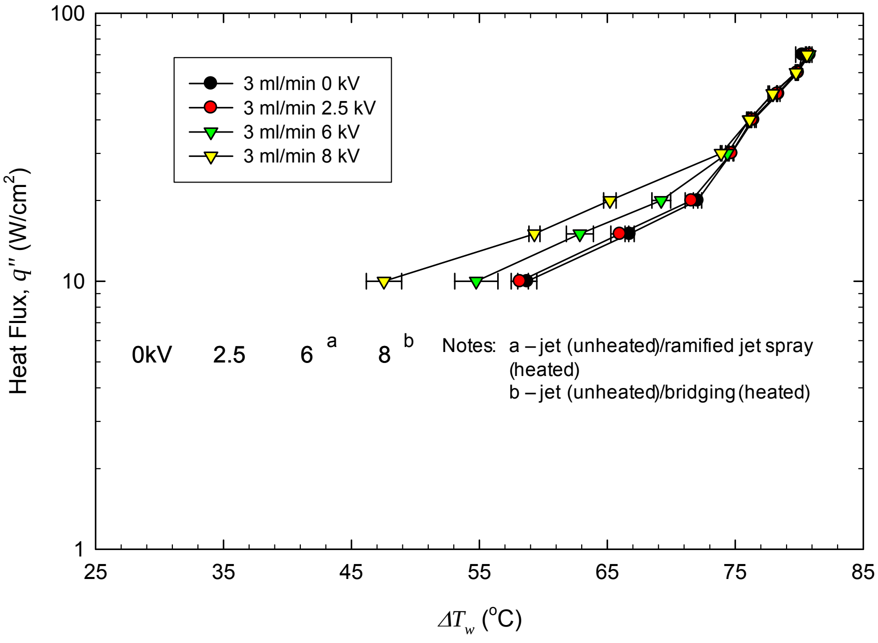

Fig. 29 EHDA effect on two-phase impingement heat transfer at $A_s = 0.5$ cm^2 and H = 1 cm on flat mounting surface

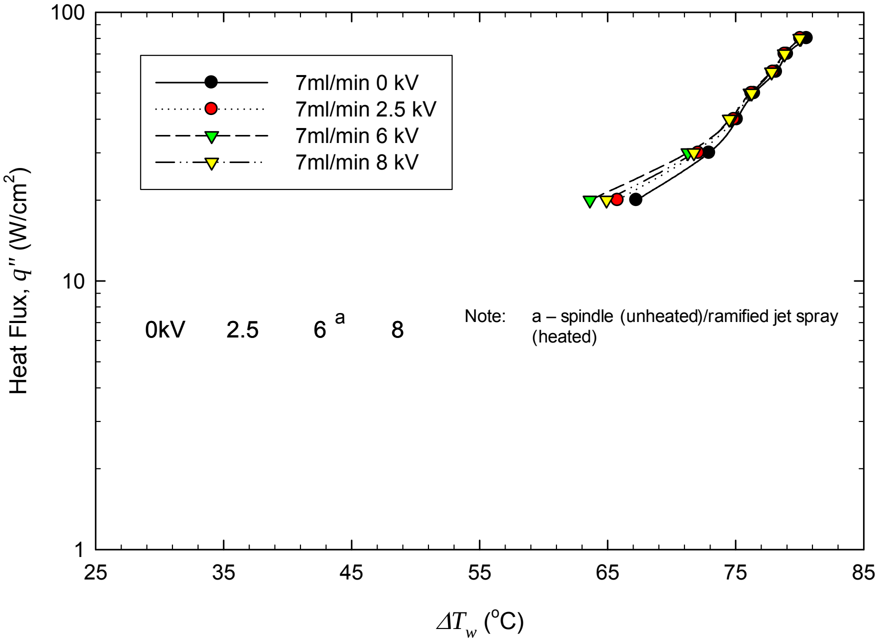

Fig. 30 EHDA effect on two-phase impingement heat transfer at $A_s = 0.5$ cm^2 and H = 1 cm on flat mounting surface

Results for three different flow rates are shown in Fig. 28 - Fig. 30. The change in the heat transfer is measurable as applied voltage and volumetric flow rate are varied as shown in the heat flux versus wall superheat results. The electrostatic and liquid momentum forces relative to surface tension force increase with increasing voltage and flow rate. In general, the increase in electrostatic force results in a lower wall superheat while the increase in momentum results in a higher achievable critical heat flux (CHF) to a point. However, the effect of the electrostatic force changes as the flow rate increases due to the change in the EHDA mode (free boundary flow shape). How the EHDA mode changes is shown in the images within each graph. It is important to note that at voltages of 6 and 8 kV the modes can change once the impinging surface is heated due to vapor interaction with the impinging flow. For the low flow rate condition, the electrostatic force only has to overcome surface tension (We = 0.011) resulting in a slight decrease in the wall superheat throughout the heat flux range once a spray is created ($V \geq 6$kV). The spray mode is different at this flow as the droplets produced are more monodisperse. As the flow rate is increased the spray produced becomes more polydispersed because the jet breakup starts from kink-type instability, breaking the jet into a range of droplet sizes. Both sprays produce enhancement. As the heat flux and flow rate increase, the effect of EHDA on the two-phase heat transfer process decreases. Beyond q" = 30 W/cm^2, the vigorous surface boiling and increased vapor flow prevent any further enhancement with EHDA. However, once a spray is produced ($V > 6$kV), the surface mass flux decreases because the impact diameter of the spray is larger than the heated surface. This will be discussed further in the next section.

The variation in the EHDA effect was the greatest at Q = 3 ml/min, so it was decided that the effect of other parameters presented would be studied at this flow rate. The repeatability of the results at Q = 3 ml/min, shown as error bars in the graph, were verified by repeating the experiments over 3 different days.

4.2 Effect of Applied Voltage, Capillary Type, and Height

The greatest variation in heat transfer with EHDA was measured at Q = 3 ml/min and q" = 10 W/cm$_2$. This condition was used to better understand the effect of the applied voltage, the type of capillary, and the capillary to heated surface spacing. Results for the stainless steel capillary and acrylic capillary as a function of applied voltage, V, and capillary to heated surface spacing, H, are shown in Fig. 31 and Fig. 32, respectively. The results are presented as the ratio of the average enhanced heat transfer coefficient, h_E, to the average heat transfer coefficient, h_0, obtained at 0 kV with the acrylic capillary. Using the stainless steel and acrylic capillaries allow for comparison of the effect of momentum and electric field changes at the same flow rate and applied voltage, respectively. Hydrodynamically, the momentum will increase by 16 times as the capillary diameter, d_i, decreases from 1 mm (acrylic capillary) to 0.25 mm (stainless steel capillary). This effect can be seen in the h_E/h_o data and the images shown in Fig. 31 at 0 kV. However, surface tension limits the increase in heat transfer to less than 10% by maintaining a liquid film on the heater surface. The flat mounting plate maintains a liquid film, ~2 mm thick, over the entire surface.

Electrostatically, the intensity of the electric field increases significantly with the use of the stainless steel capillary. In the acrylic capillary, the point of application of the high voltage is 10.6 mm from the tip of the capillary, but for the stainless steel capillary the high voltage is applied directly to the capillary. Thus, the spacing between the high voltage source and the grounded heater surface is less for the stainless steel capillary. The combination of the smaller spacing and smaller capillary diameter results in a much more intense electric field in the region around the capillary tip for the stainless steel capillary, creating a larger Coulomb force.

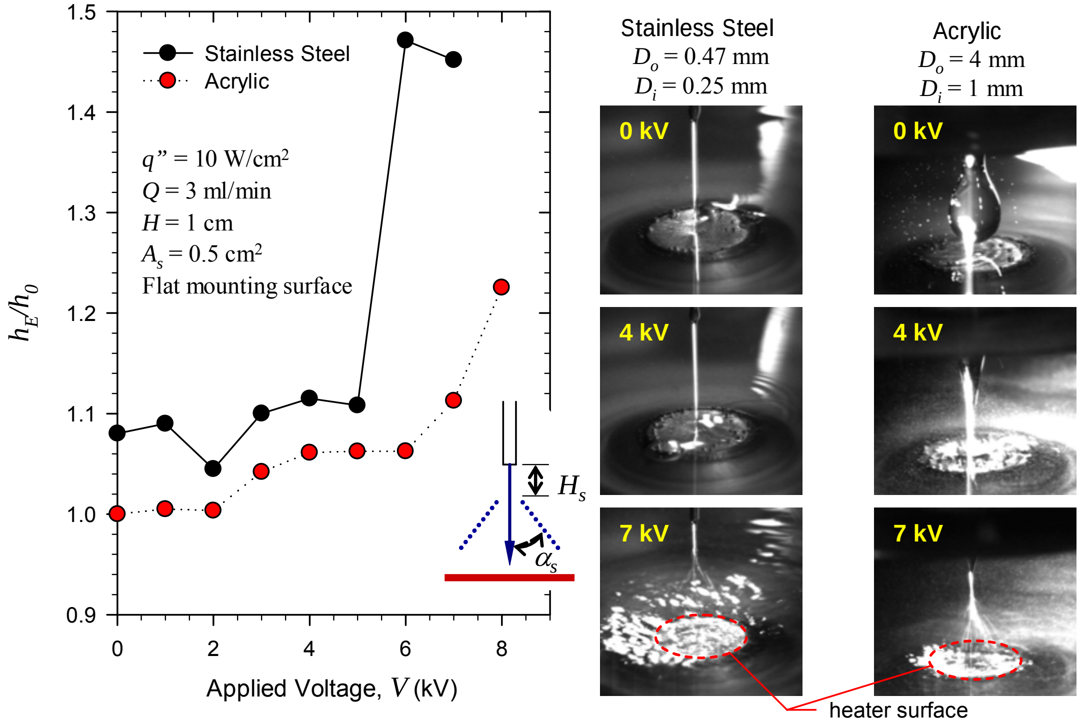

Fig. 31 Effect of applied voltage and capillary geometry on impingement heat transfer

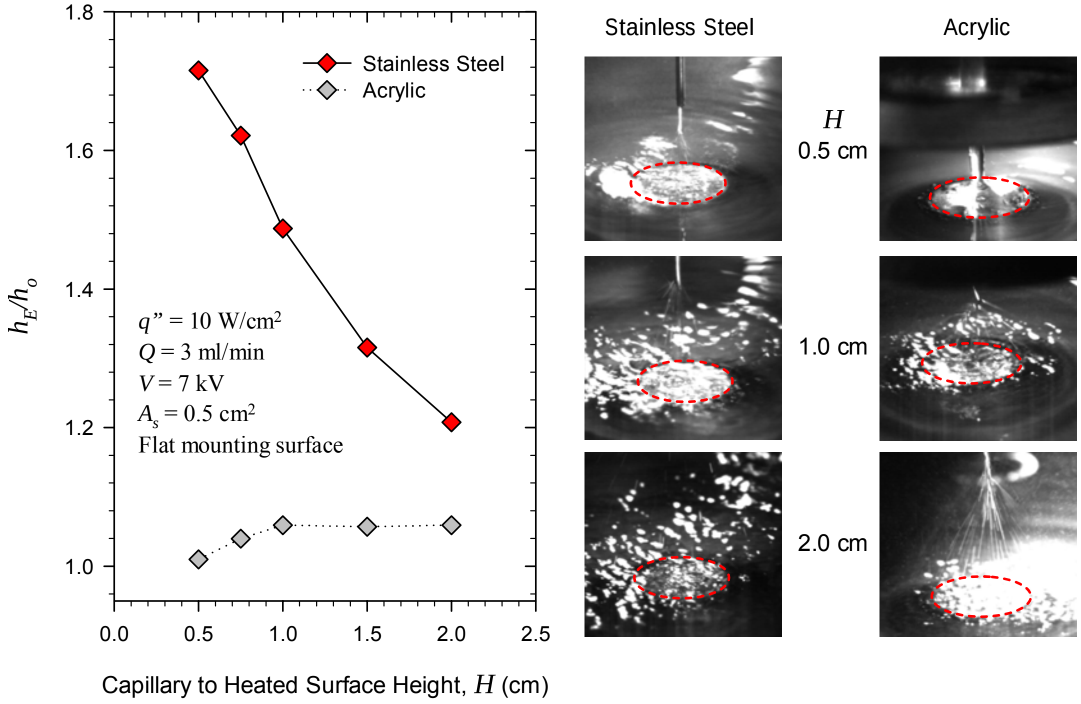

Fig. 32 Effect of height and capillary geometry on impingement heat transfer

As voltage is increased from 0 kV, the heat transfer enhancements for both capillaries increase differently. Due to the 16x increase in momentum from the stainless steel capillary, the electrostatic forces have only a slight effect for applied voltages less than 5 kV. This can be seen visually in the image at 4 kV in Fig. 31 where there is no noticeable change in the jet compared to 0 kV. However, the transition from dripping to a jet occurs between 2 and 6 kV for the acrylic capillary, see image at 4 kV, and this results in an increase in heat transfer. The transition to a spray for both capillaries is obvious but different. For the stainless steel capillary, the increase in heat transfer is significant from 5 to 6 kV but drops slightly from 6 to 7 kV. For the acrylic capillary the transition from jet to spray occurs from 6 to 7 kV with a continued increase in heat transfer with further increase in applied voltage. The reason for the increased heat transfer and differences between the two capillaries is due to the momentum and spreading of the spray. The increase in the momentum of the flow is noticeable when the mode transitions to a spray resulting in a thinning of the liquid film over the heated surface and mounting plate, which can be seen to some degree in the images at 7 kV in Fig. 32 The intensity of the electric field will affect the spray creation. Once a spray is created, further increase in applied voltage (increase in field intensity) will increase the spray angle, αs, due to increased droplet charge and repulsive force. Additionally, once a spray is produced, further increase in field intensity will shorten the point of jet breakup, smaller Hs, increasing the height above the heated surface where the spray in created. Both of these effects, greater α_s and smaller H_s, will result in less mass flux to the heated surface as field intensity increases. Inspection of the images at 7 kV in Fig. 31 shows this effect. For the stainless steel capillary the spray impinging diameter is much greater than the heated surface diameter, where the spray and surface diameters are similar for the acrylic capillary.

Knowing that the electric field intensity will have a significant effect on the spray angle and in turn the heat transfer, the effect of capillary to surface height was studied for both capillary configurations; the results are shown in Fig. 32. Again, the results for the two capillaries are different. As the capillary to heater surface spacing, H, is increased the heat transfer enhancement decreases significantly for the stainless steel needle. From inspection of the images it is evident that the mass flux and momentum to the heater surface are highest at H = 0.5 cm and decrease with increasing H. The behavior for the acrylic nozzle is different with the heat transfer increasing with increasing H, but only slightly. The electric field intensity for the acrylic nozzle is less than the stainless steel capillary, so the spray, if produced will have less momentum. Since the momentum is less, the liquid film on the heater surface caused by the flat mounting plate remains over the heater surface, which can be seen to some extent in the images in Fig. 32. At H = 0.5 cm, the liquid film on the heater surface is drawn up to the capillary due to the polarization force (dielectrophoretic force or DEP force), which will draw the liquid of higher permittivity toward the region of highest electric field intensity. This can be seen in the image in Fig. 32. This bridging effect prevents a spray from being produced resulting in no increase in heat transfer. As H is increased a spray is produced, but with less momentum resulting in a slight heat transfer enhancement.

The results presented in Fig. 31 and Fig. 32 were obtained at a heat flux of only 10 W/cm^2. The effect of heat flux for the two capillaries is shown in Fig. 32. Above 30 W/cm^2 there is no measurable increase in the heat transfer compared to the 0 kV case, which represents ho. From the images it is evident that the mass flux to the surface is lower than that at 0 kV. It is interesting that the heat transfer is not negatively affected until 70 W/cm^2, just before critical heat flux is reached now that less than 3 ml/min is impacting the surface.

4.3 Effect of Mounting and Heater Surfaces

Both the mounting surface and size of the heater surface affect the heat transfer from the surface as shown in Fig. 33. The mounting surface effects liquid drainage from the heated surface. With a flat mounting surface (see Fig. 14) liquid is retained on the surface around the heater due to surface tension. This has two effects:

1. A liquid film is retained over the heated surface increasing the thermal resistance;
2. Additional liquid is supplied to heater surface as impinging mass is evaporated.

These two effects result in a higher wall superheat and higher CHF, respectively, compared to the sloped mounting surface. The effect of the liquid film resistance with the flat mounting surface is evident in Fig. 33 where the wall superheat is greater at all heat fluxes compared to the sloped surface. The sloped surface prevents liquid retention, so the only liquid held around the heater surface is due to its surface tension only. As the heat flux is increased for a given mass flow rate to the surface, dryout will begin to occur at the periphery of the heated surface. With the flat mounting surface liquid is available from the mounting surface to the heater periphery helping to delay the onset of dryout leading to a higher CHF.

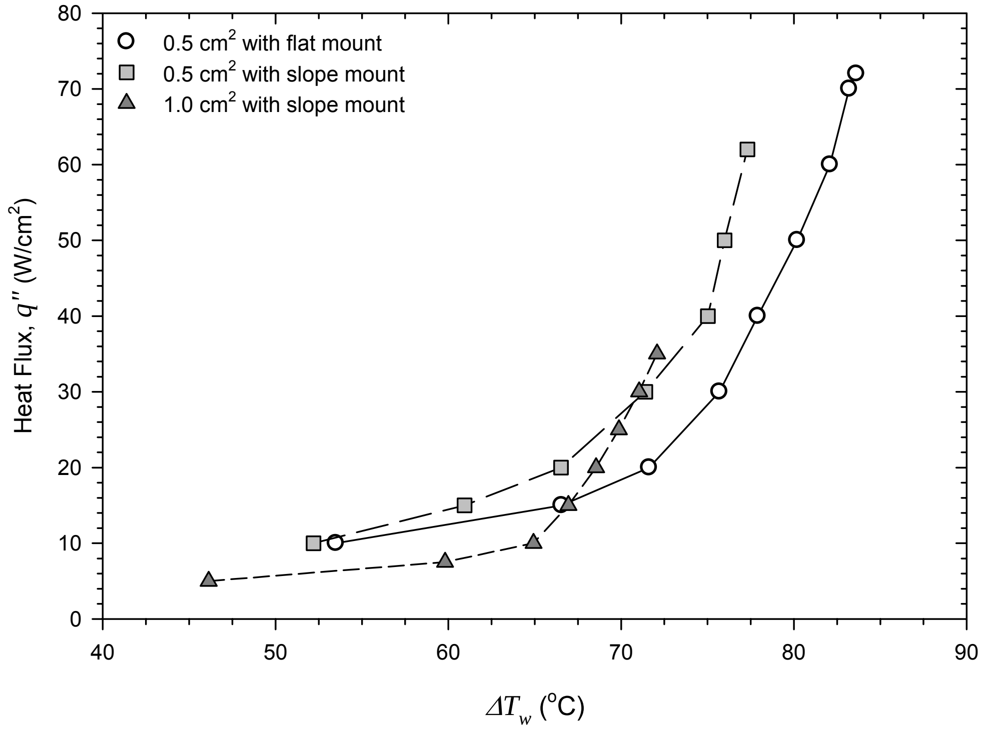

Fig. 33 Effect of surface support structure and surface area on impingement evaporation with no applied electric field through stainless capillary

An increase in the heater surface area with sloped mounting surface further changes the heat transfer characteristics for a given impinging mass flow rate condition. At low heat fluxes, < 30 W/cm^2, the larger surface area allows for greater liquid retention thus greater thermal resistance resulting in a higher wall superheat. Above 30 W/cm^2 the interaction of the surface nucleation process and the convection via jet impingement result in a slightly lower thermal resistance for the larger 1 cm^2 surface compared to the 0.5 cm^2 surface. However, the larger surface area leads to local dryout occurring at the periphery at lower heat fluxes.

The application of an electrical field further changes the heat transfer for the different surface conditions. These results presented as h_E/h_o versus heat flux are shown in Fig. 34. The mounting surface and surface size influenced the liquid distribution on the heater surface where the electrical field influences the mass distribution coming to the surface. At an applied voltage of 7kV, the mass impacting the surface is in the form of a ramified spray (polydisperse droplet distribution) compared to a jet at 0 kV. At 7 kV the volumetric flow rate at 3 ml/min is distributed over a larger area than 1cm^2. With the polydisperse spray the overall momentum of the mass impacting the surface is greater and the amount of mass is less resulting in a thinner liquid film and a pronounced increase in heat transfer as shown in Fig. 34. The heat transfer enhancement decreases rapidly as the heat flux increases due to the increase in surface nucleation, increase in vapor momentum escaping from the surface, and less than 3 ml/min impacting the heater surface.

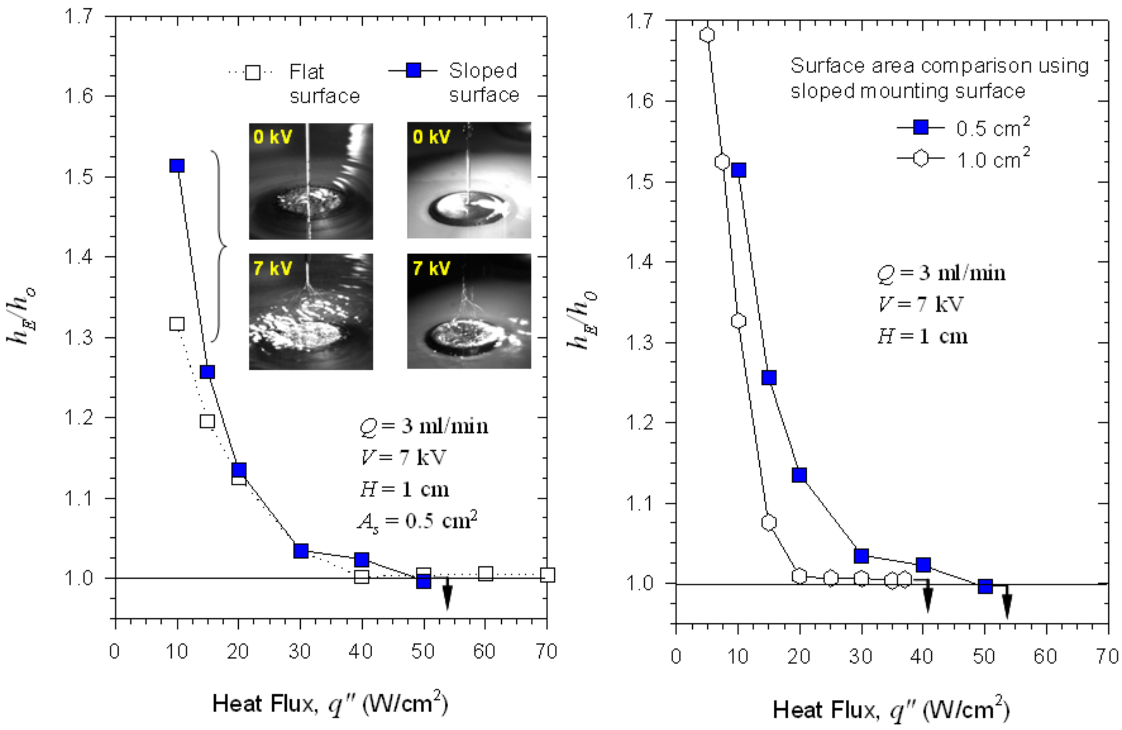

Fig. 34 Effect of EHDA, surface support structure, and surface area on impingement heat transfer with the S.S. capillary

4.4 Effect of Heater Surface Geometry

Recognizing the influence and interaction between the impinging mass and the surface conditions, the effect on EHDA on a geometrically enhanced heater surface was explored. The enhanced surface structure shown in Fig. 35 was vacuum brazed to the heater surface. This surface is being investigated for microchannel evaporation and is only tested here to obtain a preliminary understanding of the effect of enhanced surfaces on impingement heat transfer. Results are shown in Fig. 35 where the effect of the enhanced surface and EHDA are compared to the same size smooth surface. At 0 kV, the enhanced surface results in a lower thermal resistance compared to the smooth surface up to 30 W/cm^2. It is important to note that the heat transfer coefficient, determined from equation (11.2), was based on the same thermocouple location for both the smooth and enhanced surface. That is the temperature measurement was not normalized to the surface, indicating the 0.8 mm high finned surface reduced the overall liquid film resistance. Higher thermal resistance resulted at heat fluxes greater than 30 W/cm^2 because the channels blocked liquid supply from evenly distributing over the 1cm^2 surface. Application of 6 kV further decreased the thermal resistance at heat fluxes below 25 W/cm^2 with better liquid distribution. Above 25 W/cm^2, no measurable enhancement occurred due in part to some of the mass not impacting the heated surface.

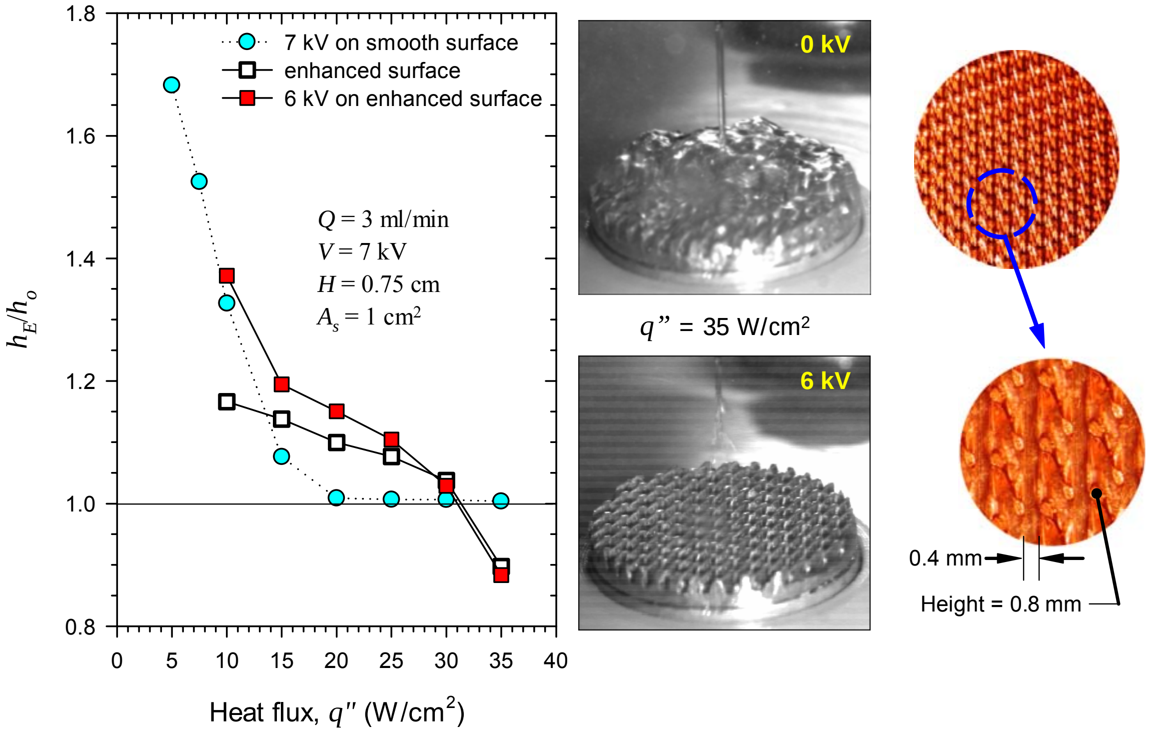

Fig. 35 Effect of surface structure and EHDA on impingement heat transfer

4.5 Single Capillary versus a Capillary Array

The interaction between the impinging mass and the heated surface directly affects the nature of the two-phase heat transfer. The results presented thus far have been for free boundary flow from a single capillary impinging on a heated surface. To achieve higher heat fluxes and transport will require higher impinging mass rates optimized with surface characteristics. An array of capillaries creates the ability to redistribute and/or increase the mass rate to the heated surface. Preliminary array experiments were performed to understand how the electric fields would affect the impinging mass characteristics.

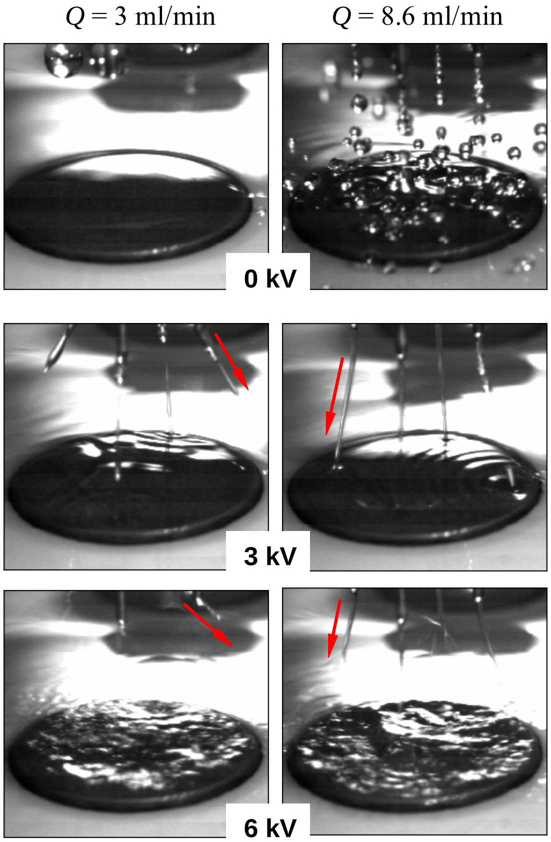

Fig. 36 Sequence of images showing effect of electric field on capillary array

The application of an electric field to an array of capillaries compared to a single capillary is different. A sequence of images are presented in Fig. 36 showing that as the applied voltage is increased, surface charge distorts the jets produced. The transition from dripping to jets and then ramified spray is similar for the single capillary and array of capillaries. However, the increase in surface charging and electric field causes the jets and droplets to divert away from neighboring capillaries, due to like charge repulsion. As seen in the images, the electrostatic repulsive force competes with the flow momentum.

As expected, the application of an electric field to an array will change the impinging heat transfer characteristics compared to a single capillary under the same total mass flow rate. Results highlighting the difference in heat transfer enhancement between a single capillary and array for two different flow rates are shown in Fig. 37. At a flow rate of 3 ml/min and 6kV applied voltage the divergence in the spray created is significant resulting in much lower mass impinging on the heated surface to the point that the heat transfer is suppressed and CHF is reached just above 20 W/cm2. At higher flow rates the spray divergence results in enhancement at lower heat fluxes transitioning to suppression at higher fluxes due to less mass impacting the heated surface. It is important to note that at 0 kV the array of 4 capillaries results in a lower heat transfer coefficient compared to a single capillary because the flow from a single capillary is a jet while the flow from the array is discreet drops.

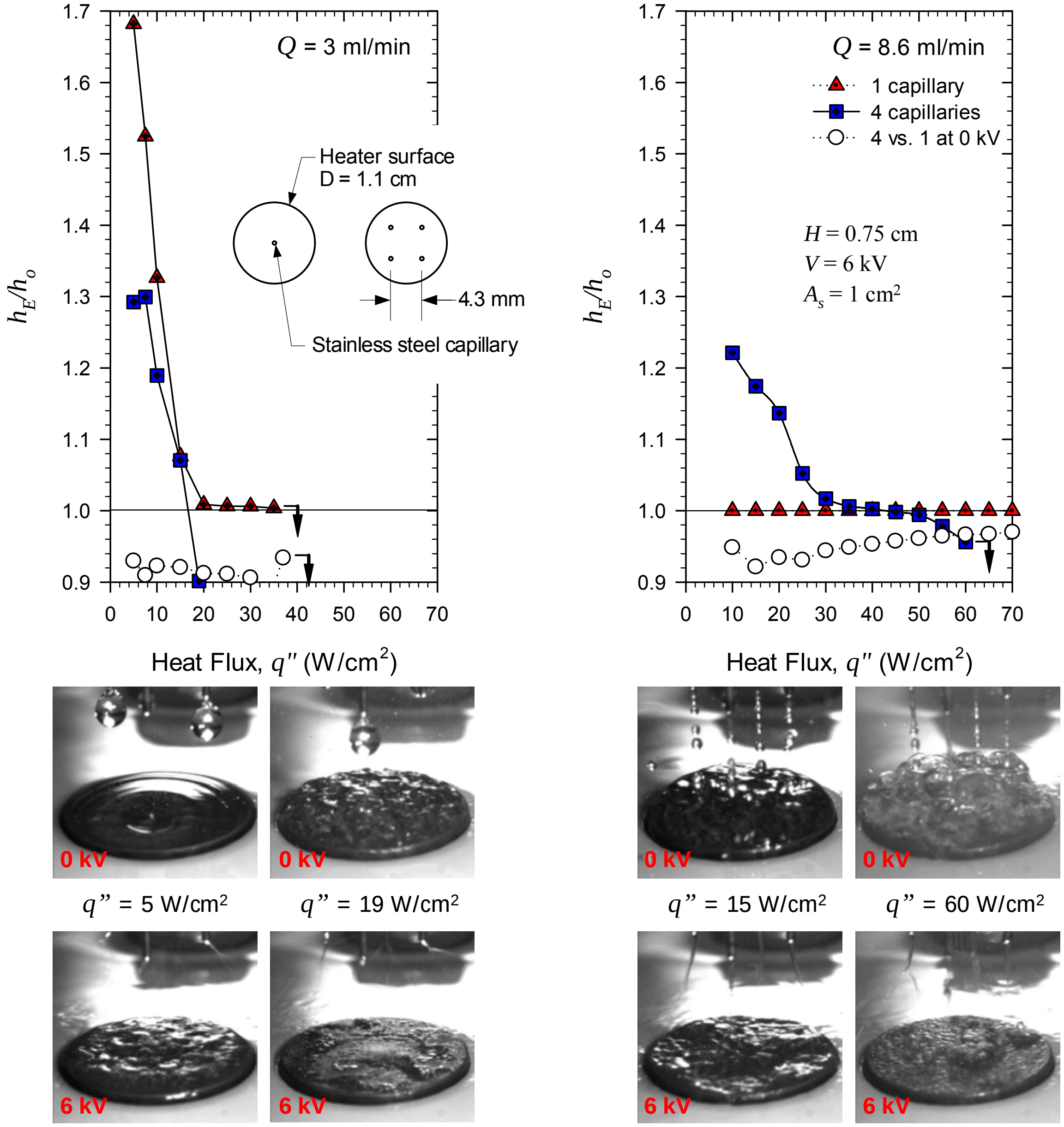

Fig. 37 Effect of capillary array on impingement heat transfer

4.6 EHDA Cooling Summary

The ability to change the mode of impinging mass from discreet drops to a jet and then a spray did change the surface heat transfer. The characteristics of the impinging mass on heat transfer was dependent on capillary flow rate, applied voltage, capillary to heated surface spacing, capillary geometry, heat flux, heater surface geometry, and capillary array configuration.

The enhancement occurred primarily at low heat fluxes (below 30 W/cm^2) under ramified spray conditions where the droplet momentum promoted thin films on the heated surface. Higher heat fluxes resulted in greater vapor momentum from the surface minimizing the effect of different modes. However, under ramified spray conditions less mass was impacting the heated surface showing that heat transfer rates at higher heat fluxes were achievable with less mass, resulting in greater evaporation efficiency.

PART 2. MICRO JET IMPINGEMENT COOLING

In this part, the micro jet impingement cooling (MJIC) would be investigated. The micro jet in this study has a constant diameter of 250 μm and experiments in saturated environment. In Chapter 5, literature reviews would be first presented on previous works on CHF correlation and recently study on micro jet. The experimental setup of MJIC would be shown in Chapter 6. Experimental results of CHF in single MJIC would be compared with existing CHF correlations in Chapter 7. In Chapter 8, a semi-theoretical CHF model would be developed on the assumption of two different two-phase heat transfer regimes during single MJIC. Finally, the CHF and heat transfer coefficient during multi MJIC would be studied in Chapter 9.

CHAPTER 5. LITERATURE REVIEW OF MICRO JET IMPINGEMENT COOLING

Since the traditional jet cooling have been widely used in steel industries and nuclear engineering, most experimental works were conducted in atmosphere pressure and jet diameter in those reviews are larger than 1 mm. Four important reviews have to be mentioned here. Webb and Ma had reviewed single phase jets cooling in 1995 [3], and Wolf et al. reviewed two-phase jet cooling in 1993 [4]. Both of two reviews are focused on the experimental studies on jet impinging cooling. The latest reviews on numerical simulation of jet impingement is done by N. Zuckerman and N. Lior [5]. Beside those three reviews, J.H. Lienhard V published a review on jet impingement cooling in 1995 [6]. His review was focused on analytical studies of wall jet and heat transfer at different regions when the jet impinging on the heating surface.

After the jet impinging on a smooth surface, the liquid would move outward in form of wall jet. In Lienhard's review [8], he listed 7 regions for the single-phase wall jet created by asymmetric jet. (See Table 12) The suggested Nu numbers in each region are presented in the table 5 of his review. As to the study of two-phase jet impingent cooling, theoretical works on the wall jet are very limited due to the complexity of boiling process. In this study, part of the analytical solutions would be used to develop the CHF correlation in MJIC. Detail works would be shown in Chapter 8.

Table 12 Transition of wall jet during impingement process [8]

Wall jet region	Range
Stagnation zone (S)	$0 \le \frac{r}{d} \le 0.787$
Transition S to BL	$0.787 \le \frac{r}{d} \le 2.23$
Boundary layer region (BL)	$2.23 \le \frac{r}{d} \le 0.1773 \cdot \mathrm{Re}_d^{1/3}$
Similarity region (SL)	$0.1773 \cdot \mathrm{Re}_d^{1/3} \le \frac{r}{d} \le 1200 \cdot \mathrm{Re}_d^{-0.422}$
Transition SL to TB	$1200 \cdot \mathrm{Re}_d^{-0.422} \le \frac{r}{d} \le 28600 \cdot \mathrm{Re}_d^{-0.68}$
Turbulent region (TB)	$\frac{r}{d} \ge 28600 \cdot \mathrm{Re}_d^{-0.68}$
Hydraulic Jump region (HJ)	$\frac{r_{hj}}{d} = f\left(\mathrm{Re}_d, Fr_d, We, \frac{Js}{d}, \frac{r_{Js}}{d}\right)$

5.1 Existing CHF Correlations for Two-phase Jet Impingement Cooling

Back to 1980's and 1990's, several CHF correlations have been developed mainly based experiments and analytical modes. Monde, Katto and Lienhard did plenty of tests with

Freon and water, and finally developed several CHF correlations. [56-58] (See Table 13) Those CHF correlations were based on both theoretical models and experimental results.

Table 13 Recommended CHF correlations of a free surface, saturated jet

M. Monde [56]	V correlation $\Phi = 0.221\gamma^{0.645} We_{D-d}^{-0.343}\left(\frac{d}{D+d}\right)^{0.364}$ L correlation $\Phi = k\gamma\left(\frac{d}{D}\right)^{2}$ where: $\frac{1}{k} = 0.0389\gamma^{0.674}\left(\frac{d}{\sqrt{\frac{\sigma}{g(\rho_l - \rho_v)}}}\right)^{1/3}$ I correlation $\Phi = 0.691\gamma^{0.466} We_{D-d}^{-0.421}\left(\frac{d}{D+d}\right)^{0.303}$ HP correlation $\Phi = 0.172\gamma^{1.27} We_{D-d}^{-0.28}\left(\frac{d}{D+d}\right)^{1.01}$
Y. Katto and S. Yokoya [57]	$\Phi = \gamma\left(0.0166 + 7.00\gamma^{-1.12}\right) We_{l-d}^{-\xi}\left(1 + \frac{D}{d}\right)^{-\xi}$ $\xi = 0.374\gamma^{-0.0155}(for: \gamma \geq 248)$ $\xi = 0.532\gamma^{-0.0794}(for: \gamma \leq 248)$
A. Sharan and J. H Liehnard V [58]	$\Phi = \left(0.00171\gamma + 0.21\right)\left(\frac{We}{1000}\right)^{-A(r)}\left(\frac{D}{d}\right)^{-1/3}$ $A(\gamma) = 0.486 + 0.06052Ln(\gamma) - 0.0378(Ln(\gamma))^2 + 0.00362(Ln(\gamma))^3$

From the table above we could easily find that CHF are composed by following factors.

Nondimensional CHF: $$\Phi_{CHF} = \frac{q''_{CHF}}{\rho_v H_{fg} u_l}$$

Density ratio: $$\gamma = \frac{\rho_l}{\rho_v}$$

Geometry ratio: d / D

We Number: $$We_l = \frac{\rho_l {u_l}^2 l}{2\sigma},$$

Subcooling factor: $$\frac{C_p \cdot (T_{sat} - T_l)}{H_{fg}}$$

Those five factors are the result of complex forces balance between vapor momentum force, liquid momentum force and surface tension, plus the subcooling effect, and latent heat factor. The general form of CHF correlation for jet impingement cooling would be like following:

$$\Phi_{CHF} = f\left(\gamma, We, \frac{D}{d}, \frac{C_p \cdot (T_{sat} - T_l)}{H_{fg}}\right) \tag{14.1}$$

In this study, we mainly study the CHF with very small subcooling effect. Therefore, the CHF correlation could be expressed as following formula:

$$\Phi = f\left(\gamma, We, \frac{D}{d}\right) \tag{14.2}$$

5.2 Studies on CHF Model Development for Jet Cooling

J.H. Lienhard V and R. Eichorn developed a model for CHF by the jet impingement cooling [59]. They considered that the vapor kinetic energy would balance the surface energy in formation of droplets. The energy balance is expressed as the equation(14.3):

$$\frac{1}{2}\left(\rho_v u_v \frac{\pi}{4} D^2\right) u_v^2 \sim \left(\frac{\alpha \rho_v u_E \frac{\pi}{4} d^2}{\rho_l \frac{\pi}{6} d_{drop}^3}\right) \pi d_{drop}^2 \sigma \tag{14.3}$$

Where: α is the fraction of liquid converted into droplets.

d_{drop} is the droplet Sauter diameter

By substitute the vapor velocity equation $u_v = \frac{q''_{CHF}}{\rho_v h_{fg}}$ into the equation(14.3), the following equation could be obtained:

$$\frac{q''_{CHF}}{\rho_v h_{fg} u_e} = \alpha^{1/3} \cdot \left(\frac{\rho_l}{\rho_v}\right)^{1/3} \left(\frac{\sigma}{\rho_l u_e^2 D}\right)^{1/3} \left(\frac{d}{d_{drop}}\right)^{1/3} \left(\frac{d}{D}\right)^{1/3} \tag{14.4}$$

They consider that α and d/d_{drop} were governed by the density ratio γ, which could be estimated by the experimental data. Thus they get the form of CHF correlation.

Y. Haramura and Y. Katto provided a model that assumes vapor penetrates a liquid sublayer (δ_c) on the heating surface as discrete columns, shown in Fig. 38 [60]. Monde proposed a successful CHF correlation based on that model [61]. They considered at the point of burnout, the CHF of Jet Impingement would equal to latent heat of the liquid pass through the cylinder passage.

$$\pi \cdot d \cdot \delta_c \cdot \rho_v \cdot u_e \cdot h_{fg} = q''_{CHF} \cdot \left[\frac{\pi}{4}\left(D^2 - d^2\right)\right] \tag{14.5}$$

Where: δ_c is depend on the Helmholtz critical wavelength (λ_H), which is could be express as equation (14.6) after simplification.

$$\delta_c = 0.0053 \cdot \sigma \cdot \rho_v \cdot \left(1 + \frac{\rho_v}{\rho_l}\right)\left(\frac{\rho_v}{\rho_l}\right)^{0.4} \left(\frac{h_{fg}}{q''_{CHF}}\right)^2 \tag{14.6}$$

Combining the equation (14.5) and (14.6), the following equation is obtained:

$$\frac{q''_{CHF}}{\rho_v h_{fg} u_e} = 0.278 \cdot \left(\frac{\rho_l}{\rho_v}\right)^{0.533} \left(1+\frac{\rho_l}{\rho_v}\right)^{1/3} \left(\frac{\sigma}{\rho_l u_e^2 \left(D-d\right)}\right)^{1/3} \left(1+\frac{D}{d}\right)^{1/3} \tag{14.7}$$

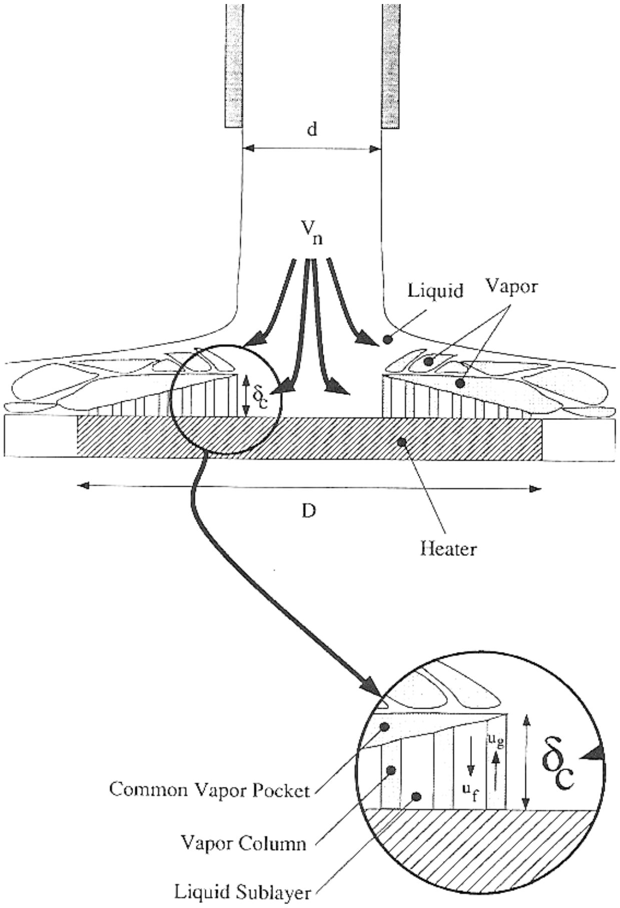

Fig. 38 Sketch of jet impinging model developed by Monde and Katto [60, 61].

Y. Haramura and Y. Katto's model not only be used in jet impingement cooling, but also applied to two-phase spray cooling [60]. For example, M.S Sehmbey et al. developed a macrolayer dry-out model of CHF correlation for spray cooling [18]. They considered that the CHF occurs when a thin macrolayer dries out before the vapor bubble escaping.

5.3 Reviews on Micro Jet and Jet Array Impingement cooling

Multi jet impingement cooling is believed one way to enhance the two-phase impingement cooling. B.W. Webb and C.F. Ma had summarized the some researches on jet array in the single-phase jet impingement cooling[3]. Most of researches were focus on developing and verifying the Nu correlation for multi jet cooling. As to two-phase jet array impingement cooling, a few works have been carried out in order to explore the heat transfer limitation. For example, M. Monde had tested two-phase impingement cooling with jet array[62]. Based on the results from two kinds of fluids and 21 kinds of jet patterns, he concluded that the CHF of multi jet impingement cooling could be predicted by his modified V-correlation. This kind of approach is not only adopted by Monde. M.T. Meyer had studied the two-phase cooling by a single confined slot jet and slot jet array[63]. Their final CHF correlation for jet array impingement was also based on the CHF correlation for single slot jet cooling. The CHF correlations in two cases have very high accuracy. Monde's CHF correlation for multi jet impingement cooling has an error less than 20% with respect to his testing results.

The recent progresses on two-phase jet impingement cooling have two major trends. One is to study the jet array in boiling regime with purpose of get high heat transfer capability. J.H. Lienhard V[64] built a very powerful confined jet array, and obtained a extremely high heat transfer record, which exceeded 17 kW via a 10 cm^2surface. The other aspect of jet array research is to explore the multi MJIC. For example, E.N. Wang tested confined micro jets[65], and M. Fabbri tested free micro jets [66, 67] with purpose for thermal management. In their studies, the diameter of the micro jet was from 50 μm to 250 μm.

And their results showed many advantages, such as high boiling efficiency. In Table 14, we listed some representative works on jet array.

Table 14 Recent studies on multi jet impingement cooling

Topic	**Group**	**Fluid**	**Array Parameters (mm)**	**Notes**
Free Boundary Micro Jet Array	M. Fabbri V. K. Dhir [66]	Water FC40	d: 0.069-0.25 N:37-271 W_J: 1,2,3	Optimization design: $W_J = 25.8 \cdot d$ Highest CHF 310W/cm^2 occur at U_e = 12.5 m/s, nozzle type: W_J = 3 mm, d = 0.174 mm
	M. Fabbri [67]	Water	d:0.0693-0.25 N: 37-397 W_J: 1,2,3	Best nozzle type: 1) s = 1 cm^2, d =0.118 mm, Q=1700mL/min, CHF 840W/cm^2 2) s = 1 cm^2, d = 0.069 mm, Q=920mL/min, CHF 680 W/ cm^2
Free Boundary Jet Array	M. Monde [62]	Water R113	d:2 N:2-4 W_J: 9.1-24.6	CHF correlation developed from the V-correlation of single jet impingement $\Phi_{CHF} = 0.221\gamma^{0.645} \cdot We_{2L-d_n}^{-0.343} \cdot \left(1-\frac{2L}{d_n}\right)^{-0.364}$
	Y. Pan and B.W. Webb [68]	Water	d:1, 2, 3 N:9, 7 W_J/d:1-8	Combined single-phase and two-phase cooling at Re_d: 5000-20000 $\overline{Nu} = 0.225\,\mathrm{Re}_{dn}^{2/3}\,\mathrm{Pr}^{1/3}\,Exp\left[-0.095\frac{s}{d_n}\right]$
Confined Micro Jet Array	E.N. Wang K.E. Goodson et. al. [65]	Water	d: 0.05,0.1, 0.15 W_J/d: 6.7-60	Max CHF = 90 W/ cm^2 with 4 x 76 µm at Q = 8 mL/min
Confined Jet Array	M.T. Meyer I. Mudawar et. al. [63]	FC-72 Ethanol	d: 0.127, 0.254, 0.508 N = 3	CHF Correlation developed from single confined slot jet $\Phi_{CHF} = 0.0919\gamma^{\frac{2}{3}} \cdot We_{L-d_n}^{-0.157} \cdot \left(\frac{d_n}{L-d_n}\right)^{0.331} \cdot \left(1+\frac{CpT_{sub}}{h_{fg}}\right)^{\frac{1}{3}} \cdot \left(1+0.034\gamma\frac{CpT_{sub}}{h_{fg}}\right)^{\frac{2}{3}}$
	C.H. Oh J.H. Lienhard V et. al. [64]	Water	d: 2.78 N:14 W_J: 10	CHF reaching 17 MW/m^2 with 500°C superheat and Re_d = 130000

CHAPTER 6. EXPERIMENTAL SETUP OF MICRO JET IMPINGEMENT COOLING

6.1 Micro Jet Impingement Cooling Test Setup

The experiment setup is based on the test bench of EHDA impingement cooling system. Since those two systems need similar functional modules, they are designed to share most components, such as testing chamber, testing surface, heat exchanger, et al. There are several differences between two systems.

1. The EHDA cooling system is equipped with a high voltage power supply, which is able to provide up to 15 kV functional high voltages.
2. The EHDA cooling system works in the atmosphere pressure, while the MJIC system works in both saturated and subcooled condition.
3. The MJIC system runs at a higher flowrate, and removes more heat and therefore is equipped with a large condenser, compared with the EHDA system.

The schematic drawing of the micro jet cooling system is shown in Fig. 39. Inside the loop, the liquid is driven by a periodic pump. Since the flowrate in MJIC experiments normally is higher than that in EHDA impingement cooling, a bypass loop is added right after the filter. Part of liquid would pass the float flowmeter and finally exit out of the nozzle. As the liquid vaporized on the testing surface, its vapor would condense on the coil located at the upper part of the testing chamber. The condensing coil is made of quarter inch copper tubing. During MJIC experiments, the total length of the coil is over

11 meters, which is about one order magnitude longer than that in EHDA impingement cooling. The testing chamber serves as a reservoir for both liquid and gas. It provides a space for non-condensable gas so that it would not accumulate inside tubing. The condensing liquid and bypass flow would converge at the bottom of the chamber. The liquid level would automatically adjust to reach a thermal balance. The liquid inside the chamber would be sucked into a flat plat heat exchange under the test chamber and return to the pump.

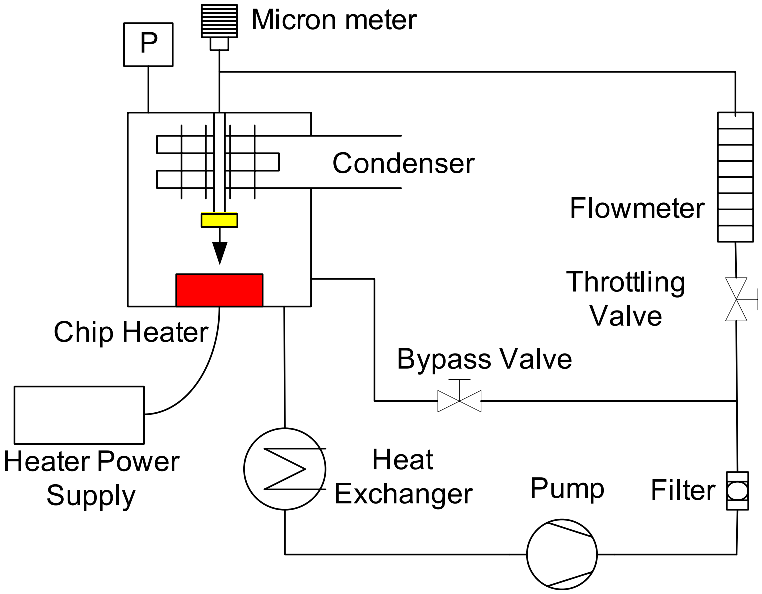

Fig. 39 Sketch of micro jet impingement cooling system

Jet impingement cooling experiments usually are carried out in two kinds of common environment. One is at 1 ATM environment. Most of reported experimental researches belong to this type. For example, most of Monde's CHF correlation evolved with test data at 1 ATM or at even higher pressure[56, 61, 62]. The other is in low pressure saturated environment. For example, the saturated environment for water is with $P_{sat} \approx 3000$ Pa. This kind of environment is much difficult to create because the vacuum sealing around the high heat flux element usually would fail after intensively heating.

One of the advantages of this kind of environment is the testing surface could reach a lower surface temperature, instead of 100°C in 1 ATM for water. So far few works on the micro MJIC is tested in saturated condition, but we conduct most of experiments in this environment. The outgasing rate has been reduced to 0.25 Pa/min. The closing loop still could seal very well in case of heat flux up to 250 W/cm^2. In Fig. 40, the test chamber is shown, including the test chamber, condenser, heater etc. Most of them had been used in the EHDA impingement cooling.

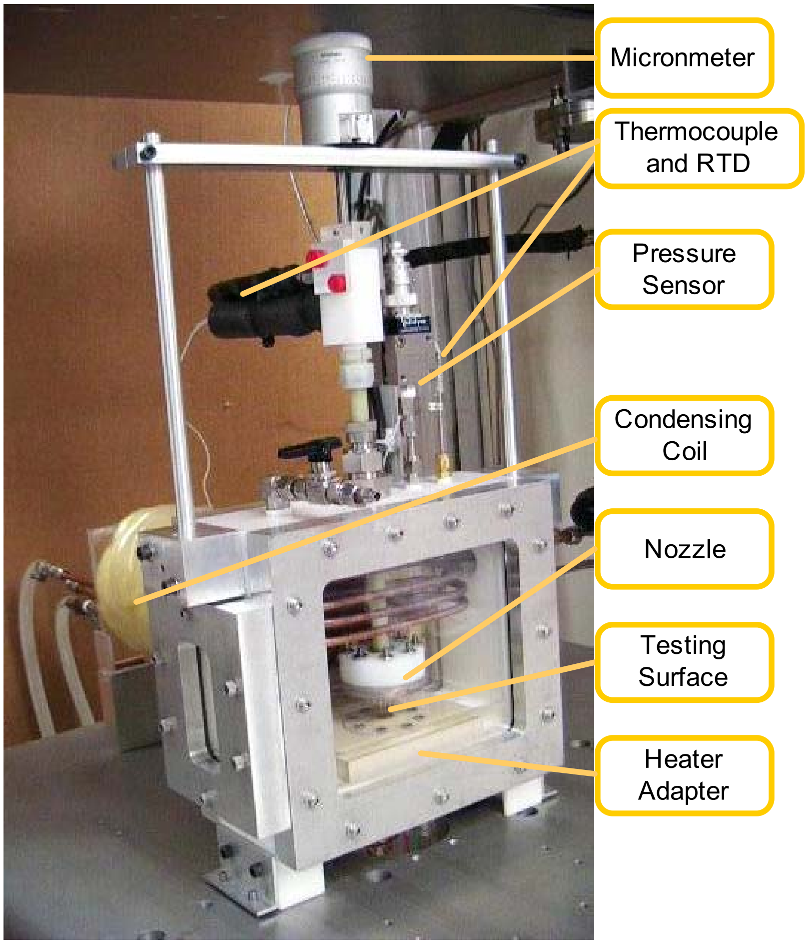

Fig. 40 Photo showing test setup of micro jet impingement cooling system

In the current study on MJIC, small liquid jet is generated by capillary tubing, instead of a tiny hole. Using micron meter, the capillary tip is adjusted to 1 mm above the testing surface, with the purpose of reducing vapor disturbance. Three types of micro jet nozzles are shown in Fig. 41. The 1 jet and 4 jet nozzles had been used in EHDA impingement cooling.

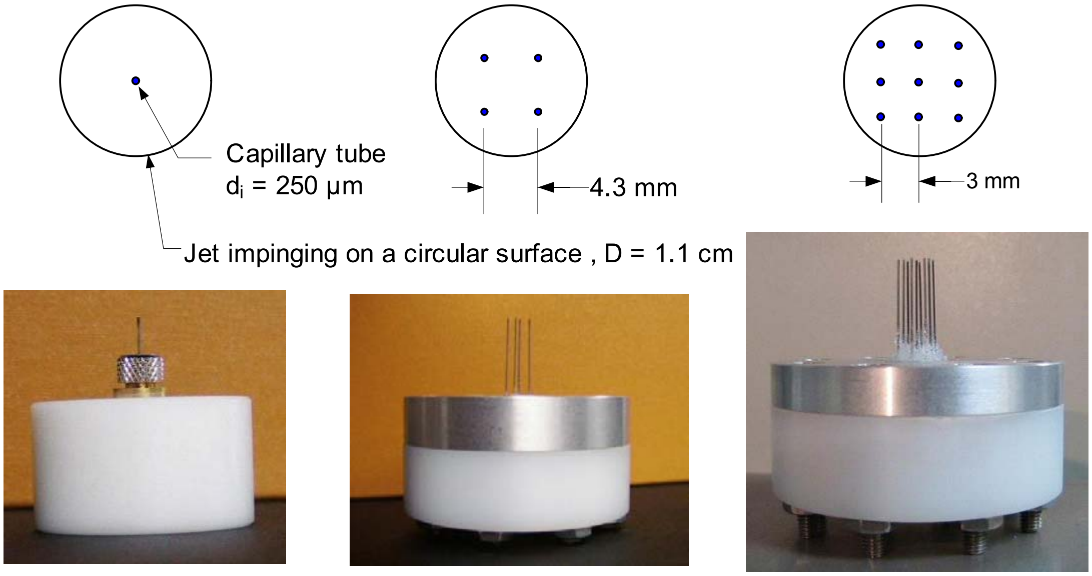

Single jet nozzle

Four micro jet nozzle

Nine micro jet nozzle

Fig. 41 Micro jet nozzles and their configuration

6.2 Uncertainty Analysis

During the MJIC tests, we want to determine two parameters, CHF and heat transfer coefficient. Those are same as during the EHDA impingement cooling tests. The measurement method and Data reduction could be refer to Chapter 2. We calculated the uncertainty for the tests with each fluid. The uncertainty analysis results are shown in Table 15-Table 17.

Table 15 Measurement uncertainty in single and multi MJIC with water

Water	T_{WB}	T_W	$T_{Cond\ 1}$	T_v	T_{le}	$T_{Cond\ 2}$	P_{sat}	T_{sat}
Average	1.17%	1.15%	0.56%	0.45%	0.34%	0.07%	0.31%	0.14%
Max	3.45%	3.42%	0.94%	0.86%	0.57%	0.33%	0.58%	0.27%
Min	0.10%	0.03%	0.00%	0.06%	0.02%	0.00%	0.07%	0.04%

Table 16 Measurement uncertainty in single and multi MJIC with ethanol

Ethanol	T_{WB}	T_{W}	$T_{Cond\ 1}$	T_{v}	T_{le}	$T_{Cond\ 2}$	P_{sat}	T_{sat}
Average	0.17%	0.17%	0.28%	0.34%	0.15%	0.18%	0.37%	0.10%
Max	0.59%	0.59%	0.39%	0.57%	0.29%	0.33%	0.84%	0.23%
Min	0.00%	0.00%	0.00%	0.01%	0.00%	0.00%	0.05%	0.01%

Table 17 Measurement uncertainty in single and multi MJIC with HFE7000

HFE7000	T_{WB}	T_{W}	$T_{Cond\ 1}$	T_{v}	T_{le}	$T_{Cond\ 2}$	P_{sat}	T_{sat}
Average	0.22%	0.19%	0.01%	0.15%	0.10%	0.05%	0.10%	0.01%
Max	2.04%	1.68%	0.04%	0.22%	0.20%	0.11%	0.38%	0.05%
Min	0.04%	0.04%	0.00%	0.05%	0.04%	0.00%	0.03%	0.00%

Compare with the uncertainty during EHDA impingement cooling, the uncertainty during MJIC experiments is found higher. One possible reason is that MJIC experiments are conducted at much higher heat flux. Since the boiling process would be much severe than before, it is measured that the temperature fluctuation is much larger.

During the experiments of MJIC, measurement of CHF and temperature are same as that in EHDA impingement cooling (See Section 2.4). In order to achieve reliable results, three repeating tests are conducted in same condition. The average value and error bars would be shown in the final results.

During the test of MJIC, the CHF values are noticed changing from time to time. Besides the measurement error, heating surface properties is considered a major factor, which contributes a lot to the deviation.

1. Surface oxidization.

The heating surface is polished and looks shining when it is installed inside the chamber. As the tests going on, it becomes dark. That oxidization must happen on the surface and might affect its properties.

2. Physical or chemical reaction at impinging site

After testing, we could found black depositions at each impinging site. It might come from the reactions between impinging flow and hot copper surface. The reason is still not clear. And the darkness and size of deposition spots are growing during the testing, no matter with water, ethanol or HFE7000.

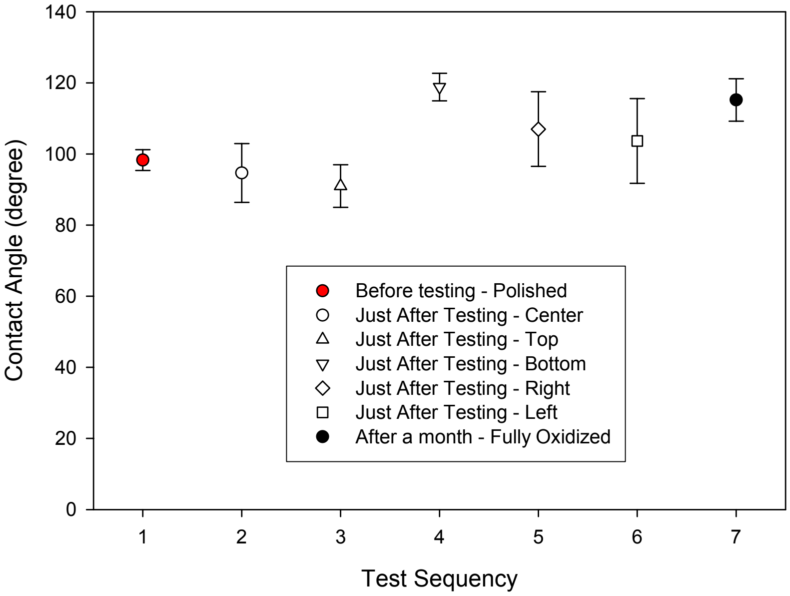

Fig. 42 Transition of contact angle during MJIC experiments

Since the surface becomes oxidized and has deposition during the testing, we are sure that the contact angle would change by a period of testing. The contact angle of water had been measured on testing surface at three different times. One is before the testing, one is right after the testing and one is after couple weeks. Before testing, their contact angles are at same level on the whole surface. The results of 5 spots on the heating surface changed irregularly when the surface brought to measure at right after testing. The local contact angle was increased at some spots and decreased at other places. After exposed in the air for a long time, the contact angle becomes uniform again. The results are shown in Fig. 42.

CHAPTER 7. EXPERIMENTAL RESULTS OF SINGLE MJIC

7.1 Fluids Effect on Single MJIC

We compared the effect of three different fluids (see Table 6 for property data) during the single MJIC experiment. Comparing with EHDA cooling tests, the testing flowrate in MJIC covers a quite wide range (10^{-8}~10^{-6} m3/s). The CHF results are obtained from three repeating tests.

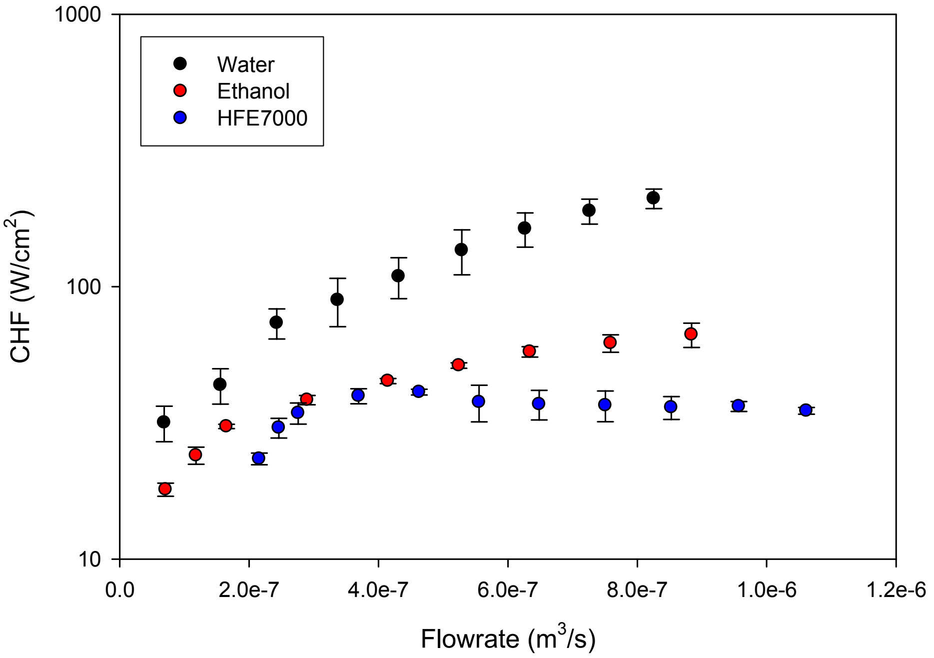

Fig. 43 CHF results during single micro jet impingement cooling with different fluids

From the CHF results shown in Fig. 43, we observed the following.

1. Water has the highest CHF, and HFE7000 has the lowest CHF at same flowrate.

2. CHF results with Ethanol have the smallest deviation than those of water or HFE7000

3. There exits an optimal flowrate in the CHF results of HFE7000, which is not the highest flowrate. The CHF under that optimal flowrate is quite repeatable, which has very small deviation.

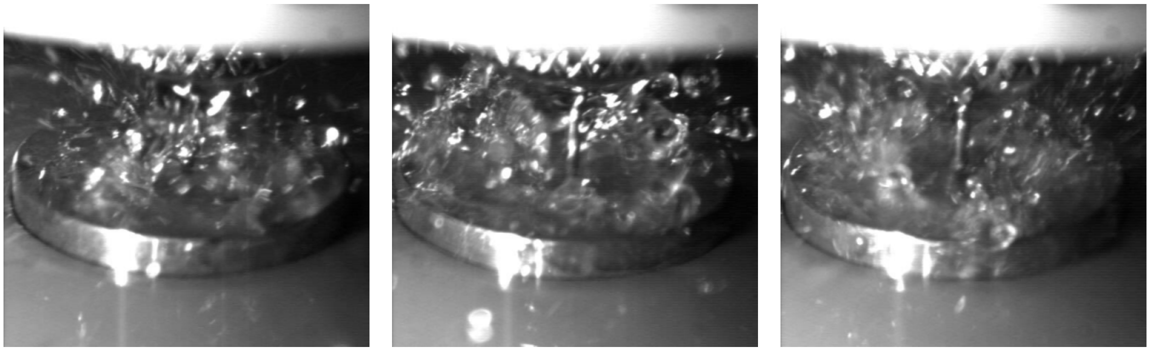

$We_d = 10$, $q''_{CHF} = 18$ W/cm^2 $Q = 7.1 \cdot 10^{-8} m^3/s$, $U_e = 1.4$ m/s

$We_d = 161$, $q''_{CHF} = 38$ W/cm^2 $Q = 2.9 \cdot 10^{-7} m^3/s$, $U_e = 4.9$ m/s

$We_d = 776$, $q''_{CHF} = 57$ W/cm^2 $Q = 6.3 \cdot 10^{-7} m^3/s$, $U_e = 12.9$ m/s

Fig. 44 Photos of single MJIC with ethanol at CHF condition

High speed images were not obtained for water because the view through the observation window was obstructed by water drops on the window. The images captured in experiments with ethanol, (See Fig. 44) show that:

1. At low flowrate, nucleate boiling occurs at the center of the surface. The liquid could not wet some part of surface near the edge at CHF condition.

2. At mid flowrate, most of surface is dominated by nucleate boiling, and the whole surface could be wetted completely at CHF condition.

3. At high flowrate, the nucleate boiling moves to outside part of the surface. The center part of surface has obvious difference with the outside regime, only small droplets could be observed occasionally.

Those high speed images would finally lead to develop a new CHF model, which would be addressed in the Chapter 8.

7.2 CHF Prediction by Existing Correlations for single MJIC

Five CHF correlations (See Table 13) are compared with the experimental CHF results of single MJIC with each type of fluids. The only correlation that is not selected is HP correlation, since the HP correlation was obtained and used in the high pressure condition (P_{sat} >>1 ATM). During the calculation, we choose the average temperature of surface temperature and liquid exiting temperature as the standard temperature to calculate all the properties. The results are shown in Fig. 45 - Fig. 47. We observed following.

1. As to water, Monde's I correlation matches with experimental results very well at the low flowrate. At higher flow rates, none of correlations are able to predict the CHF. Katto's predictions are extremely high as oppose to other correlations. Due to the density ratio is very high in saturated condition, the Ar(γ) become positive in Lienhard's correlation. So it is observed that the predictive CHF decreases with increasing flowrate.

2. For ethanol, Monde's L and I correlation was only valid for We (D-d) less than 5000. With increasing We number, the CHF data were located in between of V and I correlation. Other correlation would over predict the CHF results in the full range.

3. As for HFE7000, we observe that experimental CHF value does not simply increase as increasing the flowrate. The unique feature of the curve is that there exist a peak at We = 5×10^4. All the existing correlation show the simply increasing trend and could match with our testing results.

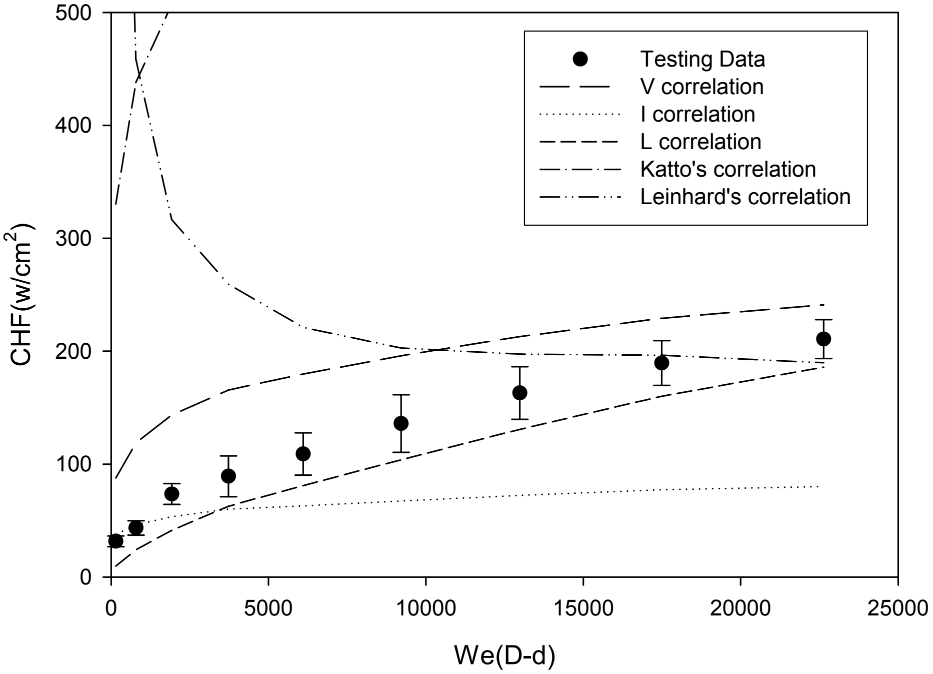

Fig. 45 CHF of single micro jet impingement cooling with water

Note: Properties are calculated under the saturated condition at temperature of $T_p = \frac{T_l + T_s}{2}$**.**

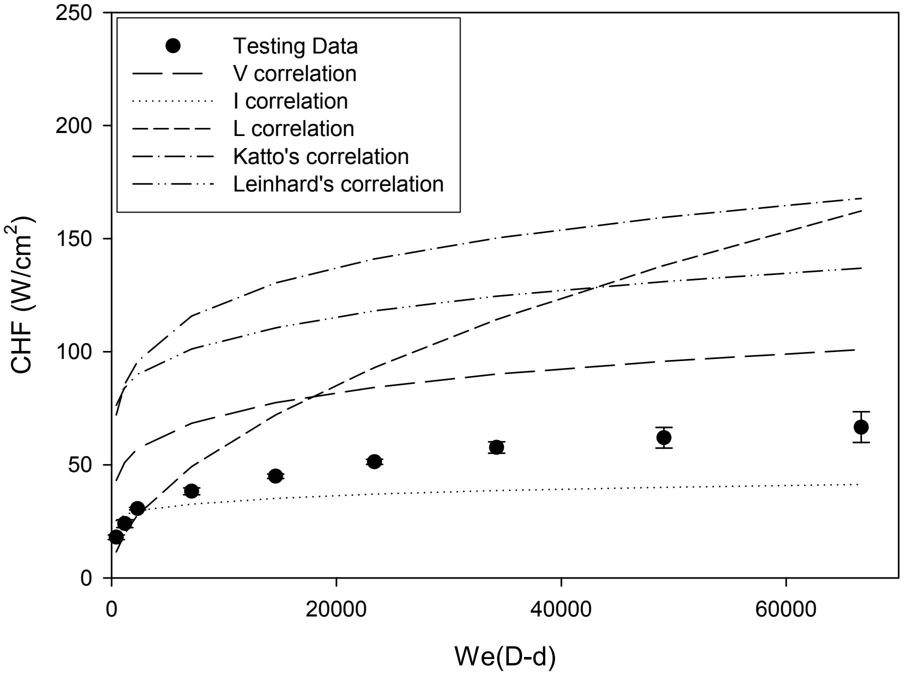

Fig. 46 CHF of single micro jet impingement cooling with ethanol

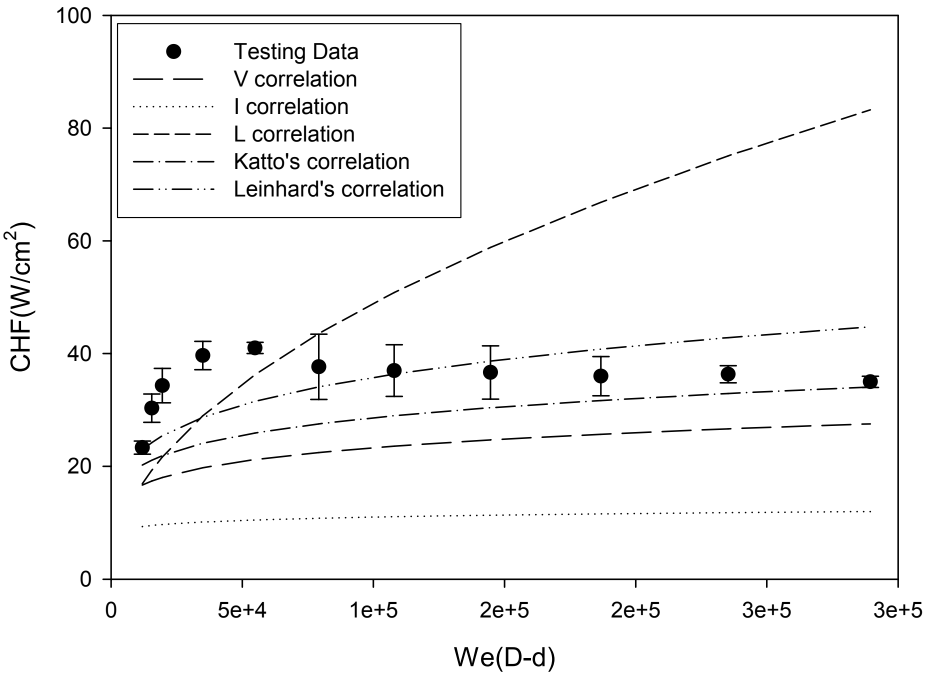

Fig. 47 CHF of single micro jet impingement cooling with HFE7000

From this comparison, it considered that the existing correlations could not predict the CHF in single MJIC at least for following reasons.

1. Though the forms of existing CHF correlations are based on the theoretical model, the coefficients in those correlations still relied on experimental results. Since most reported experiments were carried out in the atmosphere pressure, the term of density ratio would be much larger in our saturated condition as opposed to the traditional condition.

2. The second reason is due to the micro jet, which is one order of magnitude smaller than the nozzles that Monde, Katto and Lienhard had tested. The existing CHF models might not fit for the boiling situation of MJIC. It could generate much higher We Number at the same flowrate. Or it could reach the same level of

We number by much lower flowrate. In the next chapter we would address this problem with both experimental and analytical works.

During the test of HFE7000, the CHF is found dropping down when increasing the flowrate to a certain level. This phenomenon has not been found in previous researches, however, we do find the same CHF drop again during the testing with subcooled ethanol at 1 ATM. In the present study, we plan to propose an explanation for this phenomenon, which would be addressed the following chapters.

CHAPTER 8. DEVELOPMENT OF CHF CORRELATION FOR SINGLE MJIC

In the previous chapter, it was shown that existing correlations cannot predict the CHF correctly. In this chapter, a new CHF correlation will be proposed based on the assumption of two characteristic regimes on the impingement surface.

8.1 Regimes of two-phase heat transfer during microjet impingement

Three different fluids have been tested and during the experiments two different regions were observed as shown in Fig. 48 and Fig. 49. The selected images were obtained for ethanol and HFE 7000 right before CHF occurs. Images were not obtained for water because the view through the observation window was obstructed by water drops on the window. However, the two different regimes were observed with water as well. For a given fluid and jet configuration, the size of the two regions depended on volumetric flow rate and heat flux to the surface.

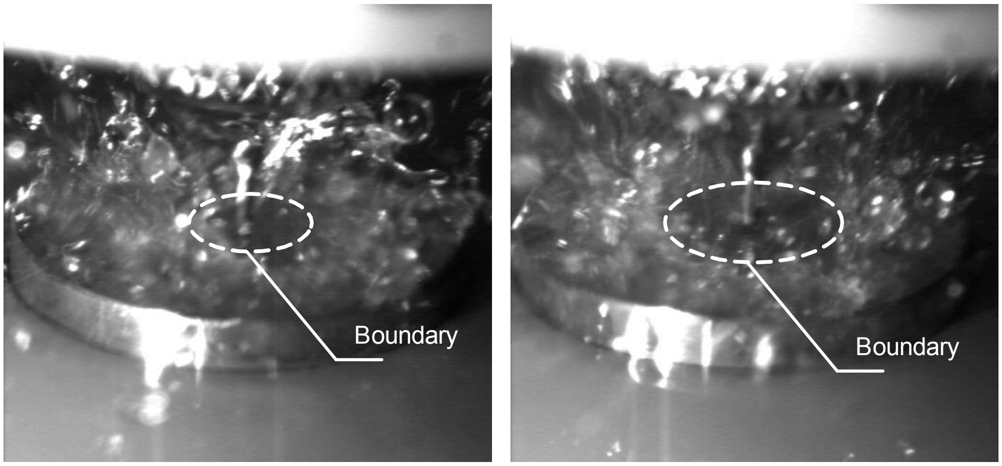

$Q = 2.9E\text{-}07\ m^3/s$, $q'' = 38\ W/cm^2$ $Q = 6.34E\text{-}07\ m^3/s$, $q'' = 57\ W/cm^2$

Fig. 48 High speed images of boiling near the CHF condition of ethanol

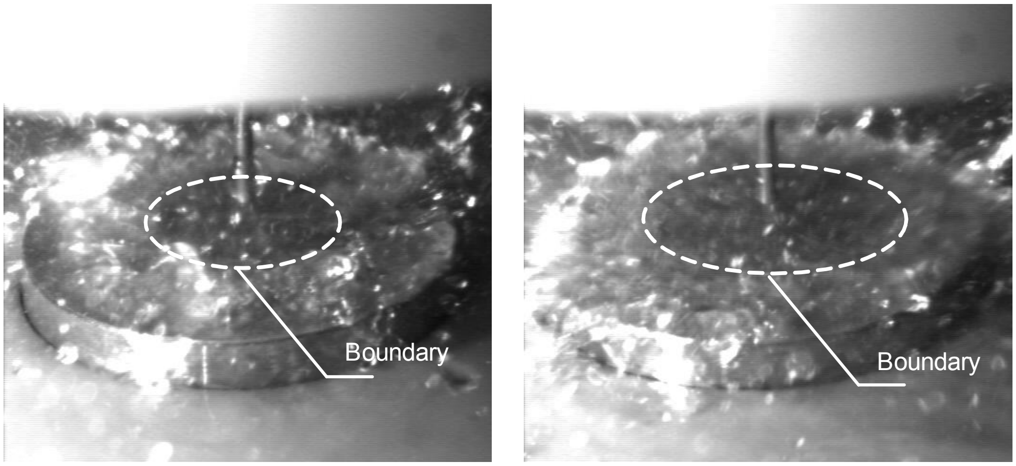

Q =4.63E-07 m^3/s, q" = 40 W/cm^2 Q =5.56E-07 m^3/s, q" = 38 W/cm^2

Fig. 49 High speed images of boiling near the CHF condition of HFE7000

A better understanding of the behavior at the surface under different conditions can be achieved by referring to the surface sketches shown in Fig. 50 and Fig. 51.

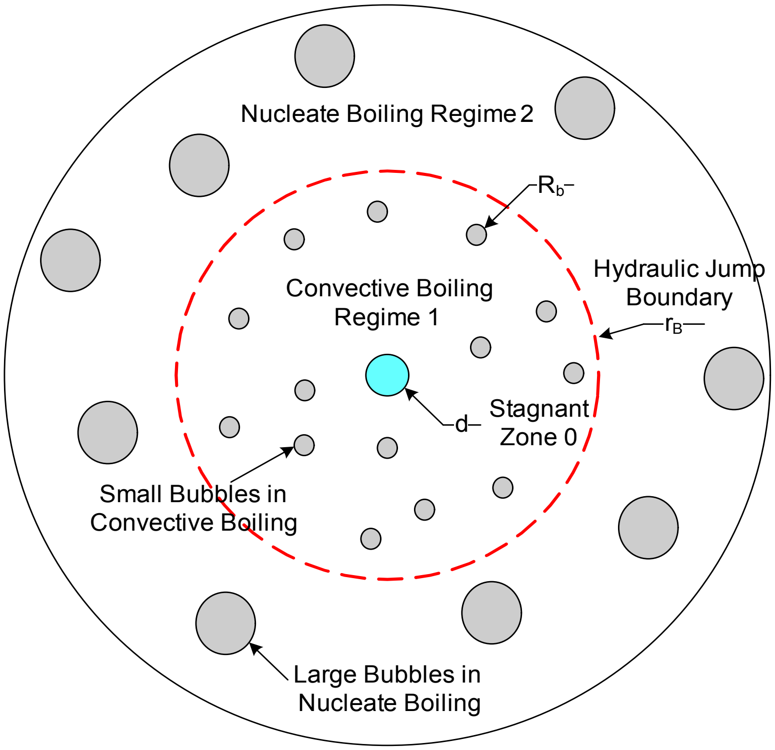

Fig. 50 Sketch of heat transfer regime near CHF condition

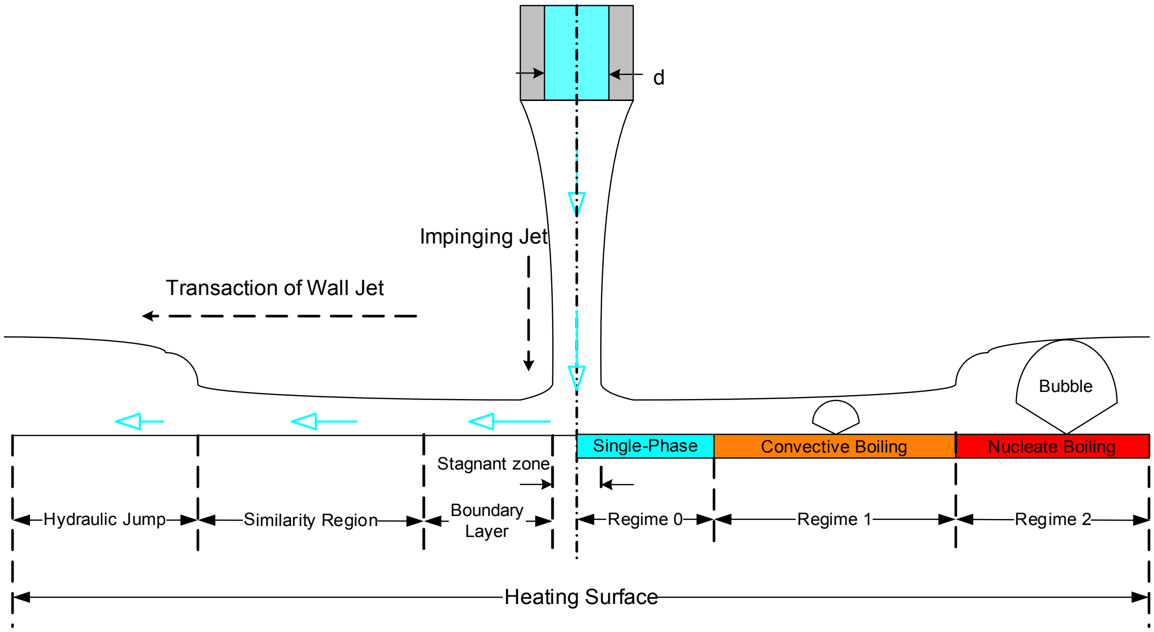

Fig. 51 Wall jet flow region of single jet impingement cooling

Table 18 Transition of wall jet during MJIC

Regime	Phenomena	Suspected wall jet region	Heat Transfer Form
Regime 0	No bubble	Stagnant Zone, Boundary Layer Region	Single-phase Convection
Regime 1	Small bubbles	Similarity Region	Convective Boiling
Regime 2	Large bubbles	Hydraulic Jump Region	Nucleate Boiling

After the liquid jet vertically impinging at the center of heating surface, most of its kinetic energy would be transferred into the wall jet, which moves in parallel with the surface. The wall jet would pass through several regions as summarized in previous studies [6]. (See Table 12 in Chapter 5) In order to compare with experimental observation, those regions are shown in the above sketch, such as the stagnant zone, boundary layer region, similarity region and hydraulic jump region.

At the surface center, stagnant zone is easily identified under the liquid jet. Then it enters the boundary layer region, which is characterized by the viscous boundary layer growing at the bottom of liquid sheet. The local heat transfer coefficient is very high due to the large velocity gradient inside the viscous boundary. Consequently, there is no bubble at the stagnant zone or the nearby region. This single phase area is named as regime 0 in the Fig. 50. And liquid momentum force and viscous force are dominating in this regime.

At the outside of regime 0, some small droplets and liquid ligaments are observed (See Fig. 50). Due to convective boiling dominating in this regime, it is called as regime 1. This regime is suspected to start from the similarity region in the Table 12. The reason is that, at the beginning of similarity region, the viscous boundary grows to the surface of the wall jet, which moderates the velocity gradient. Therefore, the local heat transfer coefficient is much lower than that in region 0, and the boiling process would take place at the bottom of wall jet. Since the liquid momentum or velocity remains strong at the top of the liquid sheet, vapor bubble would be removed when it grows and reach to top of the wall jet. Thus, convective boiling dominated in the regime and characterized by small bubbles. That means the dominating forces are liquid momentum force in the wall jet, vapor momentum and surface tension of the bubbles.

As the wall jet flows outwards, the liquid momentum drops quickly with the radius. The hydraulic jump would occur at the outside of regime 1, which has a relative clear boundary. In Fig. 51, it is named as regime 2 for the area between that boundary and the edge of heating surface. Since the liquid momentum losing its dominant position, vapor momentum and surface tension become the dominant forces in this regime, it is considered that boiling process would be similar with the nucleate boiling during traditional jet impingement cooling. In this regime, the wall jet thickness depends on vapor bubbles, which could grow up to a large level (10^{-3} m from high speed images). It is much larger than that in regime 1.

8.2 Analysis of wall jet during Single MJIC

There are two major differences in the two-phase impingement heat transfer observed in this research with microjets compared to prior jet impingement research. The first one is the jet diameter. The jet diameter in our testing condition is one order of magnitude smaller than the traditional jets[7, 56, 68]. The second difference is that our testing is conducted at saturated environment (T_{sat} closes to room temperature). Many of traditional studies were done in subcooled environment[7, 8] or saturated environment with $P_{sat} \geq 1$ ATM[56].

8.2.1 Film thickness of wall jet generated by micro jet impingement

According the mass balance along the wall jet, the film thickness of wall jet would directly link with the jet velocity. It is necessary to study the velocity profile during three regimes that we identified in previous section. Fig. 52 is a sketch of the jet flow during MJIC. Three velocity profiles are presented three areas that we talk about in the previous section.

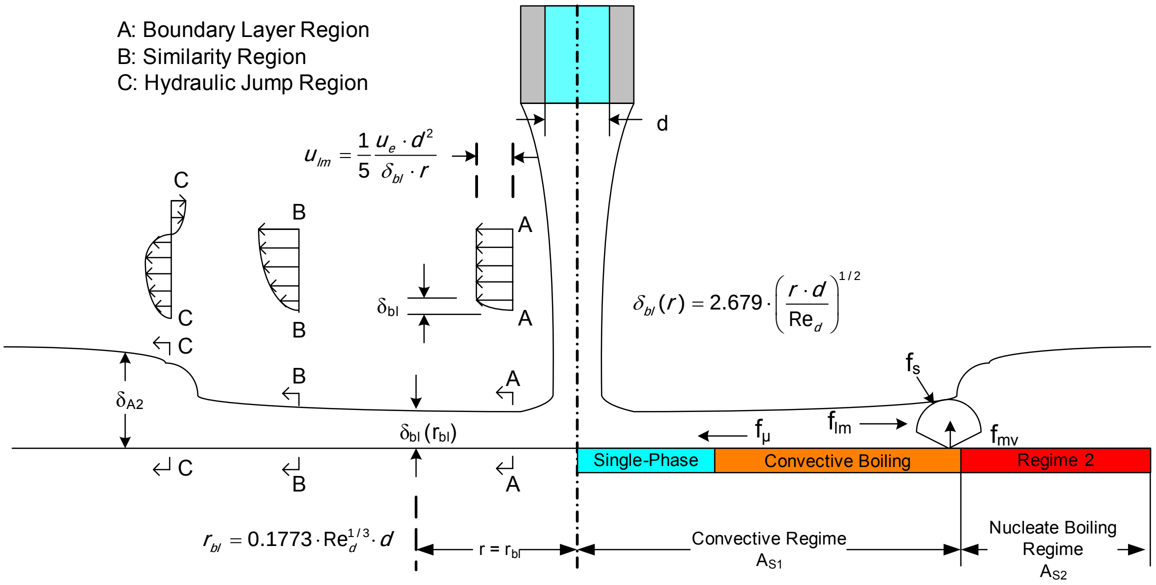

Fig. 52 Transition of velocity profiles in wall jet

In regime 0 (See A-A), the boundary layer region is located at outside of stagnation zone[6]. The upper part of wall jet moves with the incoming velocity U_e. Close to the surface, there is a viscous boundary layer with thickness of δ_{bl} which is less than the thickness of the liquid wall jet δ(r).

$$\delta_{bl} = 2.679 \cdot \left(\frac{r \cdot d}{\mathrm{Re}_d}\right)^{1/2} \tag{17.1}$$

where: r is the distance between a given location to the center line of the impinging jet

d is the liquid jet diameter, assumed the same as nozzle inside diameter D_i

Re_d is the Reynolds Number of the impinging jet with the characteristic length, d.

This region would end at r_{bl}, where the viscous boundary layer reaches the surface of the liquid sheet.

$$r_{bl} = 0.1773 \cdot \mathrm{Re}_d^{1/3} \cdot d \tag{17.2}$$

In regime 1 (See B-B), the wall jet enters viscous similarity region. The boundary layer has reached the top of the liquid surface. And the wall jet moves like a half of fully developed flow. In this region, the surface speed u_m decreases with the increasing radius. Lienhard recommended a correlation to calculate the wall jet thickness outside of the boundary layer region.

$$\frac{\delta(r)}{d} = 0.1713 \cdot \left(\frac{d}{r}\right) + \frac{5.147}{\mathrm{Re}_d} \cdot \left(\frac{r}{d}\right)^2 \tag{17.3}$$

In regime 2 (See C-C), the hydraulic jump cause an irregular velocity profile. The classical solution for hydraulic jump region is developed with effect of gravity force. It would be not fit in the two-phase boiling situation.

Using the equation(17.3), the film thickness at r_{bl} is calculated for the conditions investigated in this work. In order to illustrate the effect of jet diameter on film thickness, a traditional jet d = 2.5mm with same incoming velocity is also considered. The film thickness is much thinner for the microjet compared to the conventional jet, as shown in Fig. 53.

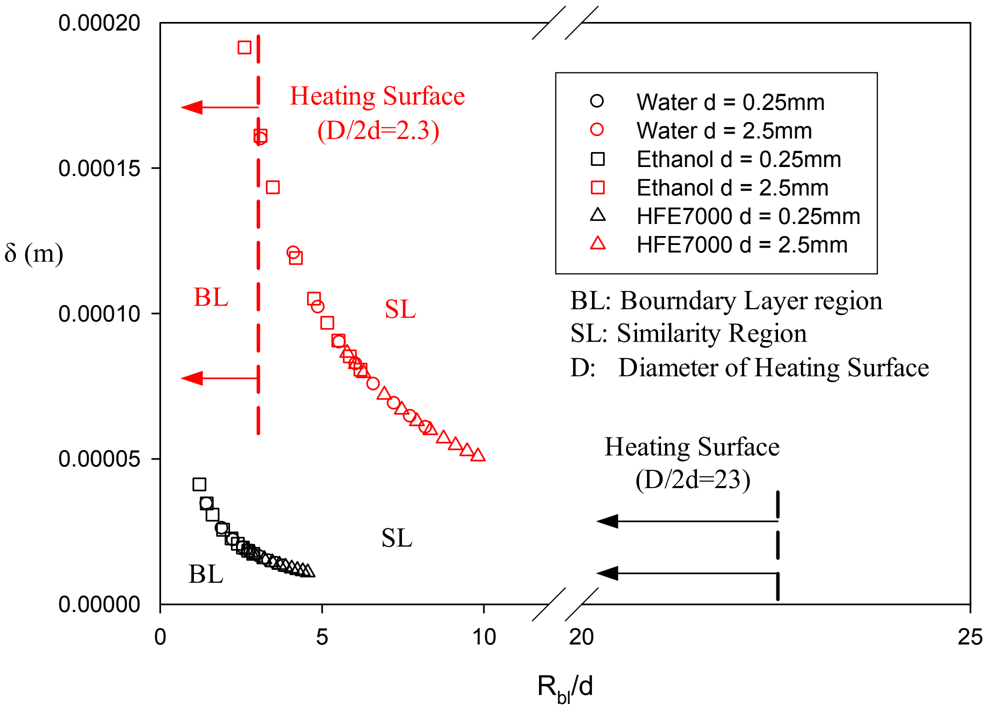

Fig. 53 Effect of jet diameter on film thickness of wall jet on 1 cm diameter surface

The two jets (0.25mm and 2.5mm) considered impinge on the same size 1cm diameter surface. The results in the Fig. 53 indicate following:

1. The film thickness of traditional wall jet is much thicker than that of micro jet. In our testing range, the film thickness of wall jet is about 10^{-5} m, which is nearly one order magnitude thinner than the traditional wall jet.

2. The heating surface (A_s =1 cm^2) would be covered by different wall jet regions when using two types of jets. For impinging with a large nozzle (d = 2.5mm), the ratio of D/d is smaller than most ratios of R_{bl} /d. That means the heat surface is most likely occupied by boundary layer region during traditional jet impingement cooling. In case of MJIC, the ratio of D/d is much larger than the ratio of R_{bl} /d, which means that the area of boundary

layer region is significant smaller than the area of heating surface. In other words, most of heating surface is covered by flow in similarity region and other regions during MJIC. Therefore the size of boundary layer region is negligible as opposed to the heating surface. When we develop the CHF correlation, the surface would only classified into two regimes instead of three. The regime 0 would be included in regime 1.

8.2.2 Liquid and vapor density ratio in saturated environment

The testing pressure would causes large difference because the vapor density highly depends on the environment pressure, or in saturated condition, it depends on saturated temperature.

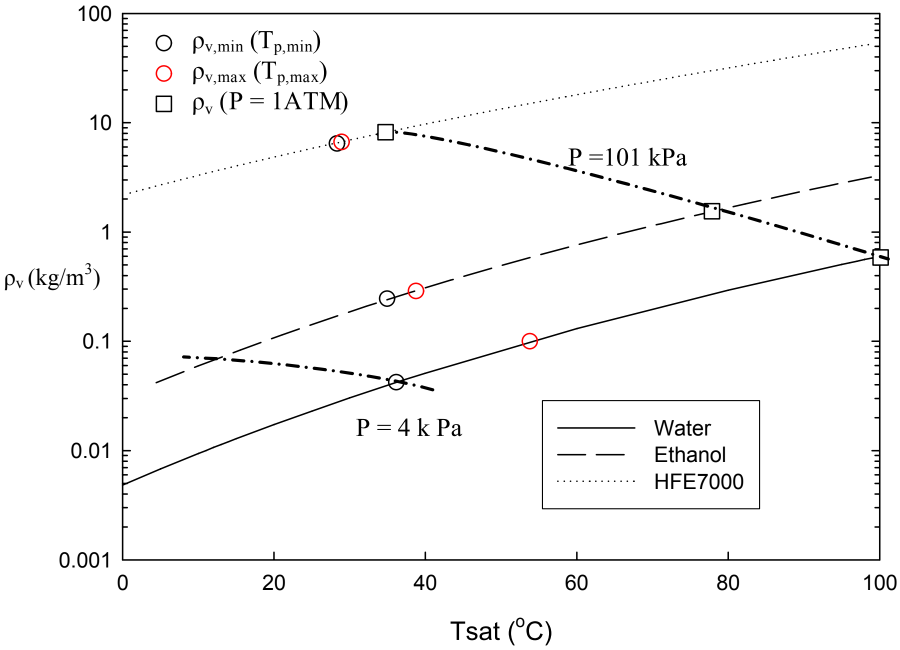

Fig. 54 Effect of saturated temperature on vapor density

Fig. 54 shows the vapor density changes in our testing conditions, which is determined by the saturated vapor temperature, $T_p = \frac{T_l + T_w}{2}$. In the figure, the black and red circles are the minimum and maximum vapor density during the CHF testing with a specific fluid. As a reference, the vapor density at 1 ATM condition is illustrated, too. It is obvious that vapor density at atmosphere pressure (P = 1 ATM) is almost one order of magnitude larger than that in our testing conditions, especially for water and ethanol. Since the liquid density has little difference between our testing condition and 1 ATM, the density ratio γ would be much higher in the saturated condition with room temperature of T_{sat}. That might be one factor influence the results by using traditional CHF correlation to predict CHF of MJIC, since many CHF correlations are based on testing in 1 ATM or even higher pressure condition.

During the current testing condition, it is found that the vapor density could change significantly during the MJIC with water. The density ratio is about doubled by comparing the maximum and minimum condition. On the other hand, for HFE7000 and ethanol, their density ratios are holding at a same level during the testing. In the study, this effect would be taken into account, which finally helps to improve the prediction (See section 8.5).

8.3 Thermal bridge analysis for heat transfer around heater

Since the regime 0 is proved negligible in the previous section, the nature of CHF would mainly depend on the heat transfer in regime 1 and 2. Therefore, it is necessary to determine the measurable CHF with respect to the heat transfer in the other two regimes. That helps to link the experimental data with the theoretical analysis and CHF correlation.

The thermal bridge at the heated surface will be the basis of the CHF correlation to be developed. In Fig. 55, a thermal bridge is presented showing the heat transfer from a thick film heater to the fluid during MJIC.

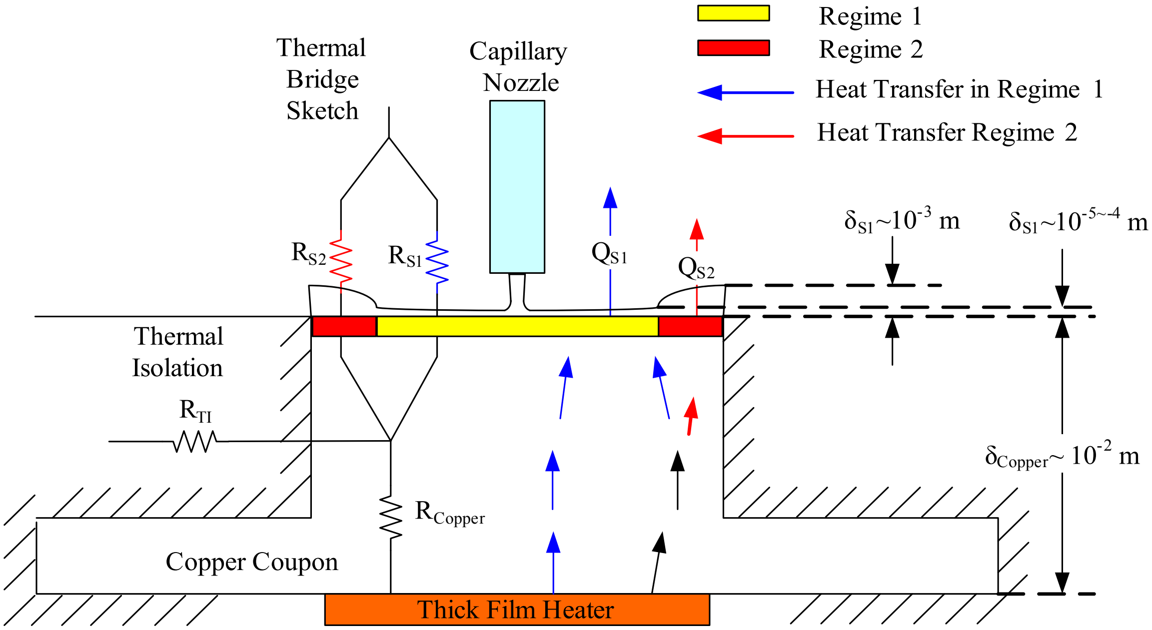

Fig. 55 Thermal Bridge Sketch of Single MJIC

Close to the CHF condition, the total heat transfer generated from the thick film heater could have three paths to the ambient environment. The first pass is to go through the copper coupon and dissipated in regime 1 (including area 0). The second one is to go through the coupon and regime 2. The third one is heat loss pass to the surround media. As discussed in Chapter 2, the heat loss to the surrounding medium is negligible, so heat transfer occurs primarily through Regime 1 and 2. The heat transfer through regime 1 and 2 at the surface can be expressed as:

$$Q = Q_{s1} + Q_{s2} \tag{17.4}$$

where Q_{S1} and Q_{S2} is the energy transfer through the regime 1 and regime 2.

The two-phase heat transfer in the two regimes is quite different, based on the discussion in the previous sections. R_{S1} and R_{S2} are used to express the thermal resistance of the two-phase heat transfer in the two regimes and are functions of local heat flux. Using R_{S1} and R_{S2}, Q_{S1} and Q_{S2} can be defined as following:

$$Q_{s1} = \frac{A_{s1} \cdot \Delta T_{s1}}{R_{s1}} \tag{17.5}$$

$$Q_{s2} = \frac{A_{s2} \cdot \Delta T_{s2}}{R_{s2}} \tag{17.6}$$

where A_{S1} and A_{S2} and ΔT_{S1} and ΔT_{S2} represent the area and superheat of regime 1 and 2, respectively.

The average heat flux in each regime could be expressed as $q''_{s1} = \frac{Q_{S1}}{A_{s1}}$ and $q''_{s2} = \frac{Q_{s2}}{A_{s2}}$.

So the average heat flux over the whole surface could be expressed as:

$$q'' = \frac{Q}{A} = \frac{Q_{s1} + Q_{s2}}{A} = \frac{A_{s1}}{A} q_{s1}'' + \frac{A_{s2}}{A} q_{s2}'' \tag{17.7}$$

Using F_{A1} to express the area percentage of inside region, following equation could be obtained by rewriting the equation(17.7).

$$q'' = F_{A1} \cdot q_{s1}'' + (1 - F_{A1}) \cdot q_{s2}'' \tag{17.8}$$

where

$$F_{A1} = \frac{A_{s1}}{A}\;.$$

For the test configuration used in this work, see Fig. 12 and Fig. 13, the magnitude of heat flux through each regime will depend on the thermal resistance in that region. The thermal resistance will be a function of the fluid type, impingement conditions (flow and jet geometry), and overall heat flux. Critical heat flux will be reached when the resistance in both regions reaches a critical limit. Before this occurs the thermal transportation through the copper coupon will redistribute based on the surface thermal resistances.

Thus the CHF at the copper coupon surface becomes

$$q''_{CHF} = F_{A1} \cdot q''_{s1,CHF} + (1 - F_{A1}) \cdot q''_{s2,CHF} \qquad (17.9)$$

In the equation above, the general CHF of the surface is expressed as three factors, such as the area percentage of regime 1 and two maximum heat fluxes. It would be discussed in the follow sections how to determine three important factors in the equation (17.10).

8.4 Development a new CHF Correlation

8.4.1 Define the Boundary between regime 1 and regime 2

In order to determine the area percentage of regime 1 at the CHF condition, the boundary between two regimes must be estimated. In Fig. 56, it is shown that 4 fundamental forces in the regime 1. Those fundamental forces would be analyzed in order to determine the boundary between regime 1 and 2. In the generic

Table 19, four fundamental forces are listed with respect to the flow regime.

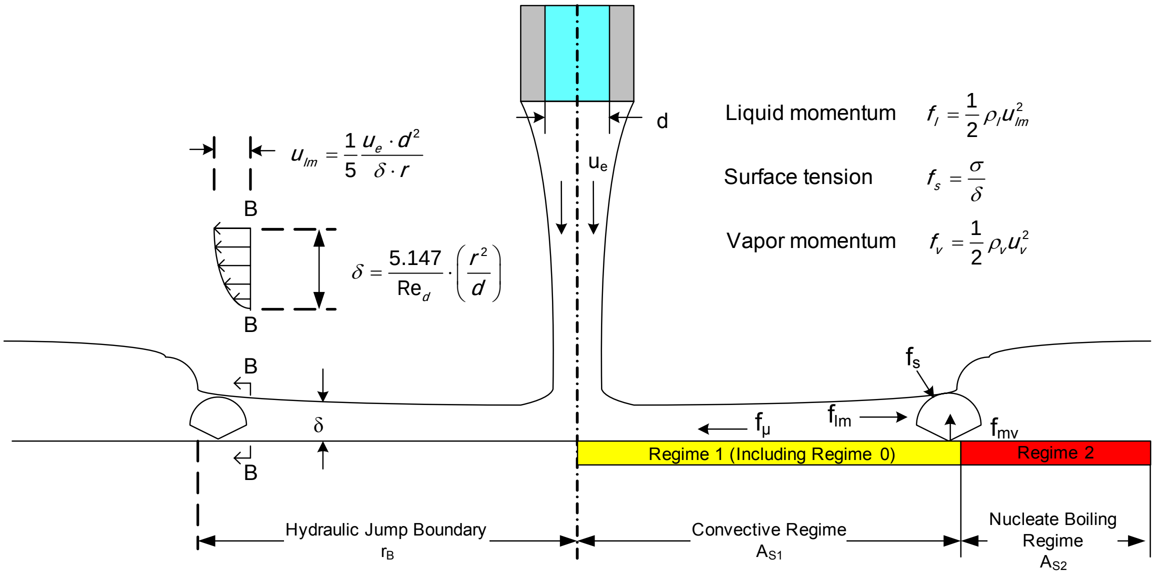

Fig. 56 Fundamental forces near the boundary of two regimes

Table 19 Fundamental Forces in two regimes during MJIC

	f_{mv}	f_{ml}	f_s	f_{vis}
Regime 1	Strong	Strong	Strong	Weak
Regime 2	Strong	Weak	Strong	Weak

Since the liquid momentum force is decreased to a critical level at the boundary, so that its local intensity is on a same level as vapor momentum and surface tension. That yields the following relationship at the boundary, r_b.

$$f_{ml} \sim f_{mv} \sim f_s \tag{17.11}$$

In this study, the momentum force is assumed equal to the surface tension at the boundary.

$$P_l = P_s \tag{17.12}$$

The liquid momentum force could be expressed as

$$P_l = \frac{1}{2}\rho_l u_{lm}^2 \tag{17.13}$$

The surface tension could be expressed as

$$P_s = \frac{\sigma}{\delta(r_b)} \tag{17.14}$$

The following equation is easily obtained by substituting (17.13) and (17.14) into (17.12)

$$\frac{1}{2}\rho_l \cdot u_{lm}^2 = \frac{\sigma}{\delta(r_b)} \tag{17.15}$$

So it is needed to calculate the liquid velocity and film thickness in order to determine the boundary between regime 1 and 2. Based the classical solution of boundary layer region and similarity region [6], the velocity profile in the boundary layer region is approximately:

$$u(r,z) = u_{lm}(r)\left[\frac{3}{2}\frac{z}{\delta_{bl}(r)} - \frac{1}{2}\left(\frac{z}{\delta_{bl}(r)}\right)^3\right] \tag{17.16}$$

where r is the distance between a given location to the center line of the impinging jet

z is the distance between a given location to the copper surface.

δ_{bl} is the viscous boundary layer with thickness (See equation (17.1))

The maximum flow velocity is above the boundary layer, which could be expressed as:

$$u_{lm} = \frac{1}{5}\frac{u_e \cdot d^2}{\delta_{bl} \cdot r} \tag{17.17}$$

Where: U_e is the incoming jet velocity.

Out of boundary layer region, the viscous boundary layer reaches the surface of the liquid film, and the velocity profile could adopt the same equation with δ_{bl} replaced by the liquid film thickness δ(r).

$$\delta(r) = 0.1713 \cdot \left(\frac{d^2}{r}\right) + \frac{5.147}{\mathrm{Re}_d} \cdot \left(\frac{r^2}{d}\right) \tag{17.18}$$

The velocity profile has a similar form:

$$u(r,z) = u_{lm}\left[\frac{3}{2}\frac{z}{\delta(r)} - \frac{1}{2}\left(\frac{z}{\delta(r)}\right)^3\right] \tag{17.19}$$

And flow velocity at the surface of liquid film is approximately:

$$u_{lm} = \frac{1}{5}\frac{u_e \cdot d^2}{\delta(r) \cdot r} \tag{17.20}$$

In order to simplify the problem, we would neglect the first term in equation (17.18) due to our working condition. By simple calculation, that equation could be reduced as long as:

$$\mathrm{Re}_d << 30.05 \cdot \left(\frac{r}{d}\right)^3 \tag{17.21}$$

Assuming it qualifies in our testing condition first, and we will check the assumption after we calculate the boundary r_b. So we get the simplified equation of film thickness:

$$\delta(r) = \frac{5.147}{\mathrm{Re}_d} \cdot \left(\frac{r^2}{d}\right) \tag{17.22}$$

Substituting the equation(17.22) into the equation(17.20) yields the maximum flow velocity as following:

$$u_{lm} = \frac{u_e \cdot \mathrm{Re}_d}{25.735} \cdot \left(\frac{d}{r}\right)^3 \tag{17.23}$$

Known the relationship between wall jet velocity and location, the following equation could be obtained by using the velocity distribution equation (17.23) and film thickness equation (17.22) into equation (17.24):

$$\frac{1}{1325} \cdot \rho_l u_e^2 \mathrm{Re}_d^2 \cdot \left(\frac{d}{r_b}\right)^6 = \frac{\sigma}{5.147} \mathrm{Re}_d \left(\frac{d}{r_b^2}\right) \tag{17.25}$$

Rearranging the equation above, we obtain the boundary of regime 1 in form of following equation:

$$\frac{r_b}{d} = \frac{1}{4.005} \cdot \left(We_d \cdot \mathrm{Re}_d\right)^{1/4} \tag{17.26}$$

Using the above equation, it is able to check our previous assumption about the film thickness. By substitute the equation (17.26) in to the equation(17.21), we get

$$\frac{\mathrm{Re}_d}{We_d^3} << 0.0478 \tag{17.27}$$

By calculating the ratio in our testing range (U_e: 1.5 ~ 22 m/s), we found it is valid in most conditions (U_e > 4 m/s), except for very few conditions with the lowest flowrate (U_e: 1.5 ~ 3 m/s). Since we are more interested in situations with higher flowrate and higher energy transfer, the assumption could be acceptable.

As the boundary between regime 1 and regime 2 is known, the size of regime 1 could be calculated as

$$A_{s1} = \pi \cdot r_b^2 = \frac{\pi \cdot d^2}{16.04} \cdot We_d^{1/2} \cdot \mathrm{Re}_d^{1/2} \tag{17.28}$$

When the boundary is inside the heating surface, we could calculate, F_{A1}, the area percentage of regime 1 over the whole heating surface as following:

$$F_{A1} = \frac{A_{s1}}{A} = \frac{1}{4.01} \cdot We_d^{1/2} \cdot \mathrm{Re}_d^{1/2} \cdot \left(\frac{d}{D} \right)^2 \tag{17.29}$$

In case that the boundary of region is large enough to exceed the heating surface, it is obvious that the regime 1 occupies 100% of the heating surface. In other words, we have:

$$A_{s1} = \frac{\pi \cdot D^2}{4} \text{ or } F_{A1} = 1 \tag{17.30}$$

8.4.2 CHF correlation in regime 1

It is suitable to use presented the local heat flux as a function of vapor momentum force, in stead of other fundamental forces. Because most of heat is remove in form of vapor bubbles. The growing speed of a single bubble indicates the intensity of the vapor momentum forces. Since the boiling process is assumed uniform in regime 1, it means the vapor momentum force might be same over the regime 1. Therefore it is possible to represent the heat flux in regime 1 by choosing the vapor momentum force at a specific location. A good location is right inside the boundary. In that boundary, it is considered that the surface tension of bubbles is at same level of the vapor momentum force. That means the force balance equation could be expressed as following:

$$P_s = P_v \tag{17.31}$$

Where:

$$P_v = \frac{1}{2} \rho_v u_v^2 \tag{17.32}$$

To calculate the vapor momentum force, it is needed to consider the heat transfer process around a single bubble. (See Fig 48)

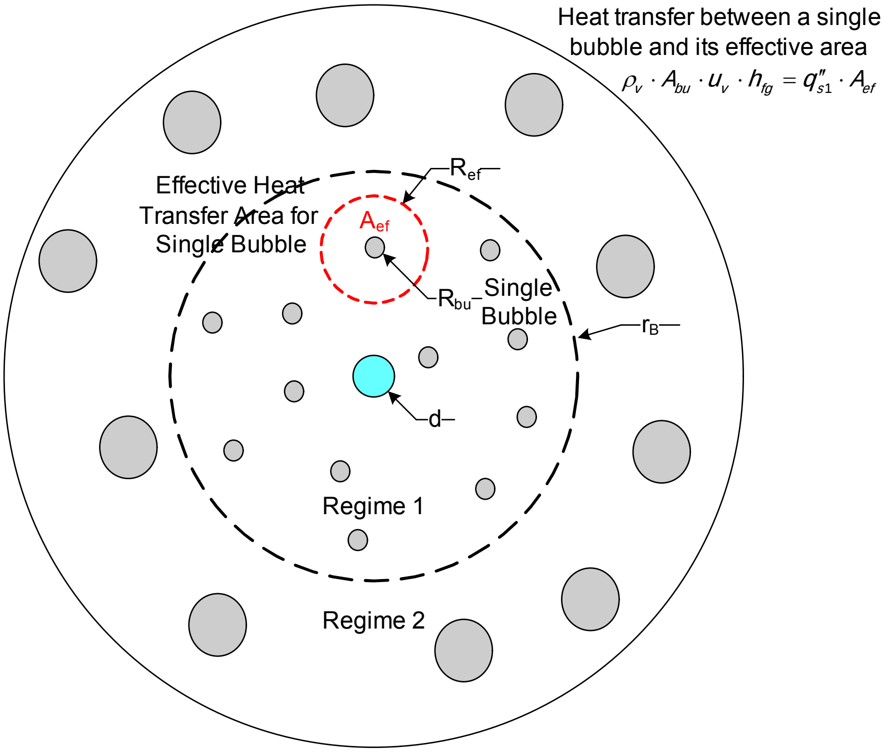

Fig. 57 Sketch of heat transfer of a single bubble in regime 1

In that situation, a single bubble is growing by absorbing the heat from its surrounding area. So the growing speed of the bubble could be calculated by the heat flux from the surrounding effective area.

$$\rho_v \cdot A_{bu} \cdot u_v \cdot h_{fg} = q''_{s1} \cdot A_{ef} \tag{17.33}$$

where: A_{ef} is the effective area of single bubble $A_{ef} = \pi \cdot R_{ef}^2$

A_{bu} is the surface area of hemisphere bubble $A_{bu} = 2\pi \cdot R_{bu}^2$

U_v is the bubble growing speed

h_{fg} is the latent heat

Thus the velocity of bubble would be expressed as:

$$u_v = \frac{q''_{s1} \cdot A_{ef}}{\rho_v \cdot h_{fg} \cdot A_{bu}} \tag{17.34}$$

Substitute the above equation into equation (8.31), we get:

$$P_v = \frac{1}{2}\rho_v \cdot \left(\frac{q''_{s1}}{\rho_v \cdot h_{fg}} \frac{A_{ef}}{A_{bu}} \right)^2 = \frac{1}{2}\rho_v \left(\frac{A_{ef}}{A_{bu}} \right)^2 \left(\frac{q''_{s1}}{\rho_v \cdot h_{fg}} \right)^2 \tag{17.35}$$

As to the surface tension, we get its form in equation (8.22). The following equation could be obtained by substituting the film thickness (8.18) into (8.22):

$$P_s = \frac{\sigma}{5.147} \cdot \mathrm{Re}_d \cdot \left(\frac{d}{r_b^2} \right) \tag{17.36}$$

Substitute the equations (8.35) and (8.36) into the force balance equation (8.30), we get:

$$\frac{1}{2}\rho_v \left(\frac{A_{ef}}{A_{bu}} \right)^2 \left(\frac{q''_{s1}}{\rho_v \cdot h_{fg}} \right)^2 = \frac{\sigma \cdot \mathrm{Re}_d}{5.147} \cdot \left(\frac{d}{r_b^2} \right) \tag{17.37}$$

By rearranging the equation, we could get:

$$\frac{q''_{s1}}{\rho_v \cdot h_{fg}} = \left(\frac{A_{bu}}{A_{ef}} \right) \cdot \left(\frac{2\sigma \cdot \mathrm{Re}_d}{\rho_v 5.147} \cdot \left(\frac{d}{r_b^2} \right) \right)^{1/2} \tag{17.38}$$

By dividing U$_e$ at both sides, the equation above could be expressed as:

$$\frac{q''_{s1}}{\rho_v \cdot h_{fg} \cdot u_e} = \frac{2}{5.147} \left(\frac{A_{bu}}{A_{ef}} \right) \cdot \left(\frac{\rho_l}{\rho_v} \right)^{1/2} \cdot \mathrm{Re}_d^{1/2} \cdot \left(\frac{\sigma}{\rho_l u_l^2 d} \right)^{1/2} \cdot \left(\frac{d}{r_b} \right) \tag{17.39}$$

Using (17.26), we get the nondimensional CHF equation in regime 1:

$$\Phi_{s1} = 1.556 \cdot \left(\frac{A_{bu}}{A_{ef}} \right) \cdot \gamma^{1/2} \cdot \mathrm{Re}_d^{1/4} \cdot We_d^{-3/4} \tag{17.40}$$

When the bubble grows and reaches the top surface of the wall jet, we can get:

$$\frac{A_{bu}}{A_{ef}} = \frac{2\pi \cdot R_{bu}^2}{\pi \cdot R_{ef}^2} = 2\left(\frac{R_{bu}}{R_{ef}} \right)^2 = 2\left(\frac{\delta\left(r_b\right)}{R_{ef}} \right)^2 \tag{17.41}$$

The area ratio is influenced by surface tension, wetting characteristic. If we simply assume $R_{ef} = 4.47\ \delta(r_b)$, the equation (17.41) would become:

$$\frac{A_{bu}}{A_{ef}} = \frac{1}{10} \tag{17.42}$$

By substitute this equation (17.42) into (17.40), The final form of CHF correlation in regime 1 would be expressed as following:

$$\Phi_{s1} = 0.1556 \cdot \gamma^{1/2} \cdot \mathrm{Re}_d^{1/4} \cdot We_d^{-3/4} \tag{17.43}$$

8.4.3 CHF correlation in regime 2

In regime 2, the hydraulic jump causes the liquid film much thicker. The boiling bubbles could be much larger than that in the regime 1. At the high heat flux, the strong vapor momentum makes the bubble in form of a large hemisphere [69]. The secondary flow generated by the bubbles, helps to supply and wet the temporary dry-out surface. It is believed that the CHF mechanism in regime 2 is similar to the traditional jet impingement cooling due to thick liquid film and large bubbles. Therefore, it would be reasonable to select one of the existing CHF correlations in Table 13 to describe the maximum heat flux in the regime 2. Monde developed four CHF correlations for different situation during impingement cooling.

1. The V-Correlation could be used in velocity dominating conditions. In other words, the CHF would be obviously effect by increasing the velocity. That is different from the feature of regime 2, where the liquid momentum is very weak.
2. The L-Correlation was suggested to use in a special condition, large D/d ratio. In that correlation, the incoming velocity still plays a big role.
3. The HP-Correlation was particularly developed for the high pressure condition. In that kind of environment, the vapor density could be much high so that the vapor momentum would be reduced.
4. The I-Correlation could be applied in the condition that CHF is not sensitive with velocity. That means the momentum force of liquid flow is not the dominating factor in that situation. It is consider that I-correlation is the right correlation that fits into the condition in regime 2.

8.4.4 Maximum heat flux and area percentage during our testing condition

After obtaining the maximum heat flux in each region, it is worth evaluating their value in the experimental conditions. We're also interested in how the size of regime 1 changes as increasing the incoming velocity. Thereafter, we could assemble them to compare with the experimental results and other CHF correlations. The equations of area percentage and maximum heat flux are listed in the Table 20

Table 20 Maximum heat flux and Area Percentage

Area	Area Percentage	Maximum Heat Flux correlations
1	$\frac{1}{4.01}\cdot\left(We_d\cdot\mathrm{Re}_d\right)^{1/2}\cdot\left(\frac{d}{D}\right)^2$	$\Phi_{s1}=0.1556\cdot\gamma^{1/2}\cdot\mathrm{Re}_d^{1/4}\cdot We_d^{-3/4}$
2	$1-\frac{1}{4.01}\cdot\left(We_d\cdot\mathrm{Re}_d\right)^{1/2}\cdot\left(\frac{d}{D}\right)^2$	$\Phi_{s2}=0.691\cdot\gamma^{0.466}\cdot We_d^{-0.421}\cdot\left(\frac{d}{D+d}\right)^{0.303}$

The area percentage of regime 1 and two maximum heat fluxes are calculated in our testing condition. The results are shown in the Fig. 58 - Fig. 60. We observe following:

1. The area percentage of regime 1 would grow as increasing the We number. In our testing range, the values for water and ethanol would reach about 30% at their maximum flowrate. That means the regime 2 occupies most surface area during the testing. While for the HFE7000, the percentage could exceed 50 % in most of its testing condition, and reach 100% at its maximum flowrate. That means the regime 1 occupies most surface area in most situations.

2. The maximum heat flux in regime 2 is based on the I-correlation developed by Monde. Their curve trends are very similar for three types of fluids. Each curve increases very slightly as increasing the flowrate. Those CHF values on the curve are small as opposed to the maximum heat flux in regime 1.

3. The maximum heat flux in regime 1 has a different trend from the maximum heat flux regime 2. It would decrease as increasing the flowrate in most cases, such as ethanol and HFE7000. By analysis the maximum heat flux equation (17.43), we could find $q''_{s1,CHF} \sim u_e^{-1/4}$, the maximum heat flux in regime 1 would drop down by the increasing the incoming velocity. As to water, the CHF in the regime 1 is holding at about 550 W/cm^2 in most conditions. Only at very low flowrate, CHF is a little bit higher. The reason we consider is due to the fluid properties, which has been discussed the previous sections. The fluid properties are calculated under the saturated condition at temperature of $T_p = \frac{T_l + T_w}{2}$. Since the wall super heat is much high for wall impingement cooling,

significant effect of the vapor density would contribute to offset the CHF in regime 1. (See Fig. 54 in section 8.2). That finally makes the curve flatter than those of ethanol and HFE7000.

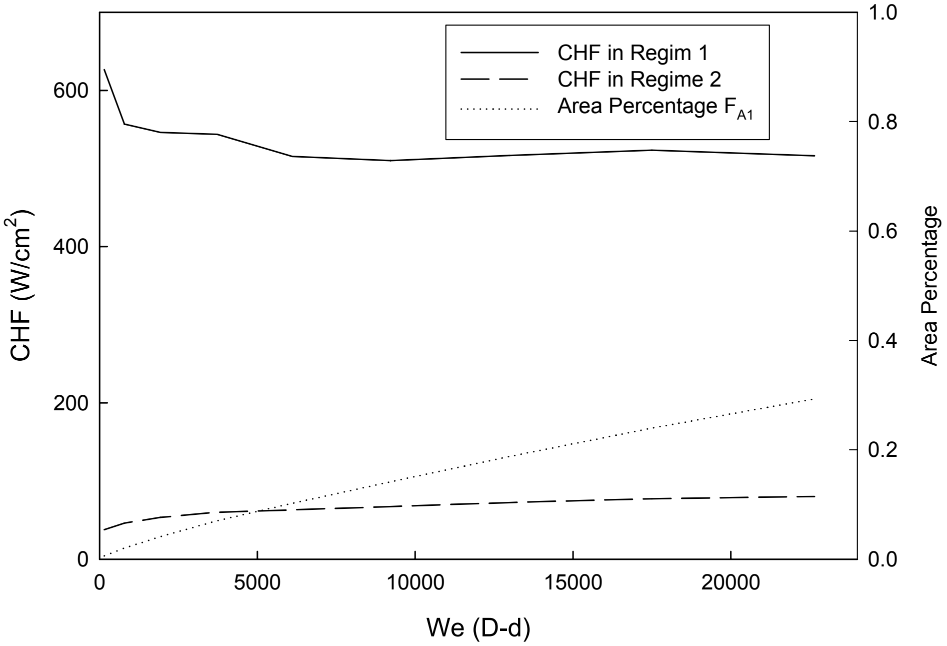

Fig. 58 Maximum heat flux and F_{A1} during single MJIC with water

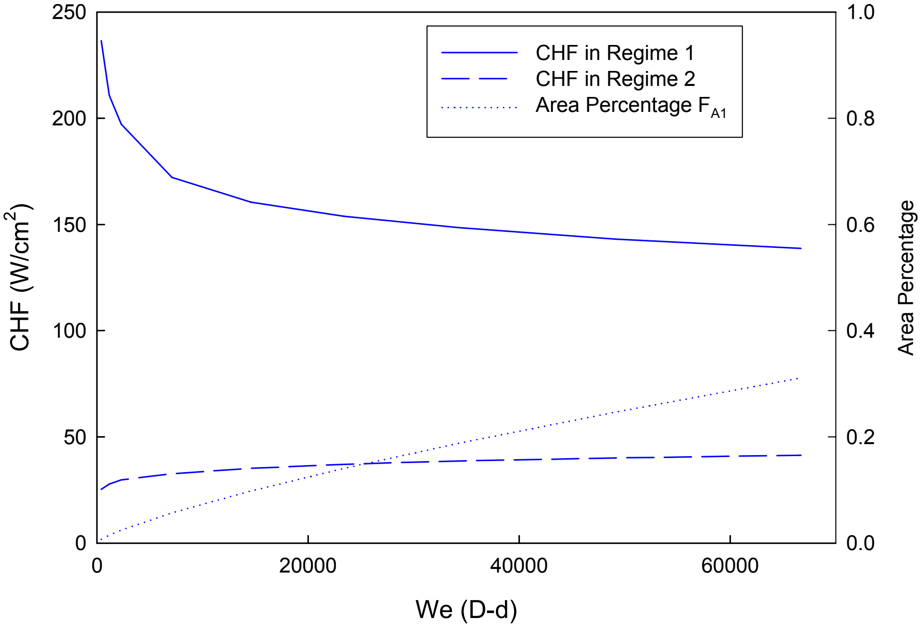

Fig. 59 Maximum heat flux and F_{A1} during single MJIC with ethanol

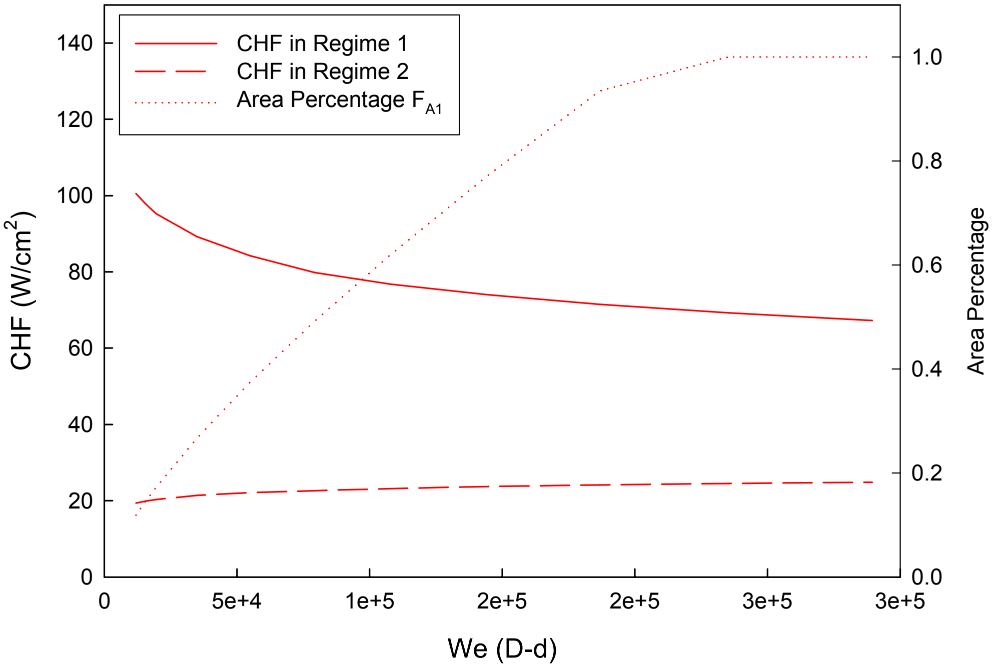

Fig. 60 Maximum heat flux and F_{A1} during single MJIC with HFE7000

8.5 Data Analysis with the new CHF correlation

Using the area ratio and maximum heat flux (See Table 20) into equation(17.9), it yields the CHF equation for single MJIC.

$$\Phi = F_{A1} \cdot 0.1556 \cdot \gamma^{1/2} \cdot \mathrm{Re}_d^{1/4} \cdot We_d^{-3/4} + \left(1 - F_{A1}\right) \cdot 0.691 \cdot \gamma^{0.466} \cdot We_{D-d}^{-0.421} \cdot \left(\frac{d}{D+d}\right)^{0.303} \tag{17.44}$$

The equation above shows the CHF consist two parts. One is contributed by the energy transfer in regime 1. The other is from regime 2. In order to demonstrate the heat contribution from each regime, the heat transportation ($q_{\max,i} = A_i \cdot q''_{CHF,i}$) in regime 1 and 2 are shown in Fig. 61, Fig. 63 and Fig. 65. The new CHF correlation would be compared with other CHF correlations again. (See Fig. 62, Fig. 64 and Fig. 66) For each type of fluid, there are two figures, one for energy contribution from each regime, and the other for comparison of CHF correlations. From those figures, we observe following:

At small We number, most of heat transfer comes from regime 2, and its absolute value slightly increase with the We number. On the other hand, the cooling effect of regime 1 starts with zero percentage at small We number or velocity, and increasing with We number. The reason is that F_{A1} (See Fig. 58) increases with increasing flowrate. As to the water, (See Fig. 61) regime 1 would contribute about 70% of cooling effect at $We_{D\text{-}d}$ = 22000. Combination of the heat transportation from two regimes yields the successful prediction for experimental results. Our CHF curve falls in the error bar of most experiment data, except for two spots with the lowest flowrate.

As to ethanol, heat transfer contribution is very similar with that of water (See Fig. 63). The heat transfer from regime 1 reaches about 60% at $We_{D\text{-}d}$ = 66000. Comparing with other correlation, the total CHF of ethanol are predicted with the best quality by our new correlation. In Fig. 64, most new predictions are close to the mid value of testing data.

In case of HFE7000, Fig. 65 shows that major heat contribution also comes from the regime 1. But its value is over-predicted comparing with the experimental results. However, the new CHF model shows a potential explanation to the unique trend of CHF curve of HFE7000. Experimental CHF of HFE7000 reaches its maximum at $We = 5\cdot10^4$, and it is predicted that there is a peak on the CHF curve by our correlation. This phenomenon has not been counted in existing CHF correlations, which only indicate that CHF simply increase with flowrate or We number. Studying our new model, it is found that the maximum heat flux from regime 1 is decreasing as in creasing the flowrate. (See Fig. 60) That means, after the regime 1 occupying the whole surface, the CHF should decrease with increasing flowrate. Though the new CHF model could not quantitatively predict the CHF of HFE7000, it shows the potential to explain the CHF trends for HFE7000.

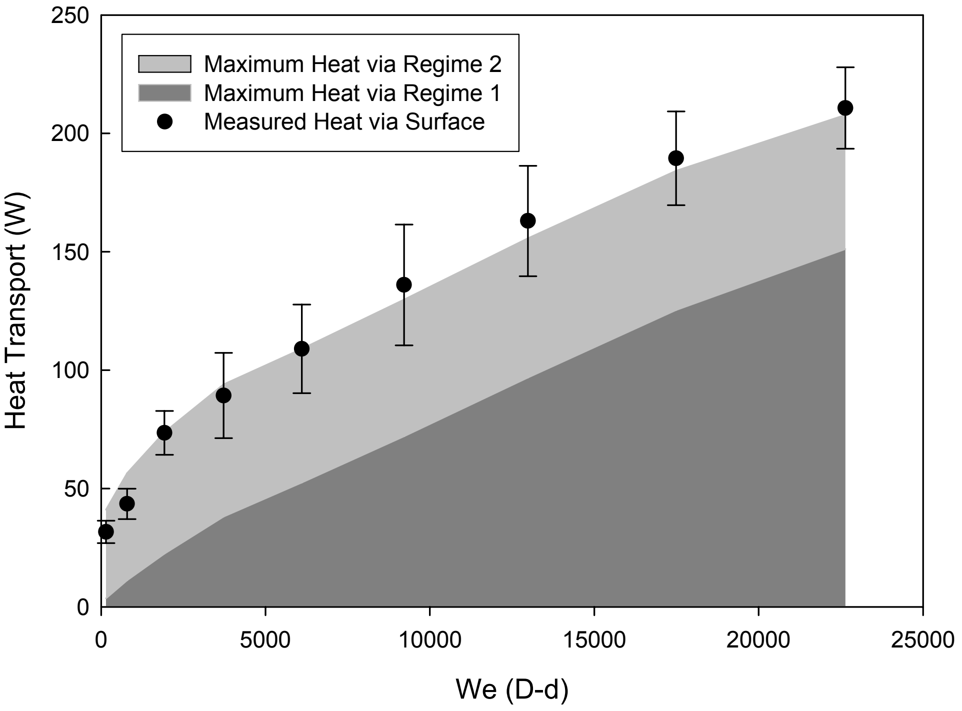

Fig. 61 Comparison of heat contribution from each region during MJIC with water

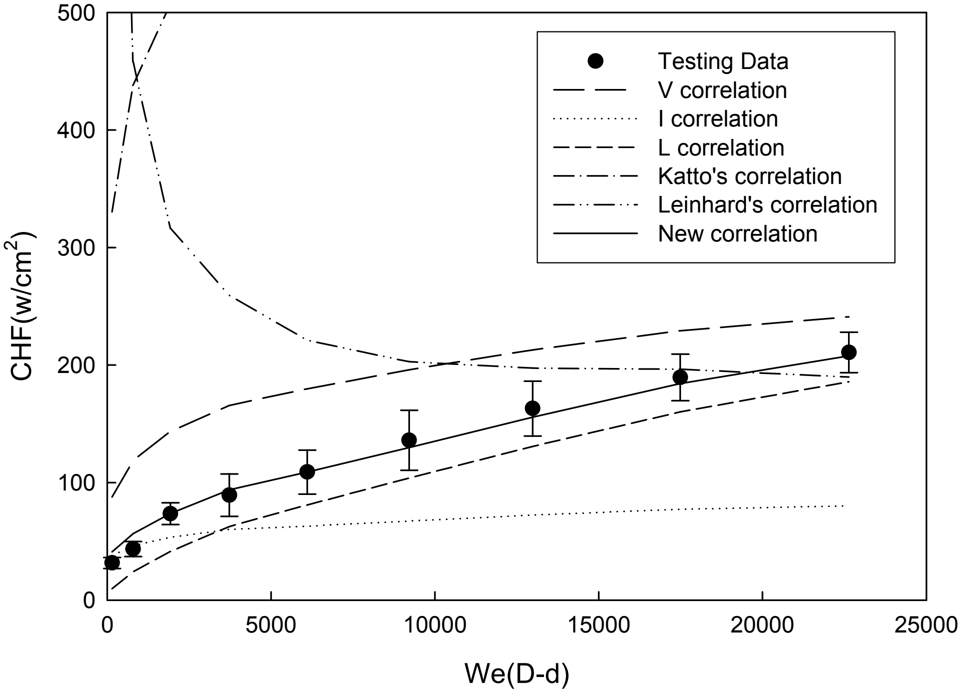

Fig. 62 Comparison of our correlation with testing data during MJIC with water

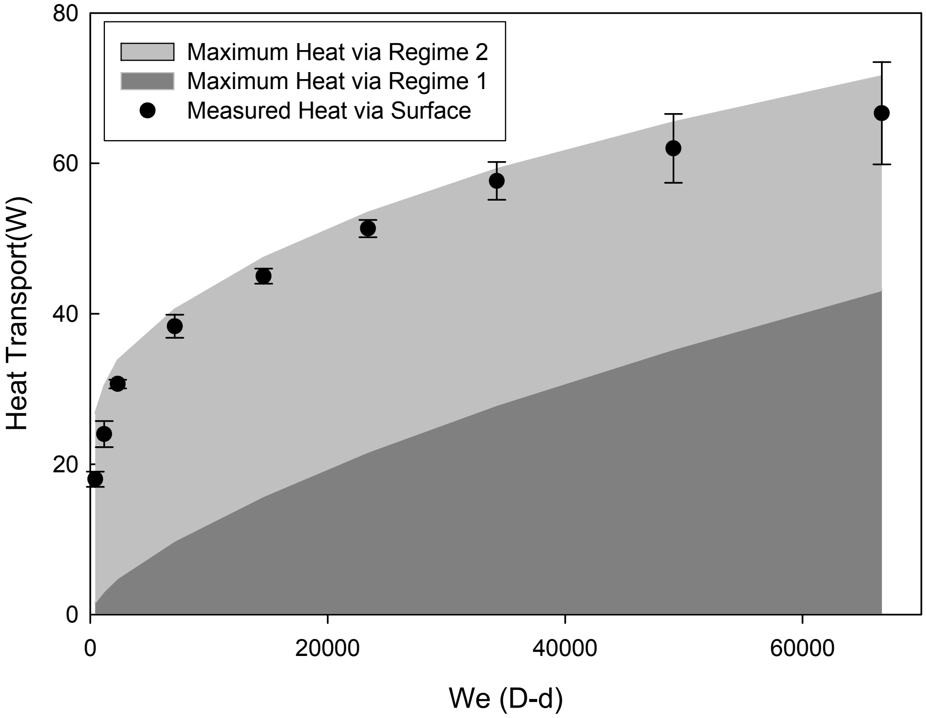

Fig. 63 Comparison of heat contribution from each region during MJIC with ethanol

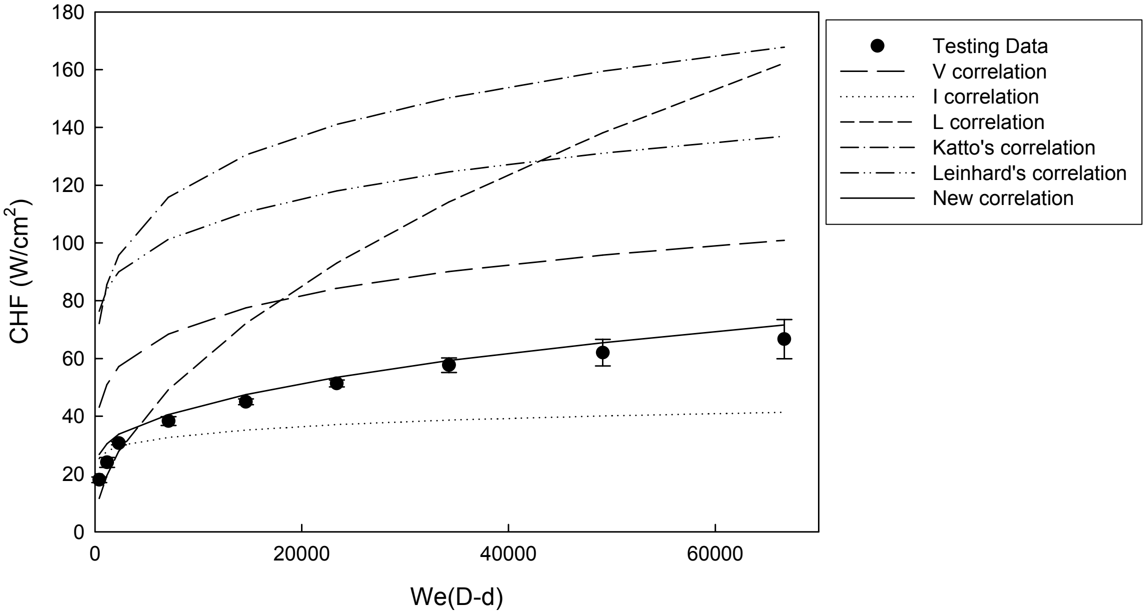

Fig. 64 Comparison of our correlation with testing data during MJIC with ethanol

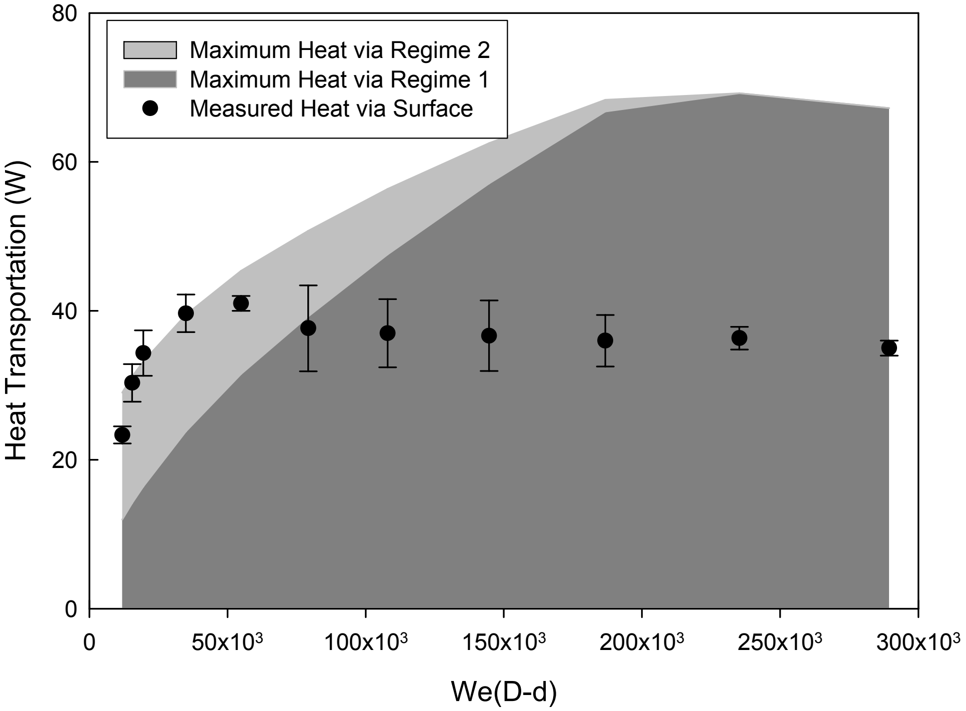

Fig. 65 Comparison of heat contribution from each region during MJIC with HFE7000

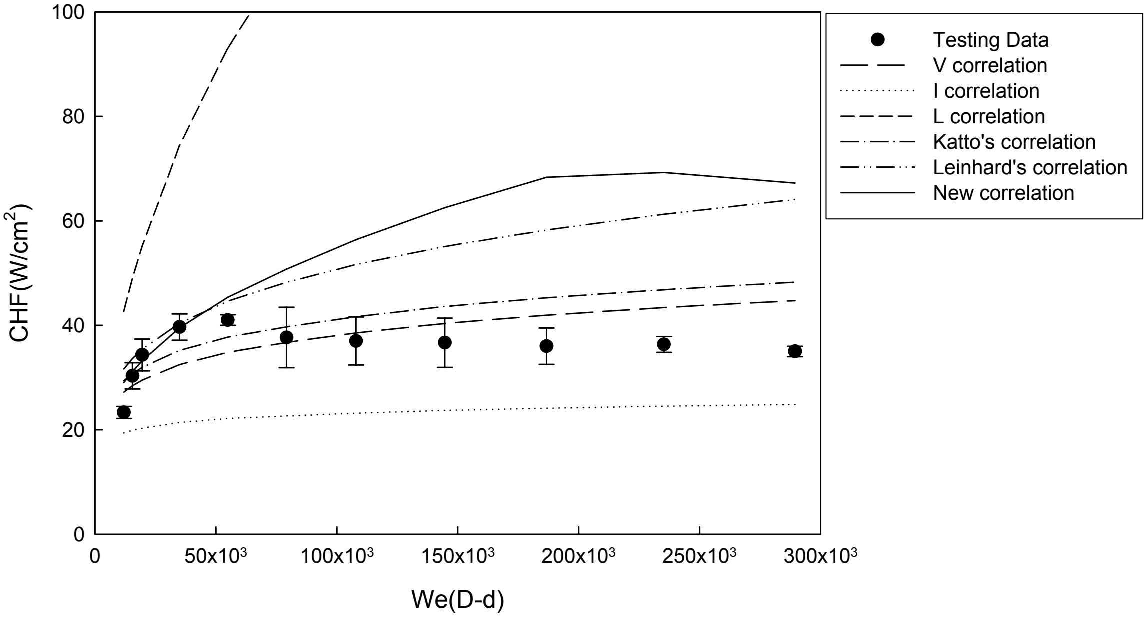

Fig. 66 Comparison of our correlation with testing data during MJIC with HFE7000

As to the deviation between the experimental result and CHF prediction for HFE7000, the reason might be that the vapor bubbles in regime 1 might not be able to penetrate the wall jet during high Re number condition, and they might float to downstream within the wall jet. That would generate high instability and disturb the velocity profile of the wall sheet. When the heat flux reaches a critical level, the vapor blanket would form under the wall jet, which causes the liquid/vapor separation. In other words, the current CHF correlation need further work to incorporate that mechanism. From the image of burnout process, (See Fig. 67) the regime 2 of ethanol shrinks inwards due to dryout at the rim. In case of HFE7000, the liquid in regime 2 is lifted by vapor and finally cause the liquid-surface separation.

Ethanol , $Q = 6.34 \cdot 10^{-7} m^3/s$, $U_e = 12.9$ m/s, $Re_d = 3034$, $We_d = 776$, $q'' = 57$ W/cm^2

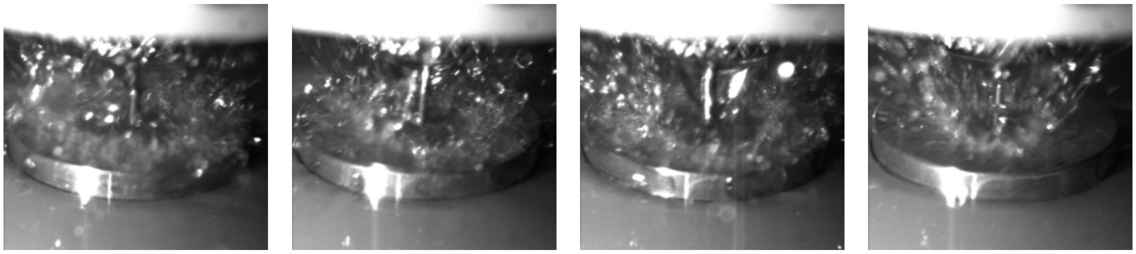

t =0 t = 2 s t = 4 s t = 6 s

HFE7000 $Q = 6.5 \cdot 10^{-7} m^3/s$, $U_e = 13.2$ m/s, $Re_d = 10497$, $We_d = 2446$, $q'' = 38$ W/cm^2

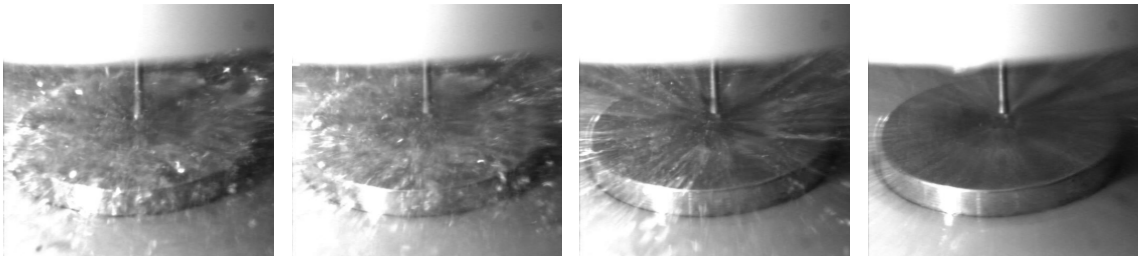

t = 0 t = 2 s t = 3 s t = 4 s

Fig. 67 Comparison of our correlation with testing data during MJIC with HFE7000

8.6 CHF Prediction Processes

The new CHF correlation is developed on experimental results and analytical works. It is easily found that the operation parameters and measurement data help to reach higher accuracy with water and ethanol. In case of utilizing the CHF correlation before testing, the operation parameters are usually known before testing, such as impinging velocity and jet diameter. But people might not know the fluid properties, which are determined by the average temperature of wall temperature and liquid incoming temperature. From the section 8.2.2, it is already proved that the fluid properties would be various during different testing conditions. It is important to estimate fluid properties in advance.

The wall temperature could be linked with wall super heat by the equation as following:

$$T_{w\sup} = T_w - T_{le} \tag{17.45}$$

Based on the experimental data, the wall super heat at CHF condition is strongly related with the heat flux and impinging velocity, which could be expressed as:

$$T_{w\sup} = C1 \cdot \left(q''_{CHF}\right)^{C2} \cdot \left(U_e\right)^{C3} \tag{17.46}$$

Those coefficients in the equation above could be determined by data regression. (See Table 21)

Table 21 Parameter estimates for T_{wsup} data regression correlation

Parameter	Estimate	Std. Error	95% Confidence Interval	
			Lower Bound	Upper Bound
C_1	1.900	.224	1.458	2.343
C_2	.797	.030	.738	.856
C_3	-.300	.025	-.350	-.250

Dependent variable: T_{wsup} (°C): R squared = .813

Therefore the T_{wsup} could be forecasted by using following equation:

$$T_{w\sup} = 1.90 \cdot \left(q''_{CHF}\right)^{0.797} \cdot \left(U_e\right)^{-0.300} \tag{17.47}$$

The equation above (17.48) is coupled with the equation (17.49), so the CHF value would be estimated by iterations. First, using the initial conditions to estimate the CHF by equation (17.50). After getting CHF value, the wall temperature could be calculated by equation (17.51) and (17.52). Then the fluid properties need to be updated based on the fluid temperature (See section 8.2.2), and error of fluid temperature could be calculated. The iterations continue until the error is substantially small.

8.7 Effect of Subcooling on CHF of single MJIC

A set of comparison experiments is carried out in order to study the effect of subcooling during single MJIC. Experiments are done in two kind of condition with ethanol. One is in saturated condition, in which T_{sat} = 22 °C and T_{sub} = 2 °C. The other is in 1 ATM, in which T_{sat} = 78 °C and T_{sub} = 55 °C. The effect of subcooling with is shown in Fig. 68.

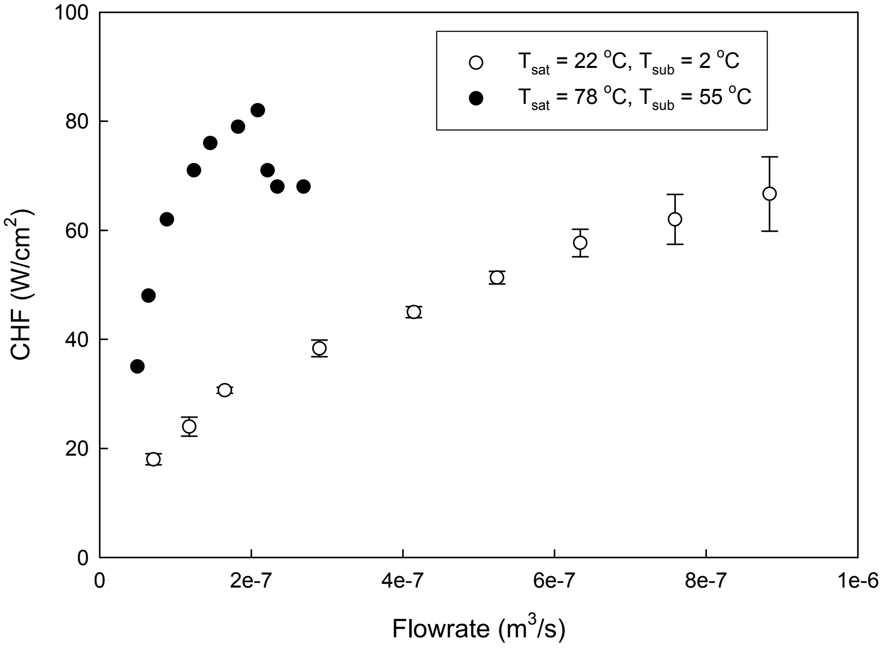

Fig. 68 Effect of subcooling in sing and multi MJIC with ethanol

Some other researchers had studied the effect of subcooling on the CHF. For example, M. Monde had used the following equation to calculate the CHF with high subcooling [70].

$$q''_{CHF} = q''_m \left(1 + 2.7 \cdot \left(\frac{\rho_l}{\rho_v} \right)^{0.5} \left(\frac{Cp_l \Delta T_{sub}}{h_{fg}} \right)^2 \right) \tag{17.53}$$

Substituting parameters of our tests in the above equation, it is found that the equation indicates that the CHF would increase 113% by the effect of subcooling term. This is consistent with the experimental data.

One interesting phenomenon we found is that, there is a peak on the CHF curve with subcooled ethanol. The CHF reach the maximum value at flowrate equals to $2.9 \cdot 10^{-7}$ m^3/s. This phenomenon is similar with the CHF curve of HFE7000 at saturated condition. It is considered due to the same reason. With deep subcooling effect, the wall jet would push the boundary of regime 1 outwards. That means, the deep subcooling would benefit the process of region 1 occupying the whole surface. Therefore, this phenomenon that does not occur in the saturated condition would appear in the deep subcooling condition.

8.8 Single MJIC summary

In this chapter, the high speed images and classical wall jet analysis show that the wall jet could be divided into two regimes. The unique features of single MJIC, is illustrated from two aspects: One is the surface is covered by thin film wall jet beyond BL region. The other is vapor density plays a big role in saturated working condition. Then a thermal bridge sketch was analyzed to show the heat transfer around the heater. It is proposed that the general CHF of the whole surface is equal to the area average of the maximum heat flux in each area. According to that hypnosis, a semi theoretical CHF model is developed based on force balance inside the wall jet. The results show that predictive CHFs by our model match with the experimental results, especially for tests with water and ethanol. Though it could not predict the CHF of HFE7000 precisely, the new CHF model shows this potential to explain the unique trend of CHF curve of HFE7000, which could not be explained by other existing CHF correlations. Similar phenomenon also is observed in single MJIC with subcooled ethanol. It is suspected that two phenomena are resulted from the same factor, which needs to be taken into account to the CHF model in the future works.

CHAPTER 9. MULTI MICRO JETS IMPINGEMENT COOLING

After investigating the single MJIC, we are curious about the impingement cooling by multi micro jets. First, experiments of multi MJIC would be conducted with three types of nozzles and three fluids. Then, the experimental CHF results would be compared with three types of CHF correlations for multi MJIC.

1. The existing CHF correlation for multi jet impingement cooling, which proposed by M. Monde, is very similar to his V-correlation for single jet impingement cooling.
2. Base on the formula of existing CHF correlations and the semi-theoretical CHF correlation for single MJIC, a CHF correlation for MJIC could be generated simply by experimental results regression.
3. Since a semi-theoretical CHF correlation has been developed for single MJIC, a correlation for multi MJIC could be obtained by treating each jet as a single MJIC.

Second, the heat transfer effect by using multi jet nozzle would be investigated by three kinds of fluid and three types of nozzle. The potential capability to enhance CHF and heat transfer coefficient by multi MJIC would be shown in form of boiling curve.

9.1 Experimental Results of Multi MJIC

Three types of nozzle are manufactured in order to compare the effect of multi MJIC. They are 1 jet, 4 jets and 9 jets, and their configurations are shown in Fig. 41.

Experimental results are shown in form of Re_d versus CHF. (See Fig. 70). We observe following:

1. At same Re number, multi MJIC could improve the CHF with water and ethanol. As to HFE7000, it is depends on testing condition. Under certain condition, that effect is negligible or even might be negative.
2. At same flowrate, the heat transfer enhancement depends on fluids. In case of water, multi MJIC could not enhance its CHF because the boiling process mainly affected by the impinging momentum force, which deceases with jet number. CHF of ethanol mainly influenced by flowrate, instead of jet number. As to HFE7000, 4 jet nozzle could reach a higher CHF than single jet nozzle when Q > $7 \cdot 10^{-7}$ m^3/s, and 9 jet nozzle is still the worst one.

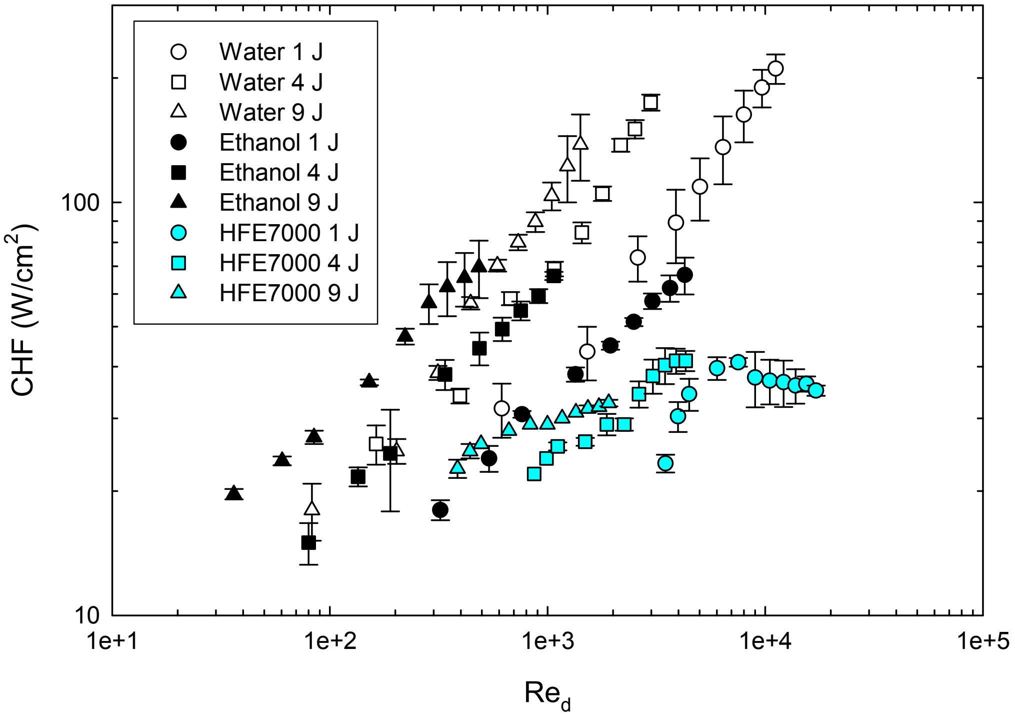

Fig. 69 CHF enhancement by multi MJIC (Re vs CHF)

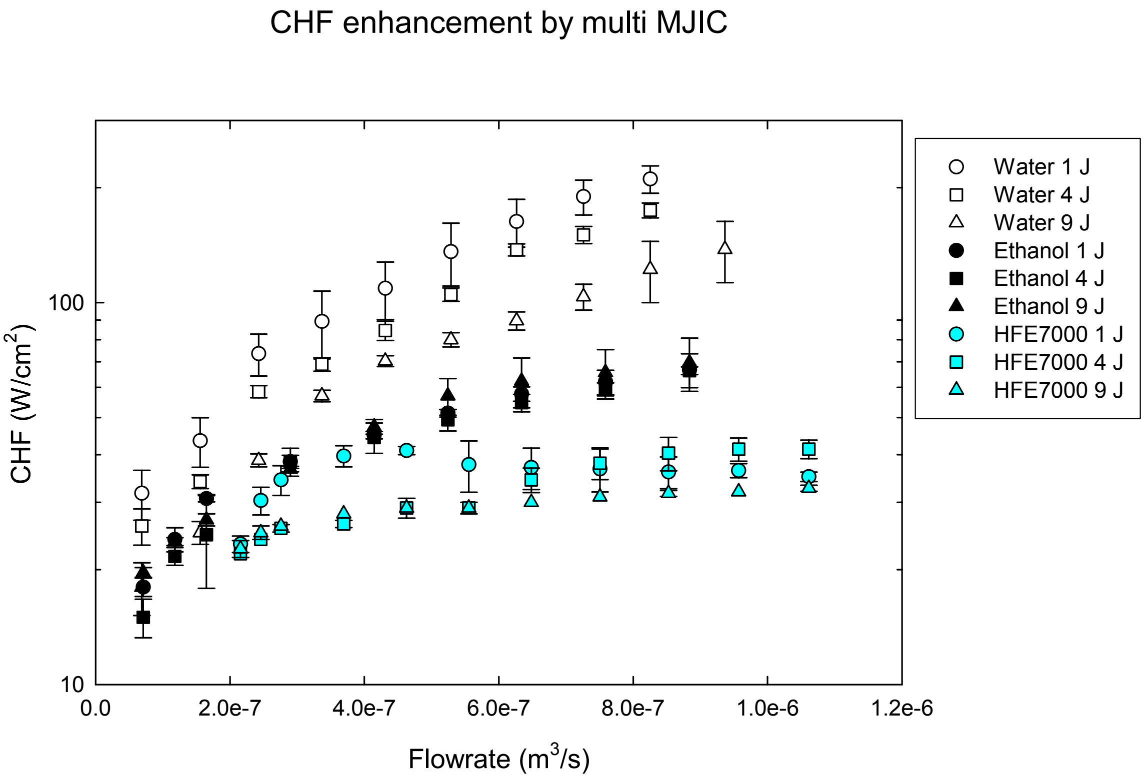

Fig. 70 CHF enhancement by multi MJIC (Q vs CHF)

The high speed images in Fig. 71, show that the heating surface is dominated by nucleate boiling during multi MJIC. Compare with single MJIC, there is more extra liquid staying on the surface, especially with low flowrate. At same existing velocity, more convective boiling is found by using 9 jet nozzle. At same flowrate, due to less liquid momentum force, the edge of heating surface might not be wetted at CHF condition. On the hand, by increasing the flowrate, the surface could be fully wetted and convective boiling would take over nucleate boiling in some area. It is obviously that 4 convective boiling sites are generated by impinging jets.

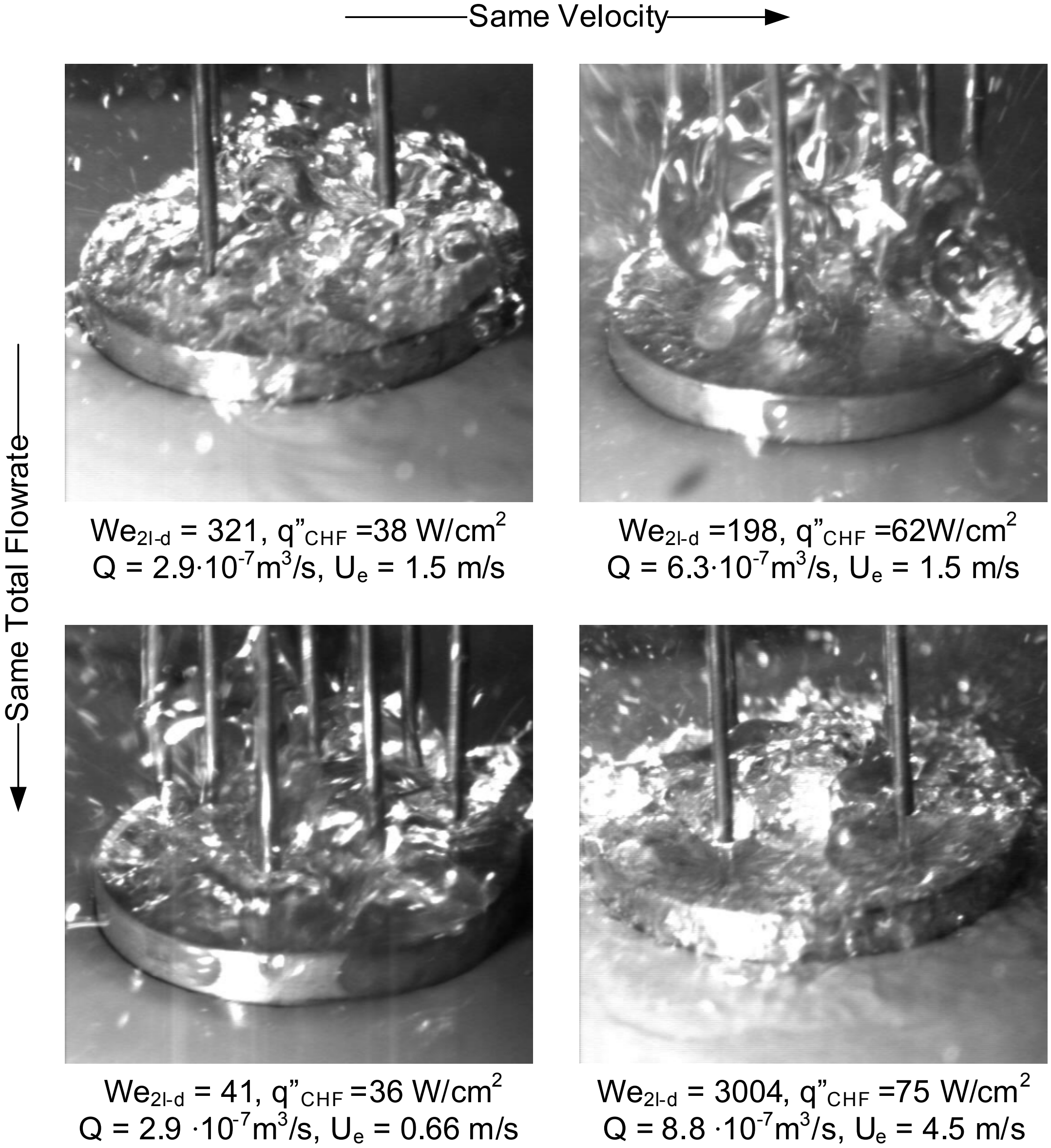

$We_{2l\text{-}d} = 321$, $q''_{CHF} = 38\ W/cm^2$
$Q = 2.9 \cdot 10^{-7} m^3/s$, $U_e = 1.5\ m/s$

$We_{2l\text{-}d} = 198$, $q''_{CHF} = 62 W/cm^2$
$Q = 6.3 \cdot 10^{-7} m^3/s$, $U_e = 1.5\ m/s$

$We_{2l\text{-}d} = 41$, $q''_{CHF} = 36\ W/cm^2$
$Q = 2.9 \cdot 10^{-7} m^3/s$, $U_e = 0.66\ m/s$

$We_{2l\text{-}d} = 3004$, $q''_{CHF} = 75\ W/cm^2$
$Q = 8.8 \cdot 10^{-7} m^3/s$, $U_e = 4.5\ m/s$

Fig. 71 Photos of ethanol during multi MCJIC at CHF condition

9.2 CHF Correlations for Multi MJIC

9.2.1 Monde's CHF correlation for multi jets impingement cooling

By reviewing past work, it is found that only a few studies had been carried out on multi free boundary jets impingement cooling. The only CHF correlation for multi jet impingement cooling was proposed by Monde. According to his experimental results, it was able to predict CHF in multi jet impingement cooling by slightly modifying the We number in the V-correlation for single jet impingement cooling. That is to change the characteristic length of We number to the maximum distance from the jet position to the point in the domain controlled by the jet. In Fig. 72, the relative locations of the jets on the disk heater are plotted, including D, d and L.

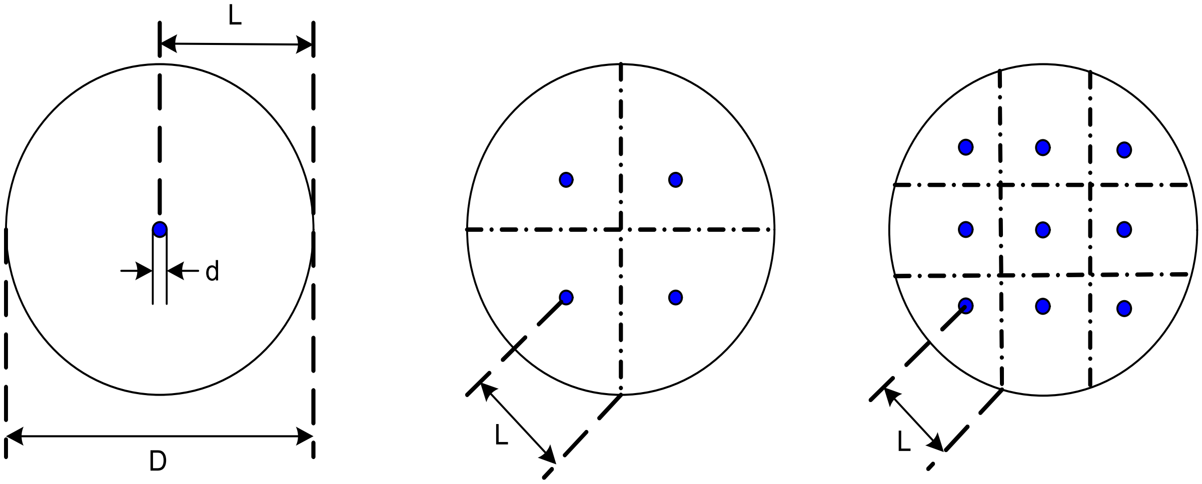

Fig. 72 Characteristic length of multi jet impingement cooling

Monde's correlation for multi jet impingement cooling could be expressed as following:

$$\Phi_{vm} = 0.221 \cdot \gamma^{0.645} \cdot We_{2L-d}^{-0.343} \cdot \left(\frac{d}{2L+d} \right)^{0.364} \tag{18.1}$$

In this study, we plan to compare the prediction by this CHF correlation with experimental results.

9.2.2 A CHF correlation by data regression

By select the right form of CHF correlation, we could develop a correlation from the experimental data. In the present study, we have not study the effect of surface size and jet diameter. So we do not plan to introduce the geometry factor into the CHF correlation. Based on our analysis on single jet impingement cooling, we consider that the CHF should relate with Re, We and γ. The form of CHF correlation we proposed is expressed as following:

$$\Phi_{Rm} = C_1 \cdot \mathrm{Re}_d^{C_2} \cdot We_{2L-d}^{C_3} \cdot \gamma^{C_4} \tag{18.2}$$

Where: C_1, C_2, C_3, C_4 are coefficients that need to be determined from experimental data.

We_{2L-d} is the Webber number with the characteristic length of 2L-d

Re_d is the Reynolds number of exiting liquid jet

γ is the liquid/vapor density ratio

One thing we want to mention is that the correlation incorporates the effect of jet number into Re_d and We_{2L-d}. At same flowrate, Re and We number would decrease as increasing the jet number.

After obtaining the experimental results, we use SSPS 15 to get the coefficients by data regression. The estimated coefficients are shown in the Table 22.

Table 22 Parameter estimates for CHF data regression correlation

Parameter	Estimate	Std. Error	95% Confidence Interval	
			Lower Bound	Upper Bound
C_1	.060	.010	.039	.080
C_2	.121	.036	.050	.191
C_3	-.337	.020	-.377	-.296
C_4	.500	.014	.471	.528

Dependent variable: CHF (W/cm^2): R squared = .870

Thus we get the CHF correlation for multi micro jets impingement cooling.

$$\Phi_{Rm} = 0.06 \cdot \mathrm{Re}_d^{0.121} \cdot We_{2L-d}^{-0.337} \cdot \gamma^{0.5} \tag{18.3}$$

9.2.3 A semi-theoretical CHF correlation for multi MJIC

Since we proposed a CHF model for single MJIC, a similar CHF model could be developed for multi MJIC. Each jet in multi MJIC might be treated as a single MJIC, it is suspected that each jet would have its own dominant zone. which also composed by three parts, F_{A1}, Φ_{CHF1} and Φ_{CHF2}. As to multi MJIC, CHF in each zone is same and could be treated the CHF of single MJIC. In other words, it could be divided into regime 1 and regime 2 in each zone, and the maximum heat flux in regime 1 and regime 2 could be calculated by using the same method for single MJIC. The area percentage of regime 1 could be determined by the incoming liquid jet. In this study, we make an approximation in order to simplify the problem. We assume that the total R_{A1} is the area sum of regime 1 at all impingement spots, though the area ratio, R_{A1}, during multi MJIC should be very complex in real situation. So the total R_{A1} for multi MJIC could be expressed as following:

$$A_{m1} = n \cdot \pi \cdot r_{b,mj}^2 = \frac{n \cdot \pi}{16.04} \cdot \left(We_d \cdot \mathrm{Re}_d\right)^{1/2} \cdot d^2 \qquad (18.4)$$

Therefore, the area ratio would be

$$F_{Am1} = \frac{A_{m1}}{A} = 4 \cdot n \cdot \frac{r_b^{\ 2}}{D^2} = \frac{n}{4.01} \cdot \left(We_d \cdot \mathrm{Re}_d\right)^{1/2} \cdot \left(\frac{d}{D}\right)^2 \qquad (18.5)$$

When $\frac{A_{m1}}{A} > 1$, we assume the regime 1 covers all the heating surface, which means $F_{Am1} = 1$.

In the Fig. 73-Fig. 75, the area ratios, F_{Am1}, are shown with different micro jet number and different types of fluids. At the same existing velocity or Re number, the 9 jets nozzle would generate largest size of regime 1 as it has more impingement spots than others. On the other hand, with same total flowrate, the exiting momentum would be reduced by increasing the jet number. Therefore the F_{Am1} of 9 jets are the lowest and those with 1 jet are the highest at the same flowrate.

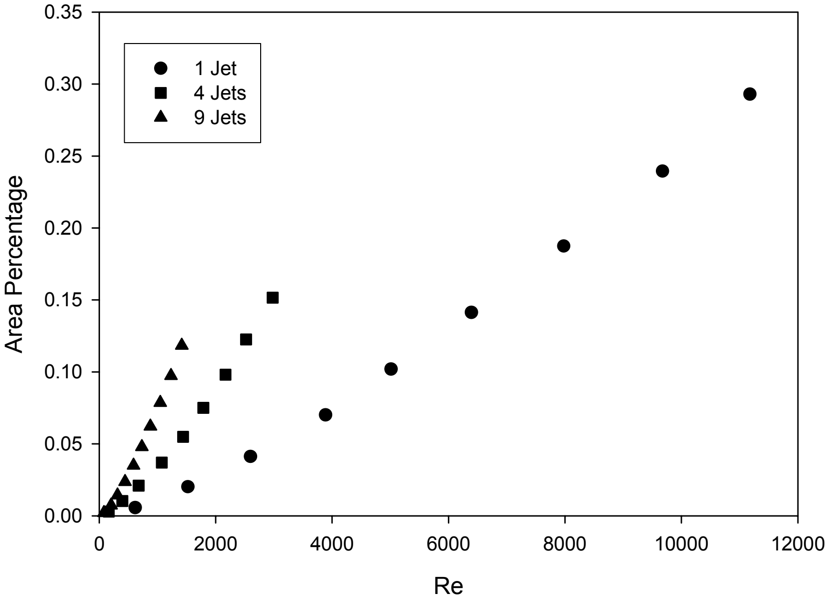

Fig. 73 Area percentage (F_{A1}) during multi MJIC with water

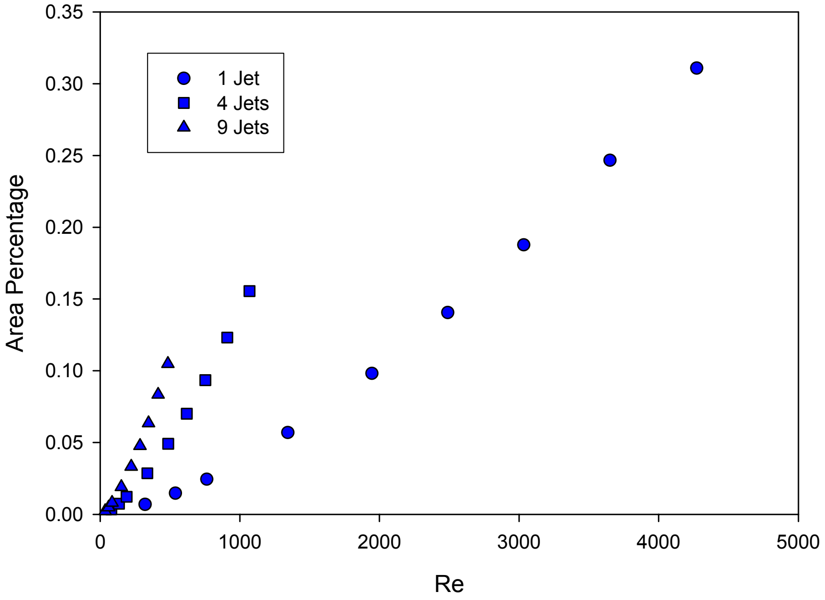

Fig. 74 Area percentage (F_{A1}) during multi MJIC with ethanol

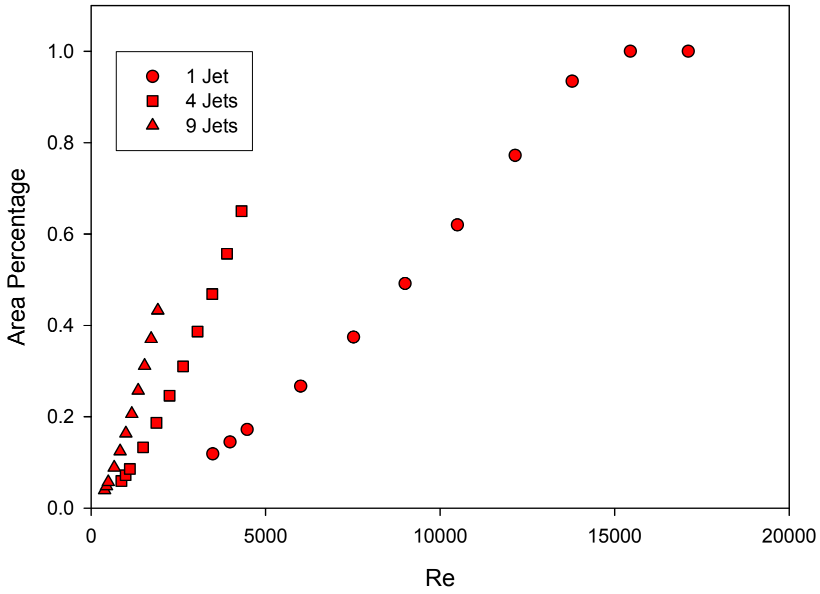

Fig. 75 Area percentage (F_{A1}) during multi MJIC with HFE7000

In case of multi MJIC, the maximum heat flux in regime 1 is considered same as that for the single jet, which could be expressed as following:

$$\Phi_{m1} = 0.173 \cdot \gamma^{1/2} \cdot \mathrm{Re}_d^{1/4} \cdot We_d^{-3/4} \tag{18.6}$$

One thing we want to point out is that the CHF in regime 1 is determined by the incoming flow, while the CHF in regime 2 need to count in the effect of surface size. For example, the We number in regime 2 uses D-d as the characteristic length for single MJIC. As to multi MJIC, the CHF in the regime 2 need to be modified to represent the effect of nozzle pattern. So we plan to adopt the method used by Monde. The characteristic length that of We number in regime 2, is 2L-d. That means the $We_{D\text{-}d}$ in single MJIC is replaced with $We_{2L\text{-}d}$ for multi MJIC.

Therefore the maximum heat flux equation for regime 2 is expressed as following:

$$\Phi_{m2} = 0.691 \cdot \gamma^{0.466} \cdot We_{2L-d}^{-0.421} \cdot \left(\frac{d}{2L+d} \right)^{0.303} \tag{18.7}$$

The final CHF equation for multi MJIC would combine the three parts, F_{AM1}, Φ_{m1} and Φ_{m2}. Combination of three parts yields the final CHF correlation as following:

$$\begin{aligned} \Phi_{mj} &= F_{Am1} \cdot 0.173 \cdot \gamma^{1/2} \cdot \mathrm{Re}_d^{1/4} \cdot We_d^{-3/4} \\ &+ \left(1 - F_{Am1}\right) \cdot 0.691 \cdot \gamma^{0.466} \cdot We_{2L-d}^{-0.421} \cdot \left(\frac{d}{2L+d} \right)^{0.303} \end{aligned} \tag{18.8}$$

9.3 CHF Data Analysis for Multi MJIC

In the previous section, we describe the three CHF equations, (18.1), (18.3) and (18.8), for multi MJIC. The comparison results of CHF correlation for multi MJIC are shown in the Fig. 76 - Fig. 78. We observe following:

1. With the same We number, the CHF of 9 jets is the highest and that of single jet is the lowest. In other words, when the system provides the same exiting velocity, or the same level of pressure head, the CHF could be enhanced by adding more impingement spots. While at the same level of total flowrate, the CHF could not get obvious enhancement and might be reduced by using multi jet nozzle, depending on the working fluid and conditions.

2. As to the CHF correlations, it is found that V-correlation and our model could not predict the results precisely. As to the multi MJIC with ethanol, the semi-theoretical CHF correlation could be valid for high flowrate condition, but not the low flowrate condition. In other conditions, most of predictions by that correlation are higher than the experimental results. Most prediction values of V-correlation

are higher or lower than the experimental results. As to the CHF data regression correlation, it is the closest one to the experimental data.

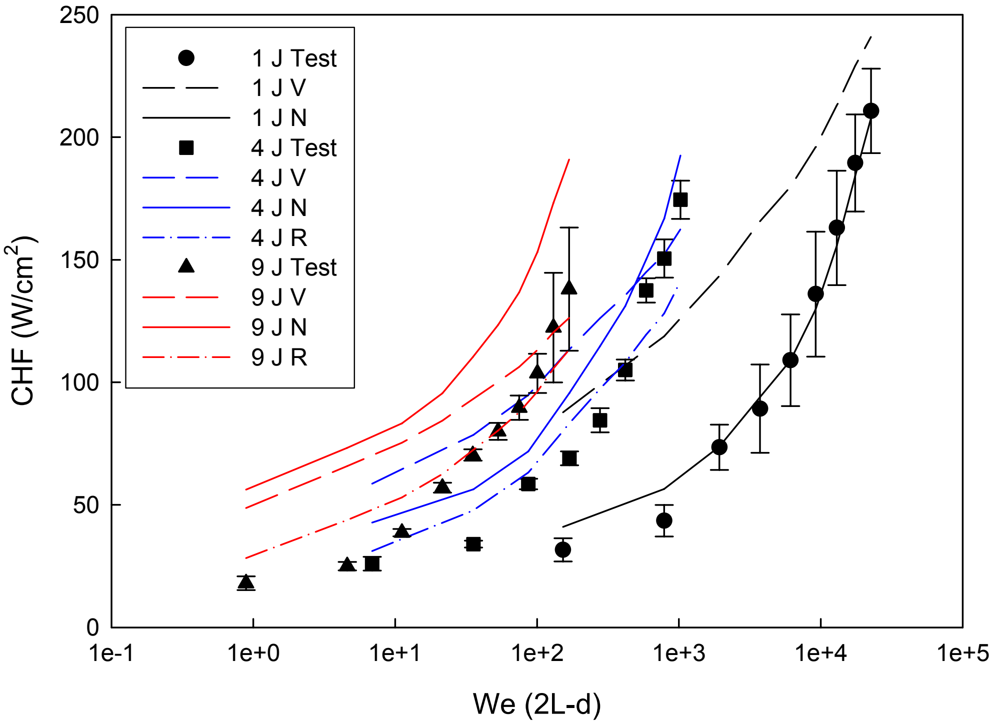

Fig. 76 Comparison of CHF Correlations for multi MJIC with water

Note: 1 J: single jet impinging, 4 J: 4 jets impinging, 9 J : 9 jets impinging
V: CHF V-correlation by Monde,
N: the semi-theoretical CHF correlation by force analysis,
R: experimental CHF correlation by data regression

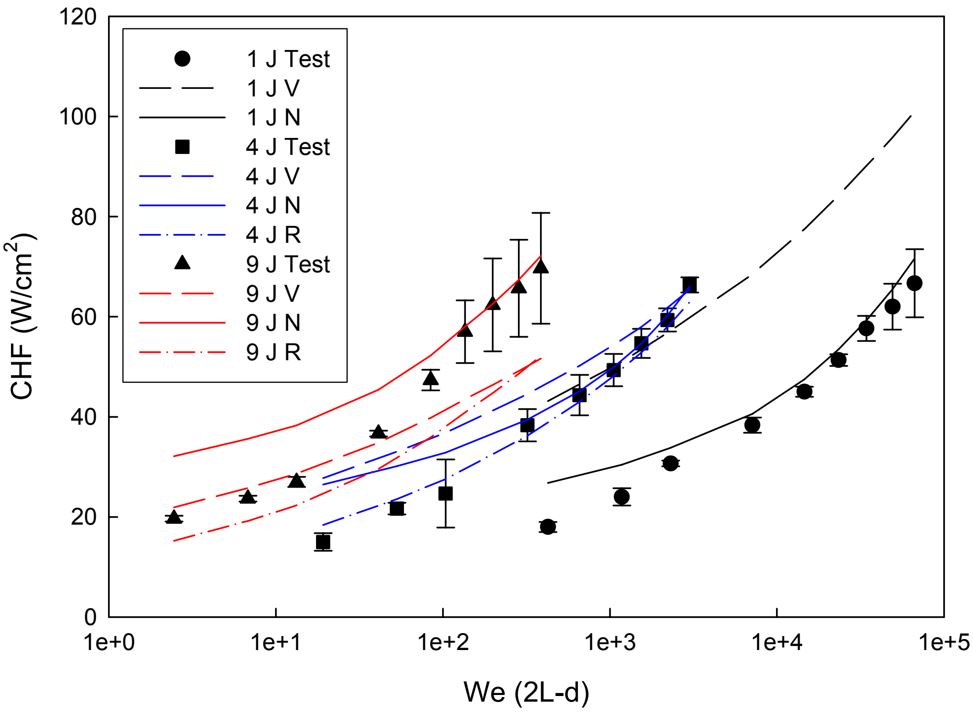

Fig. 77 Comparison of CHF Correlations for multi MJIC with ethanol

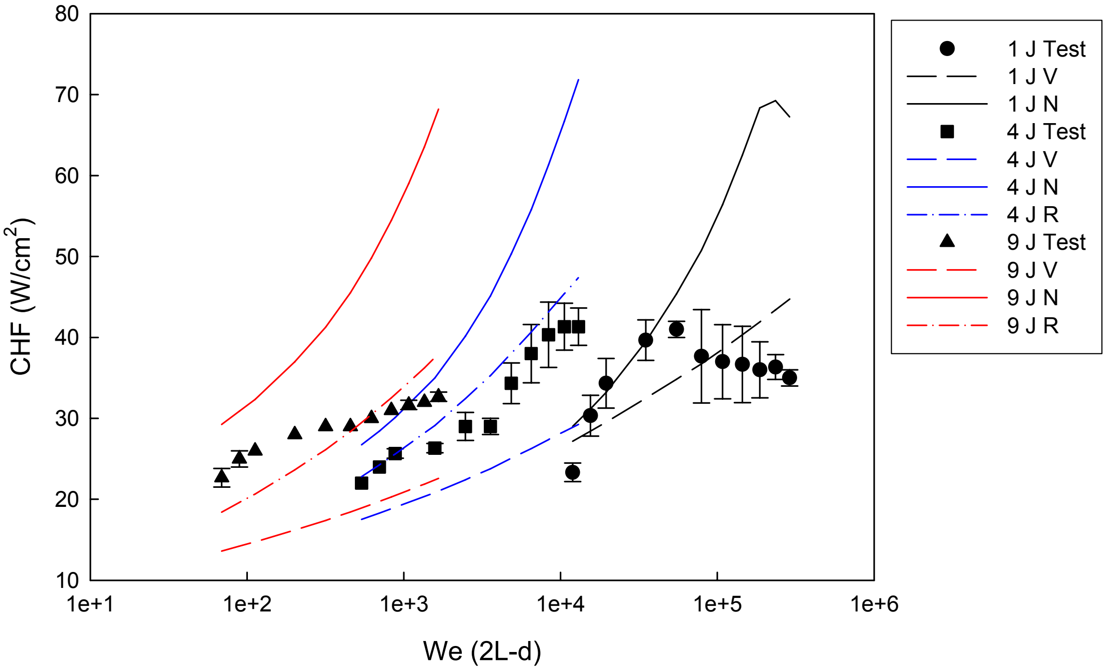

Fig. 78 Comparison of CHF Correlations for multi MJIC with HFE7000

Note: 1 J: single jet impinging, 4 J: 4 jets impinging, 9 J : 9 jets impinging
V: CHF V-correlation by Monde,
N: the semi-theoretical CHF correlation by force analysis,
R: experimental CHF correlation by data regression

Discussion about CHF prediction for multi MJIC:

1. Monde's L correlation had been verified by his experiments. But the size of jet is 8 times larger than what we tested in this study. And his verification experiment was contacted with the nozzles, which only had a maximum jet number of 4. Our tested jet number could be much larger. Those two issues might cause the V-correlation invalid for our experiments.
2. As to the semi-theoretical CHF correlation, we put several assumptions that might not be true in multi MJIC.
    a. First, the simplification about wall jet thickness is only valid for high impingement momentum. Since the jet number reduced the exiting velocity, it could not be valid for the small flow rate conditions during multi MJIC.
    b. Second, during multi MJIC, the interaction of the wall jets and vapor bubbles should be significant strong. In that situation, each liquid jet might not have a clear dominant zone, especially at low flowrate. At flowrate, we had observed the dominant zone of each jet, but the boundary between each zone was quite wide. That effect has not been taken into account.
3. The phase-change process in multi MJIC is so complex that those coupled effects are difficult to embed into a simple model. So far it is the best choice to use the data regression correlation which has relative high accuracy.

Discussion about CHF experiments during multi MJIC:

1. First, the multi MJIC cause more debris deposition spots on the testing surface. The experiments of multi MJIC would receive more uncertainty from the factor of surface properties.
2. Second, the exiting velocity of each liquid jet might be different. As to the 9 jet nozzle, there could be a problem to distribute the flow uniformly. Due to the geometry of the 9 jet nozzle pocket, the center jet should have more kinetic pressure head and the jets at the corner would have less pressure head due to the drag force. Therefore the nozzle geometry could cause the non uniform distribution of impingement mass, which finally affect the phase-change process on the heating surface.

9.4 Heat Transfer Enhancement by Multi MJIC

Besides CHF, heat transfer coefficient is another important parameter, which had great value to study during the MJIC. A lot of works on jet impingement cooling had shown this coefficient in form of the boiling curves. In order to compare the effect of nozzle type on heat transfer coefficient, we will show the boiling curve of single and multi MJIC together. (See Fig. 79-Fig. 81) The boiling curves of different fluids are shown in two ways with same type of fluid. One plot shows the boiling curves with the same exiting velocity $U_e = 1.5$ m/s. In case of tests with same fluid, that means the same Re number or the same pressure head that pump could provide. The other type plot shows the boiling curve in at the same total flowrate $Q = 2.9 \cdot 10^{-7}$ m^3/s.

We observe following:

1. For water jet impingement, severe fluctuation was found in surface temperature measurement when the fully nucleate boiling (FNB) was reached. The amplitude of those fluctuating was as large as 20 °C, which mainly due to the changing of surface properties. (See section 6.2) The fluctuating becomes weak when the heat fluxes approaching CHF. The similar situation also happened with other fluids, but the amplitude of fluctuation is not as large as that with water.

2. At same exiting velocity, the 9 jet nozzle could get the lowest wall super heat with water. That means, the heat transfer coefficient is highest with 9 jets nozzle, and the single jet and 4 jet nozzles are lower. At same total flowrate, the 1 jet nozzle reaches the highest heat transfer coefficient, while 9 jets nozzle gets the lowest one. No matter at the same level of velocity or total flowrate number, the 4 jet nozzle achieves the highest CHF with water.

3. As to the boiling curve of ethanol, the flowrate is the dominating factor. At same exiting velocity, which means the 9 jet nozzle has highest heat transfer coefficient and CHF, while the single jet nozzle has the worst performance in both aspects. At the same flowrate, 3 types of nozzle get the same level of CHF, and the heat transfer coefficients are also very close.

4. The testing condition of HFE7000 could not be obtained with U_e = 1.5 m/s with 1 J nozzle, which lower than the working range of the flowmeter. So the test results of HFE7000 only are presented with same flowrate. It is found that the boiling curve has similar trend of ethanol. At the same flowrate, both CHF and heat transfer coefficient could not be change too much by nozzle type. Only 1 jet has a little

higher CHF and 9J has a little bit lower heat transfer coefficient than other test conditions.

General speaking, at the same level of flowrate Q = 18 mL/min, the heat transfer coefficient of water would be reduced by the jet number. At the same velocity, heat transfer coefficient could be enhanced by multi micro jet nozzle. As to HFE7000 and ethanol, flowrate shows the most importance on heat transfer coefficient, which is different with water.

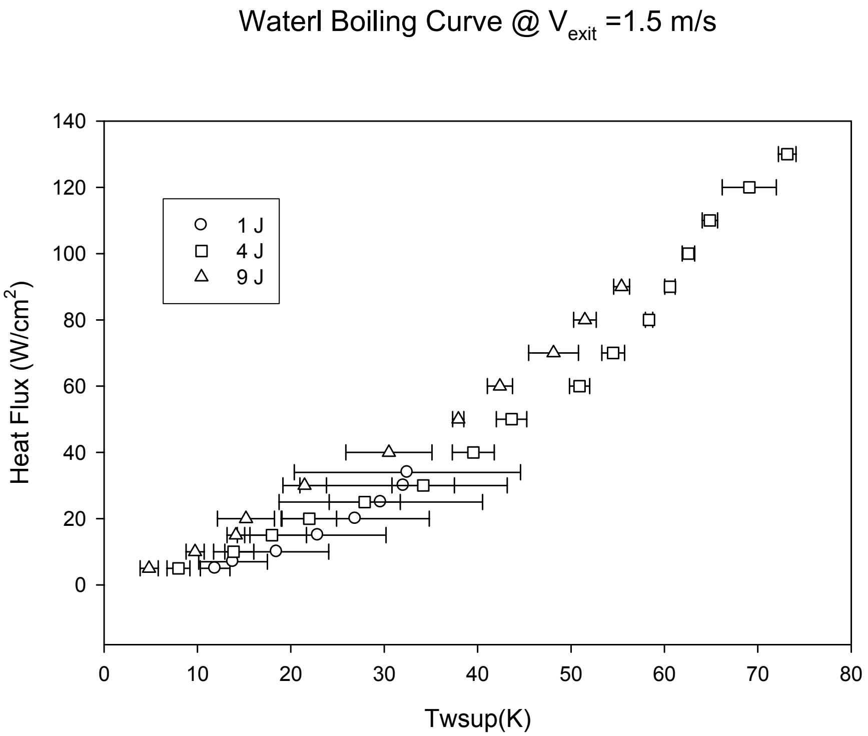

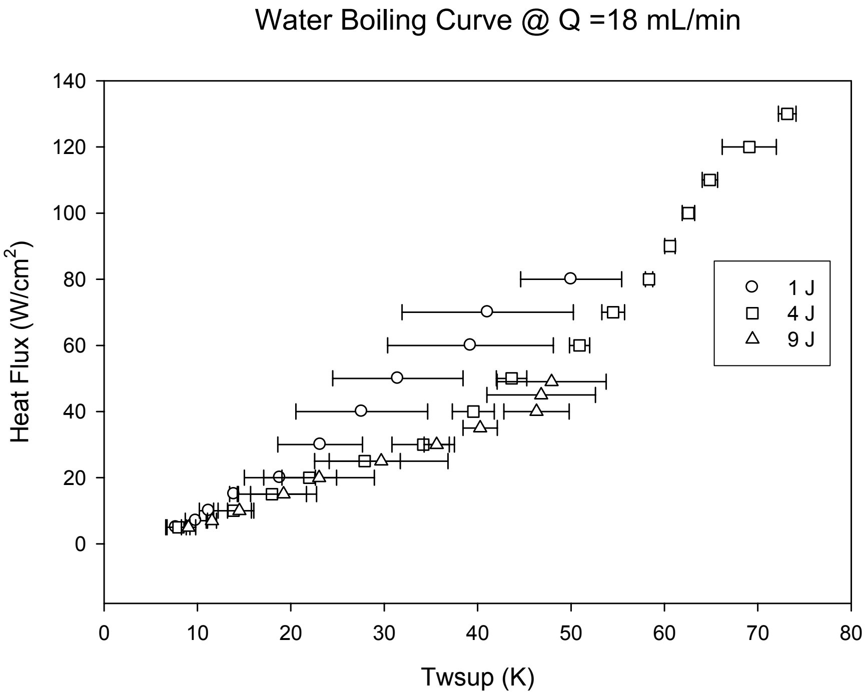

Fig. 79 Effect of jet number on boiling curves of water

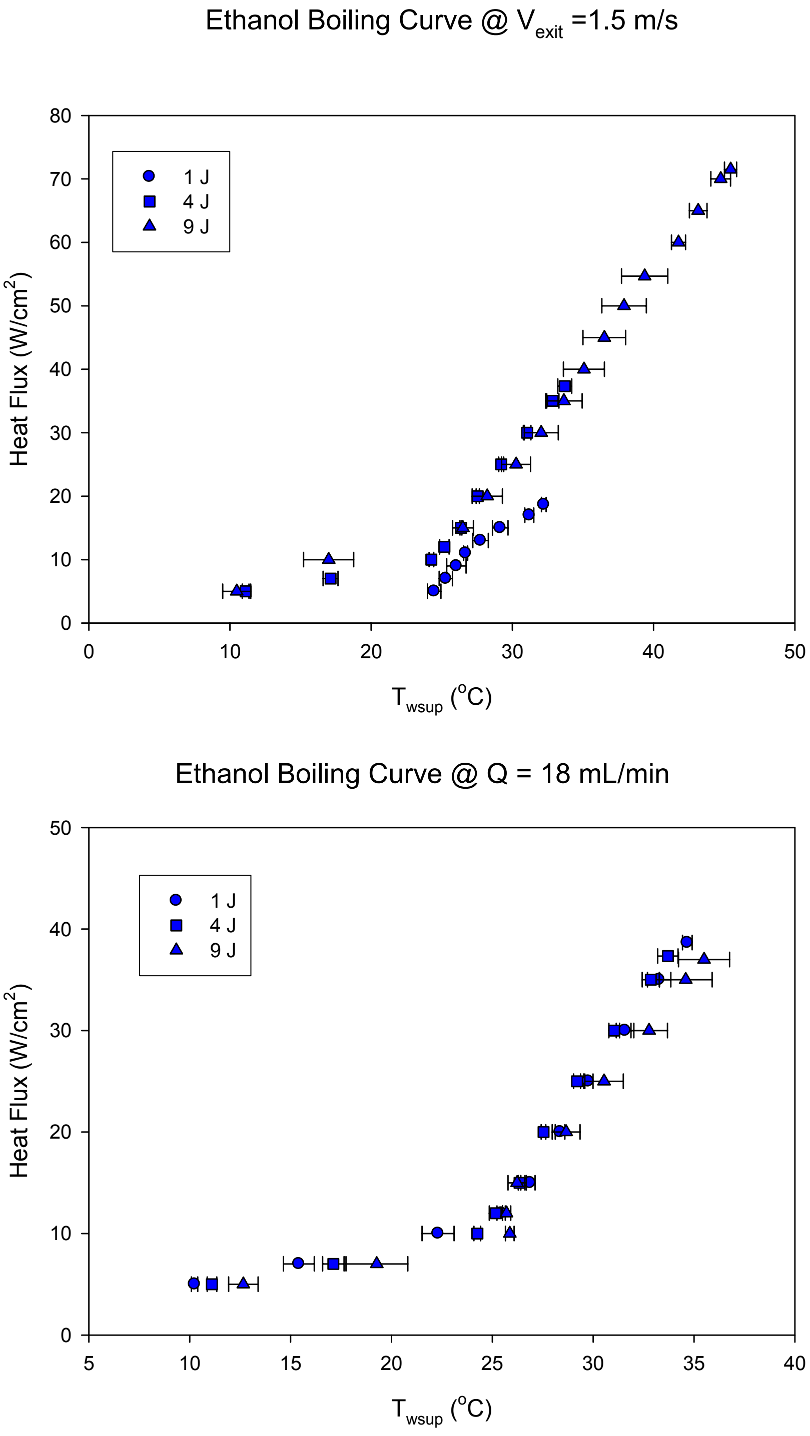 Ethanol Boiling Curve @ V_{exit} =1.5 m/s

Ethanol Boiling Curve @ Q = 18 mL/min

Fig. 80 Effect of jet number on boiling curves of ethanol

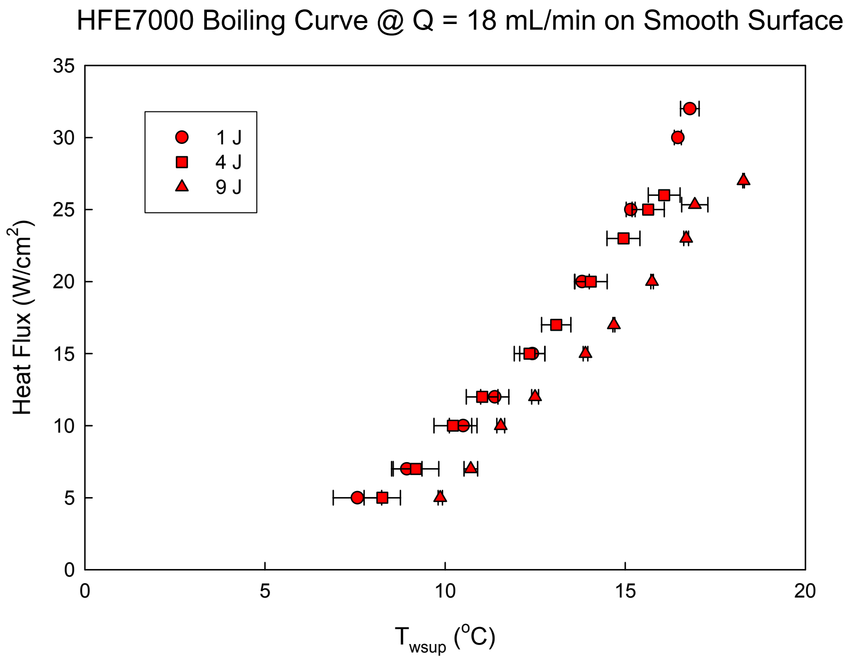

Fig. 81 Effect of jet number on boiling curves of HFE7000

9.5 Multi MJIC Summary

The experimental results of multi MJIC shows that heat transfer enhancement effect depends on fluids and testing conditions. At same Re number, multi MJIC has positive effect in most conditions. At same flowrate, it might cause negative, neutral and positive effect on water, ethanol and HFE7000, respectively. As to the CHF correlations, the data regression correlation achieves a better quality than the semi-theoretical CHF model and Monde's V-correlation. Several possible reasons are provided and discussed in the study. According to the experimental results, the heat transfer coefficient could be enhanced by using multi MJIC with water. While for ethanol and HFE7000, no obvious enhancement is observed by using multi MJIC.

CHAPTER 10. SUMMARY

In the first part of this study, EHDA method is used to generate spray and compare it with jet impingement cooling. In the second part, the experimental and analytical study are carried out on single and multi MJIC.

A testing bench is built for both EHDA cooling and MJIC experiments. During the experiments of EHDA cooling, the system is equipped with high voltage supplier and works in the atmosphere pressure. We achieved good electric insulation and good thermal conduction between the heating and measuring components. During the experiments of MJIC, the system is equipped with heavy duty condenser and runs in saturated environment. The system is sealing very well, which enable the repeating tests above 200 W/cm^2 in saturated condition. We developed a method to make thick film resistance heaters, which simulate the cooling target, power electronics elements.

In our testing range, EHDA mode could be affected by applied voltage, flowrate, nozzle height and nozzle diameter. 14 EHDA modes are observed and classified from over one thousand testing data. By reviewing previous studies and high speed images, we developed two nondimensional parameters. Using two parameters, EHDA modes, which have four degree freedom, could be separated in the EHDA mode map.

The comparison experiments of EHDA cooling and jet impingement are conducted in various conditions, we had tested with different applied voltage, flowrate, nozzle height nozzles and surfaces. The results show that the EHDA cooling could improve the heat transfer coefficient as opposed to jet impingement cooling. However, EHDA create a wide spray angle and certain amount of impinging mass would hit outside of the surface. Therefore, it is observed that EHDA method could not enhance the CHF, no matter on smooth surface or structure surface.

In the second part, according to the experiment results, the existing CHF correlation for traditional jet impingement cooling could not give the right prediction. Analytical works are carried out on the impingement boiling process, which leads to three characteristic regimes during single MJIC. Using the concepts of force balance and energy balance, a semi-theoretical CHF model is proposed. The predictive results of the new model match with the testing results of water and ethanol very well. And a CHF prediction process is presented for better utilizing this CHF model. Though the model over-predicts the CHF of HFE7000, it provides a potential explanation about the unique feature on that CHF curve. There is a peak on the CHF curve of saturated HFE7000, which could not be explained by existing CHF model. Similar trend is also found in the experiment with subcooled ethanol, which is considered due to the same reason.

As to the CHF correlation of multi MJIC, neither the semi-theoretical model nor Monde's correlation is able to precisely predict the experimental results. An experimental CHF correlation is suggested, which is generated by data regression. Base on our experimental study, the heat transfer enhancement by multi MJIC depends fluids and testing conditions. At same Re number, multi MJIC normally could enhance the CHF. However, its effect is totally different at same flowrate, it might have negative, neutral and positive effect on CHF of water, ethanol and HFE7000, respectively. The effect of multi MJIC on heat transfer coefficient also depends on fluids. Heat transfer process with water could be enhanced by using multi MJIC method. While for ethanol and HFE7000, there is no obvious enhancement by using multi MJIC.

Many interesting phenomena are observed during this study, which might be clues towards other valuable research topics. Some of them are presented in the appendix. The future work might be carried out on three aspects.

1. Experiment study the EHDA mode with other fluids, those EHDA mode data could be utilized to verify the EHDA mode map for ethanol. Further Study could evolve to explain the mode transition by fundamental mechanism.

2. The maximum heat flux in each region might be determined by experiments. When a micro jet directly impinging on the surface of the thin film alloy heater, the local heat flux would be very uniform on the heater surface. Therefore, experimental CHF in that configuration would be expressed as $Min[q''_{CHF,A1}, q''_{CHF,A2}]$.

3. Various types of structure surface would have different wetting characteristic. Experimental and analytical studies are needed to explore this effect on MJIC.

I wish that here is a starting point of another research, instead of the end of a PhD dissertation.

REFERENCES

[1] I. Mudawar, "Assessment of High Heat Flux Thermal Management Schemes," IEEE Transactions on Components and Packaging Technologies, vol. 24, pp. 122-141, 2001.

[2] D. Butterworth and G. F. Hewitt, Two-Phase Flow an Heat Transfer: Oxford University Press, 1977.

[3] B. W. Webb and C. F. Ma, "Single-phase Liquid Jet Impingement Heat Transfer," Advances in Heat Transfer, vol. 26, pp. 105-217, 1995.

[4] D. H. Wolf, F. P. Incropera, and R. Viskanta, "Local Jet Impingement Boiling Heat Transfer," International Journal of Heat Mass Transfer, vol. 39, pp. 1395-1406, 1996.

[5] N. Zuckerman and N. Lior, "Jet Impingement Heat Transfer: Physics, Correlations, and Numerical Modeling," Advances in Heat Transfer, vol. 39, pp. 565-632, 2006.

[6] J. H. Lienhard, "Liquid Jet Impingement," Journal of Annual Review of Heat Transfer, vol. 6, pp. 199-270, 1995.

[7] Z. Liu, T. Tong, and Y. Qiu, "Critical Heat Flux of Steady Boiling for Subcooled Water Jet Impingement on the Flat Stagnation Zone," Journal of Heat Transfer, vol. 126, pp. 179-183, 2004.

[8] X. Liu and J. H. Lienhard, "Extremely High Heat Fluxes Beneath Impinging Liquid Jets," Journal of Heat Transfer, vol. 115, pp. 472-476, 1993.

[9] Y. Mitsutake and M. Monde, "Ultra High Critical Heat Flux During Forced Flow Boiling Heat Transfer With an Impinging Jet," Journal of Heat Transfer, vol. 125, pp. 1038-1045, 2003.

[10] K. A. Estes and I. Mudawar, "Correlation of Sauter Mean Diameter and Critical Heat Flux for Spray Cooling of Small Surfaces," International Journal of Heat and Mass Transfer, vol. 38, pp. 2985-2996, 1995.

[11] I. Mudawar and K. A. Estes, "Optimizing and Predicting CHF in Spray Cooling of a Square Surface," Journal of Heat Transfer, vol. 118, pp. 672-679, 1996.

[12] J. R. Rybicki and I. Mudawar, "Single-phase and Two-phase Cooling Characteristics of Upward-facing and Downward-facing Sprays," International Journal of Heat and Mass Transfer, vol. 49, pp. 5-16, 2006.

[13] E. A. Silk, J. Kim, and K. Kiger, "Spray Cooling of Enhanced Surfaces: Impact of Structured Surface Geometry and Spray Axis Inclination," International Journal of Heat and Mass Transfer, vol. 49, pp. 4910-4920, 2006.

[14] R. J. Issa, "Numerical Modeling of the Dynamics and Heat Transfer of Impacting Spray for a Wide Range of Pressure," University of Pittsburgh, 2003.

[15] L. C. Chow, "High Heat Flux Spray Cooling," Annual Review of Heat Transfer, vol. 8, pp. 291-318, 1997.

[16] L. C. Chow, "Critical Heat Flux in High Heat Flux Spray Cooling," presented at Symposium on Thermal Science and Engineering in Honor of Chancellor Chang-Lin Tien, San Franscisco, CA, 1995.

[17] R.-H. Chen, L. C. Chow, and J. E. Navedo, "Optimal Spray Characteristics in Water Spray Cooling," International Journal of Heat and Mass Transfer, vol. 47, pp. 5095-5099, 2004.

[18] M. S. Sehmbey, L. C. Chow, O. J. Hahn, and M. R. Pais, "Effect of Spray Characteristics on Spray Cooling with Liquid Nitrogen," Journal of Thermophysics and Heat Transfer, vol. 9, pp. 757-765, 1995.

[19] J. E. Navedo, "Parametric Effects of Spray Characteristics on Spray Cooling Heat Transfer," University of Central Florida, 2000.

[20] C. Cho and K. Wu, "Comparison of Burnout Characteristics in Jet Impingement Cooling and Spray Cooling," presented at Proceeding of National Heat Transfer Conference, Houston, Texas, 1988.

[21] K. Estes and I. Mudawar, "Comparison of Two-Phase Electronic Cooling Using Free Jets and Spray," Journal of Electronic Packaging, vol. 117, pp. 323-332, 1995.

[22] M. Fabbri, S. Jiang, and V. K. Dhir, "A Comparative Study of Cooling of High Power Density Electronics Using Sprays and Microjets," Journal of Heat Transfer, vol. 127, pp. 38-48, 2005.

[23] J. Zeleny, "Instability of Electrified Liquid Surfaces," Physics Reviews, vol. 10, pp. 1-6, 1917.

[24] J. B. Fenn, M. Mann, C. K. Meng, S. F. Wong, and C. M. Whitehouse, "Electrospray Ionization for Mass Spectrometry of Large Biomolecules," Science, vol. 246, pp. 64-71, 1989.

[25] J. Wei, W. Shui, F. Zhou, Y. Lu, K. Chen, G. Xu, and P. Yang, "Naturally and Externally Pulsed Electrospray," Mass Spectrometry Reviews, vol. 21, pp. 148-162, 2002.

[26] D. Michelson, Electrostatic Atomization. Bristol: Adam Hilger, 1990.

[27] G. Bailey, Electrostatic Spraying of Liquids: Research Studies Press, 1988.

[28] G. Taylor, "Disintegration of Water Drops in an Electric Field," Proceedings of the Royal Society of London, Series A, vol. 280, pp. 383-397, 1964.

[29] J. M. Grace and J. C. M. Marijnissen, "A Review of Liquid atomization by Electrical Means," Journal of Aerosol Science, vol. 25, pp. 1005-1019, 1994.

[30] J. P. Borra, Y. Tombette, and P. Ehouarn, "Influence of Electric Field Profile and Polarity on the Mode of EHDA Related to Electric Discharge Regime," Journal of Aerosol Science, vol. 30, pp. 913-925, 1999.

[31] R.Ragucci, F. Fabiani, A. Cavaliere, P. Muscetta, and C. Noviello, "Characterization of stablity regimes of electrohydrodynamically enhanced atomization.," in Experimental Thermal and Fluid Science, vol. 21, 2000, pp. 156-161.

[32] J. M. Grace and P. F. Dunn, "Droplet Motion in an Electrohydrodynamic Fine Spray," Experiments in Fluids, vol. 20, pp. 153-164, 1996.

[33] X. Feng and J. Bryan, "Control of Liquid Impingement with Electrical Field," presented at ASME International Mechanical Engineering Congress and Exposition, Orlando, Florida, 2005.

[34] H. Park, K. Kim, and S. Kim, "Effects of a Guard Plate on the Characteristics of an Electrospray in the Cone-jet Mode," Journal of Aerosol Science, vol. 35, pp. 1295?312, 2004.

[35] I. W. Lenggoro, K. Okuyama, J. F. n. d. l. Morat, and N. Tohge, "Preparation of ZnS Nanoparticles by Electrospray Pyrolysis," in Journal of Aerosol Science, vol. 21, 2000, pp. 121-136.

[36] A. Jaworek and A. Krupa, "Classification of the Modes of EHD Spraying," Journal of Aerosol Science, vol. 30, pp. 873-893, 1999.

[37] J. C. Ijsebaert, K. B. Geerse, J. C., M. Marijnissen, J.-W. J., and L. a. P. Zanen, "Electrohydrodynamic Atomization of Drug Solutions for Inhalation Purposes," Journal of Applied Physiology, vol. 91, pp. 2735-2741, 2001.

[38] P. F. Dunn and S. R. Snarski, "Velocity Component and Diameter Distribution Characteristics of Droplets within Two Interacting Electrohydrodynamic Sprays," Physical Fluids A, vol. 3, pp. 492-494, 1991.

[39] P. F. Dunn and S. R. Snarski, "Droplet Diameter, Flux, and Total Current Measurements in an Electrohydrodynamic Spray," Journal of Applied Physics, vol. 71, pp. 80-84, 1992.

[40] A. L. Huebner, "Disintegration of Charged Liquid Jet: Results with Isopropyl Alcohol," Science, vol. 168, pp. 118-119, 1970.

[41] M. Cloupeau and B. Prunet-Foch, "Recipes Electrohydrodynamic Spraying Functioning Modes: A Critical Review," Journal of Aerosol Science, vol. 25, pp. 1021-1036, 1994.

[42] M. M. Hohman, M. Shin, G. Rutledge, and M. P. Brenner, "Electrospinning and electrically forced jets. I. Stability theory," Physical of Fluids, vol. 13, pp. 2201-2220, 2001.

[43] M. M. Hohman, M. Shin, G. Rutledge, and M. P. Brenner, "Electrospinning and electrically forced jets. II. Applications," Physical of Fluids, vol. 13, pp. 2221-2236, 2001.

[44] M. Cloupeau and B. Prunet-Foch, "Electrostatic Spraying of liquid: Main functioning modes," in Journal of Electrostatics, vol. 25, 1990, pp. 165-184.

[45] J. F. D. L. Mora and I. G. Loscertales, "The Current Emitted by Highly Conducting Taylor Cones," Journal of Fluid Mechanics, vol. 260, pp. 155-184, 1994.

[46] J. M. Lopez-Herrera and A. M. Ganan-Calvo, "A Note on Charged Capillary Jet Breakup of Conducting Liquids: Experimental Validation of a Viscous One-Dimensional Model," Journal of Fluid Mechanics, vol. 501, pp. 303-326, 2004.

[47] A. M. Ganan-Calvo and A. B. J.Davila, "Current and Droplet Size in the Electrospraying of Liquids: Scaling Laws," Journal of Aerosol Science, vol. 28, pp. 249-275, 1997.

[48] J. Rosell-Llompart and J. F. D. L. Mora, "Generation of Monodisperse Droplets 0.3 to 4 um in Diameter from Electrified Cone-Jets of Highly Conducting and Viscous Liquids," Journal of Aerosol Science, vol. 25, pp. 1093-1119, 1994.

[49] F. J. Higuera and A. Barrero, "Electrosprays of Very Polar Liquids at Low Flow Rates," Physics of Fluids, vol. 17, pp. 018104, 2005.

[50] A. R. Jones and K. C. Thong, "The Production of Charged Monodisperse Fuel Droplets by Electrical Dispersion," Journal of Physics D: Applied Physics, vol. 4, pp. 1159-1166, 1971.

[51] H. Watanabe, T. Matsuyama, and H. Ymamoto, "Experimental Study on Electrostatic Atomization of Highly Viscous Liquids," Journal of Electrostatics, vol. 57, pp. 183-197, 2002.

[52] A. M. Ganan-Calvo, J.C.Lasheras, and A. B. J.Davila, "The Electrostatic Spray Emitted from an Electrified Conical Meniscus," Journal of Aerosol Science, vol. 25, pp. 1121-1142, 1994.

[53] O. Wilhelm, L. Madler, and S. E. Pratsinis, "Electrospray Evaporation and Deposition," Journal of Aerosol Science, vol. 34, pp. 815-836, 2003.

[54] A. Jaworek and A. Krupa, "Jet and Drops Formation in Electrohydrodynamic Spraying of Liquids," Experiments in Fluids, vol. 27, pp. 43-55, 1999.

[55] K. Sung and C. S. Lee, "Factors influencing liquid breakup in electrohydrodynamic atomization," Journal of Applied Physics, vol. 96, pp. 3956-3961, 2004.

[56] M. Monde, "Critical Heat Flux in a Forced Convective Subcooled Boiling with an Impinging Jet," Journal of Heat Transfer, vol. 7, pp. 515~520, 1994.

[57] Y. Katto and S. Yokoya, "Critical Heat Flux on a Disc Heater Cooled by a Circular Jet of Saturated Liquid Impinging at the Center," International Journal of Heat and Mass Transfer, vol. 31, pp. 219-227, 1988.

[58] A. Sharan and J. H. Lienhard, "On Predicting Burnout in the Jet-Disk Configuration. Journal of Heat Transfer," Journal of Heat Transfer, vol. 107, pp. 398-401, 1985.

[59] J. H. Lienhard and R. Eichorn, "Peak Boiling Heat Flux on Cylinders in a Cross Flow," International Journal of Heat and Mass Transfer, vol. 19, pp. 1135-1142, 1976.

[60] Y. Haramura and Y. Katto, "A New Hydrodynamic Model of Critical Heat Flux, Applicable Widely to Both Pool and Forced Convection Boiling on Submerged Bodies in Saturated Liquids," International Journal of Heat and Mass Transfer, vol. 26, pp. 389-399, 1983.

[61] M. Monde, "Critical Heat Flux in Saturated Forced Convective Boiling on a Heated Disk With an Impinging Jet, a New Generalized Correlation," W鋜me Stoff黚ertrag, vol. 19, pp. 205-209, 1985.

[62] M. Monde and T. Inoue, "Critical Heat Flux in Saturated Forced Convection Boiling on a Heated Disk with Multiple Impinging Jets," Journal of Heat Transfer, vol. 113, pp. 722?27, 1991.

[63] M. T. Meyer, I. Mudawar, C. E. Boyack, and C. A. Hale, "Single-phase and Two-phase Cooling with an array of Rectangular Jet," International Journal of Heat and Mass Transfer, vol. 49, pp. 17-29, 2006.

[64] C. H. Oh, J. H. Lienhard, H. F. Younis, R. S. Dahbura, and D. Michels, "Liquid Jet Array Cooling Modules for High Heat Flux," in Fluid Mechanics and Transport Phenomena, vol. 44, 1998, pp. 769-779.

[65] E. N. Wang, L. Zhang, L. Jiang, J.-M. Koo, J. G. Maveety, E. A. Sanchez, K. E. Goodson, and T. W. Kenny, "Micromachined Jets for Liquid Impingement Cooling of VLSI Chips," Journal of Microelectromechanical System, vol. 13, pp. 833-842, 2004.

[66] M. Fabbri, "Cooling of Electronic Components Using Arrays of Microjets," UCLA, 2004.

[67] M. Fabbri and V. K. Dhir, "Optimized Heat Transfer for High Power Electronic Cooling Using Arrays of Microjets," Journal of Heat Transfer, vol. 127, pp. 760-769, 2005.

[68] Y. Pan and B. W. Webb, "Heat Transfer Characteristics of Arrays of Free Surface Liquid Jets," Journal of Heat Transfer, vol. 117, pp. 878-883, 1995.

[69] V. P. Carey, Liquid-Vapor Phase-Change Phenomena: Taylor & Francis, 1992.

[70] M. Monde and Y. Katto, "Burnout in a High Heat-Flux Boiling System With an Impingement Jet," in International Journal of Heat Mass Transfer, vol. 21, 1978, pp. 195-305.

[71] D. A. Saville, "Stability of Electrically Charged Viscous Cylinders," Physics of Fluids, vol. 14, pp. 1095-1099, 1971.

[72] D. A. Saville, "Electrohydrodynamic Stability: Effects of Charge Relaxation at the Interface of a Liquid Jet," Journal of Fluid Mechanics, vol. 48, pp. 815-827, 1971.

[73] A. J. Mestel, "Electrohydrodynamic Stability of a Slightly Viscous Jet," Journal of Fluid Mechanics, vol. 274, pp. 93-113, 1994.

[74] A. J. Mestel, "Electrohydrodynamic Stability of a Highly Viscous Jet," Journal of Fluid Mechanics, vol. 312, pp. 311-326, 1996.

[75] D. C. Wadsworth and I. Mudawar, "Enhancement of Single-Phase Heat Transfer and Critical Heat Flux from an Ultra-High-Flux Simulated Microelectronic Heat Source to a Rectrangular Iminging Jet of Dielectric Liquid," Journal of Heat Transfer, vol. 114, pp. 764-768, 1992.

[76] D. Copeland, "Single-phase and Boiling Cooling of Small Pin Fin Arrays by Multiple Slot Nozzle Suction and Impingement," Thermal Phenomena in Electronic Systems, pp. 16-22, 1994.

[77] D. Priedeman, V. Callahan, and B. W. Webb, "Enhanced Surface Liquid Jet Impingement Heat Transfer with Surface Modifications," Journal of Heat Transfer, vol. 116, pp. 486-489, 1994.

[78] I. Mudawar and D. E. Maddox, "Enhancement of Critical Heat Flux from High Power Microelectronic Heat Sources in a Flow Channel," Journal of Electronic Packaging, vol. 112, pp. 241-248, 1990.

VITA

Xin Feng was born in Wuzhen, a famous water town in east China. He attended Jiaxing No. 1 high school in 1993. In 1996, he entered Shanghai Jiao Tong University (SJTU) and studied in Refrigeration and Cryogenics Engineering. He received BS degree in mechanical engineering in 2000, and received BA degree in accounting as a minor. In 2003, several life events come into his life. He received MS degree in that Feb. In the Apr., he was awarded Danfoss scholarship for his outstanding performance in SJTU. In the May, he started his first formal job in Carrier China Operations. In the Aug., he married a beautiful and lovely girl, Yamin Luo. In the Nov., he left China and went to Columbia, Missouri. In the Dec., he got the offer from Dr. Robert Tzou to pursue the PhD degree. In 2004, he started this current research directed by Dr. James Bryan.

Appendix A. EHDA Modes of Water, Ethanol and HFE7000

During the experiments for EHDA mode identification, we tried different types of fluids, nozzle and frequency of AC voltage. Many videos have been recorded under various testing conditions. In the following sections, we are going to show some selective EHDA phenomena.

I. Experimental Observation of EHDA Mode with Water

Compare with HFE7000 and ethanol, water is so conductive that severe arcing would take place when V = 8 kV, H = 1 cm. That problem could be eliminated by increasing the height. We show three sets of images in the Fig. 82, and testing parameters are listed. At H =3 cm and H = 5 cm, the transition trend of water is similar to that of ethanol. With the relative low applied voltage, droplet size would reduce and frequency of dripping would increase, until the spindle mode occurs.

H = 1 cm, Water, Delrin, $d_i = 0.25$ mm, $d_o = 4$ mm, $Q = 4.05 * 10^{-9}$ m^3/s

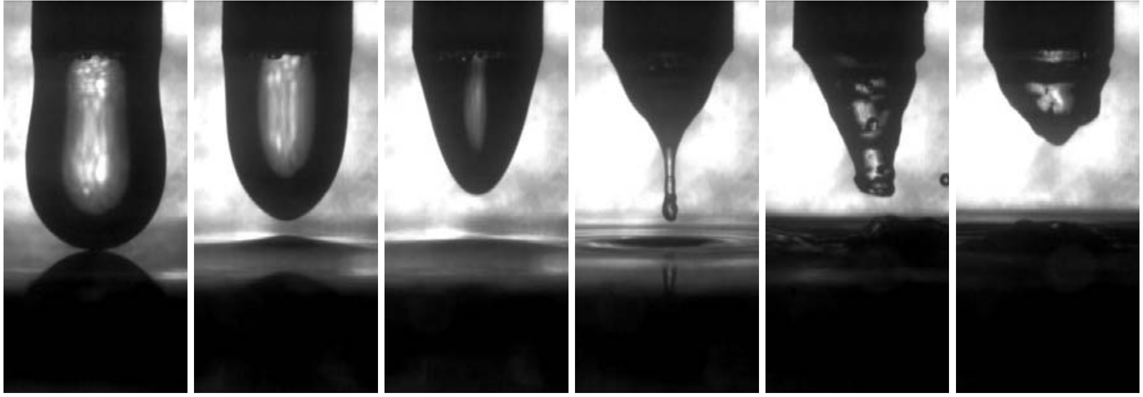

V = 0 2 kV 4 kV 6 kV 8 kV 10 kV

H = 3 cm, Water, Delrin, $d_i = 0.25$ mm, $d_o = 4$ mm, $Q = 4.05 * 10^{-9}$ m^3/s

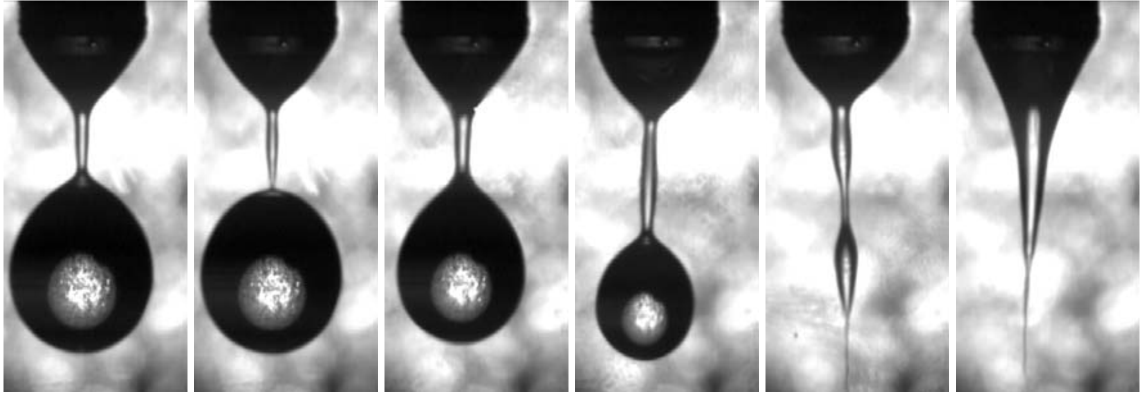

H = 5 cm, Water, Delrin, $d_i = 0.25$ mm, $d_o = 4$ mm, $Q = 4.05 * 10^{-9}$ m^3/s

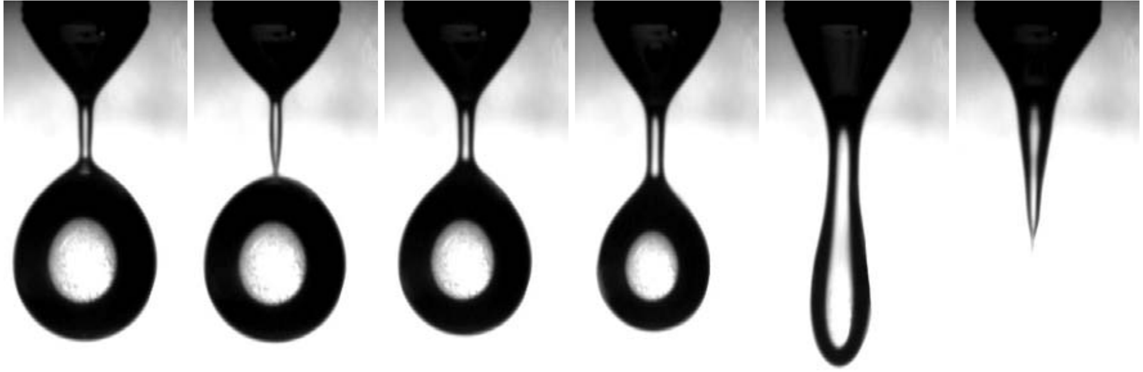

Fig. 82 High speed images of EHDA mode of water with different height and voltage

With higher flowrate, the ramified jet spray mode could be generated. In the Fig. 83, we illustrate the EHDA modes of water and ethanol under same condition and testing parameters are listed. Though there is a “swing tail” under the liquid meniscus, it is much short and thin due to strong surface tension. Therefore the droplets size during ramified jet spray with water is larger than that of ethanol.

Water, Q = 6.71 $*10^{-8}$ m^3/s, Delrin, d_i =0.25 mm, d_o = 4 mm, V = 10 kV,   H = 5 cm

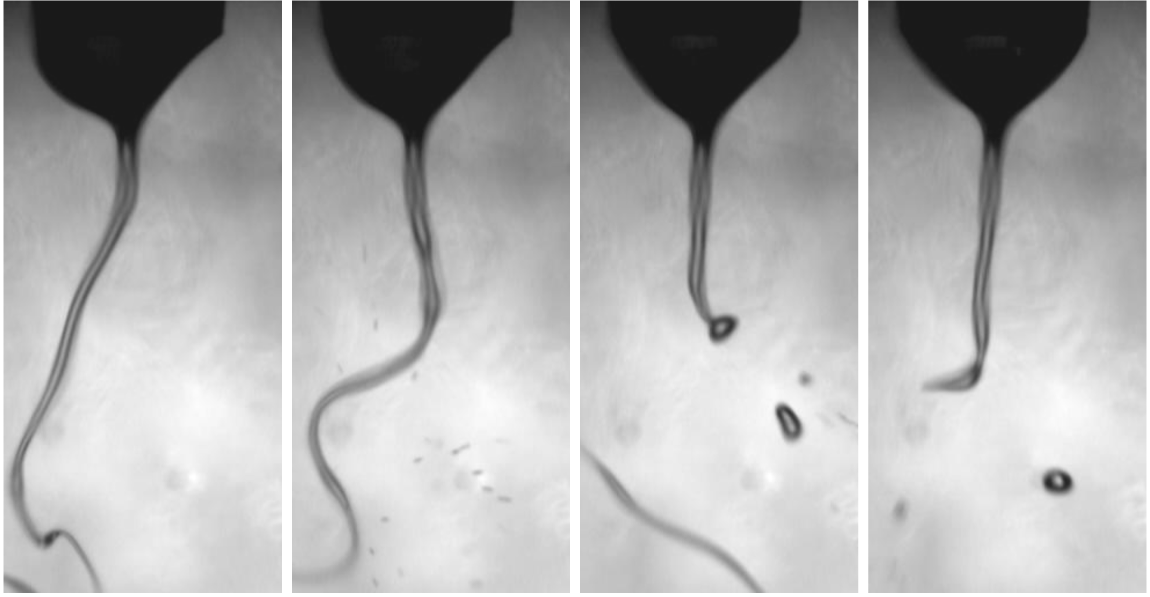

T = 0 T = 2 ms T = 4 ms T = 6 ms

Ethanol, Q = 6.57 $*10^{-8}$ m^3/s, Delrin, d_i = 0.25 mm, d_o = 4 mm, V = 10 kV, H = 5 cm

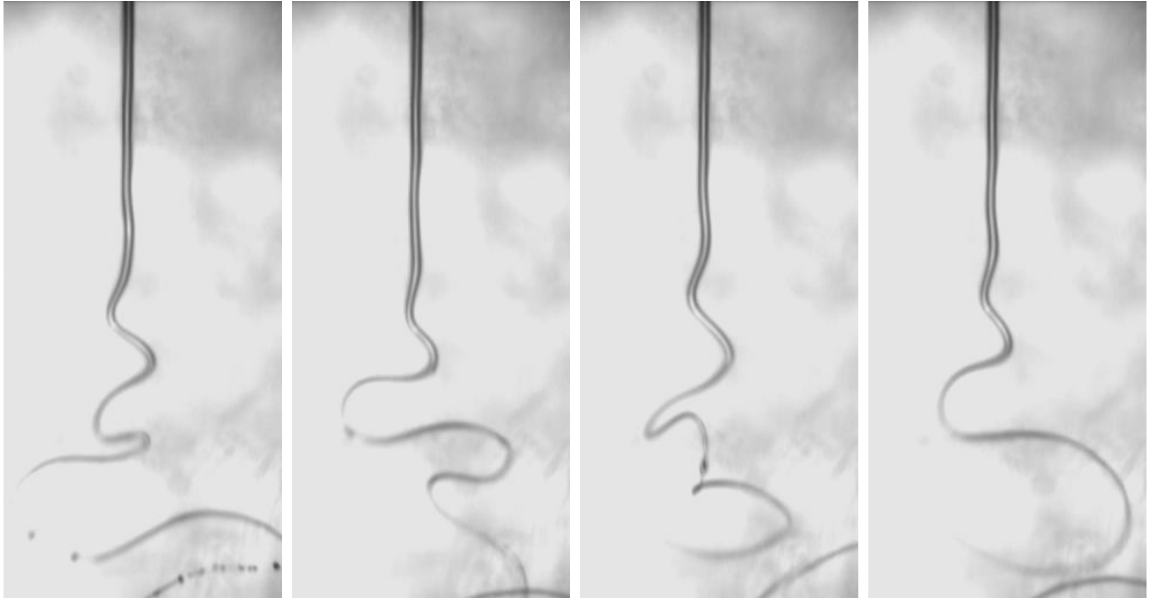

T = 0 T = 2 ms T = 4 ms T = 6 ms

Fig. 83 High speed images showing RJS mode of water and ethanol in the same conditions

II. Experimental Observation of EHDA Mode with Ethanol

In order to compare the delrin and acrylic nozzle, we conducted the EHDA experimental with two nozzles with identical parameters except for the material. Within a wide range of flowrate and voltage, we found that EHDA modes are very similar under same testing conditions. The static images and testing parameters are shown in Fig. 84 and Fig. 85.

Delrin, $Q = 0.2$ ml/s, $d_i = 1$ mm, $d_o = 4$ mm, $H = 1$ cm, Ethanol

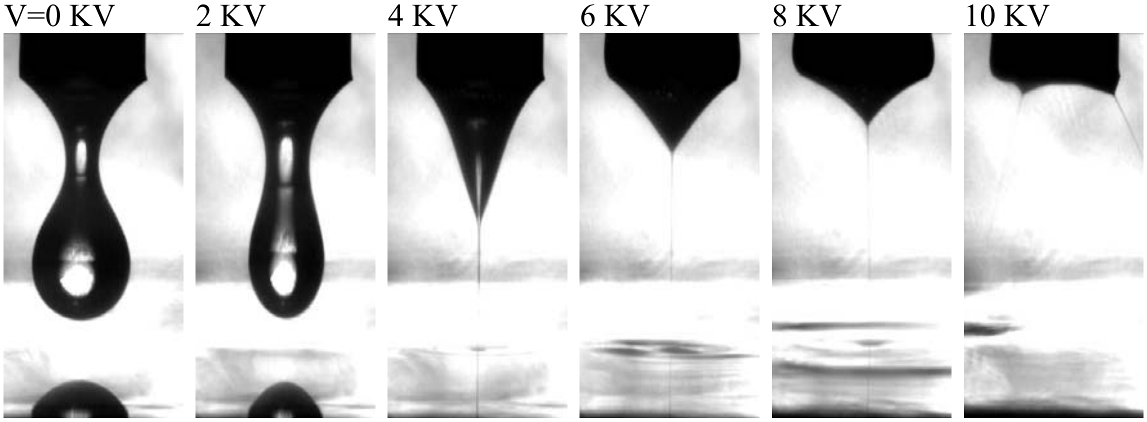

Delrin, Q=2.8 ml/s, $d_i = 1$ mm, $d_o = 4$ mm, $H = 1$ cm, Ethanol

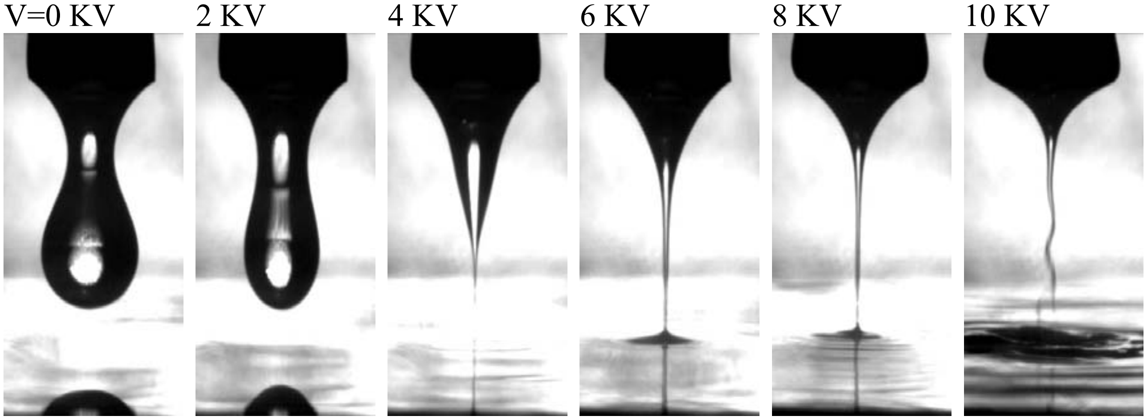

Delrin, Q=7.4 ml/s, $d_i = 1$ mm, $d_o = 4$ mm, $H = 1$ cm, Ethanol

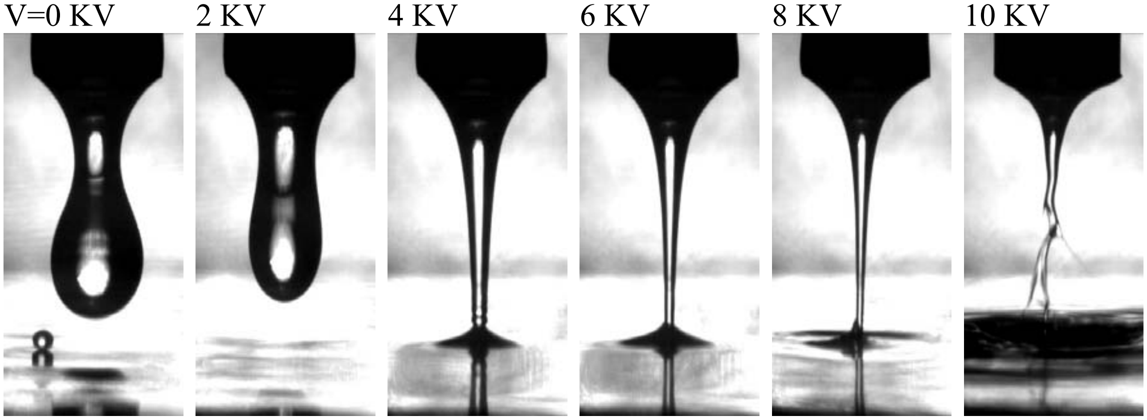

Fig. 84 Comparison the effect of nozzle material on EHDA modes (delrin nozzle)

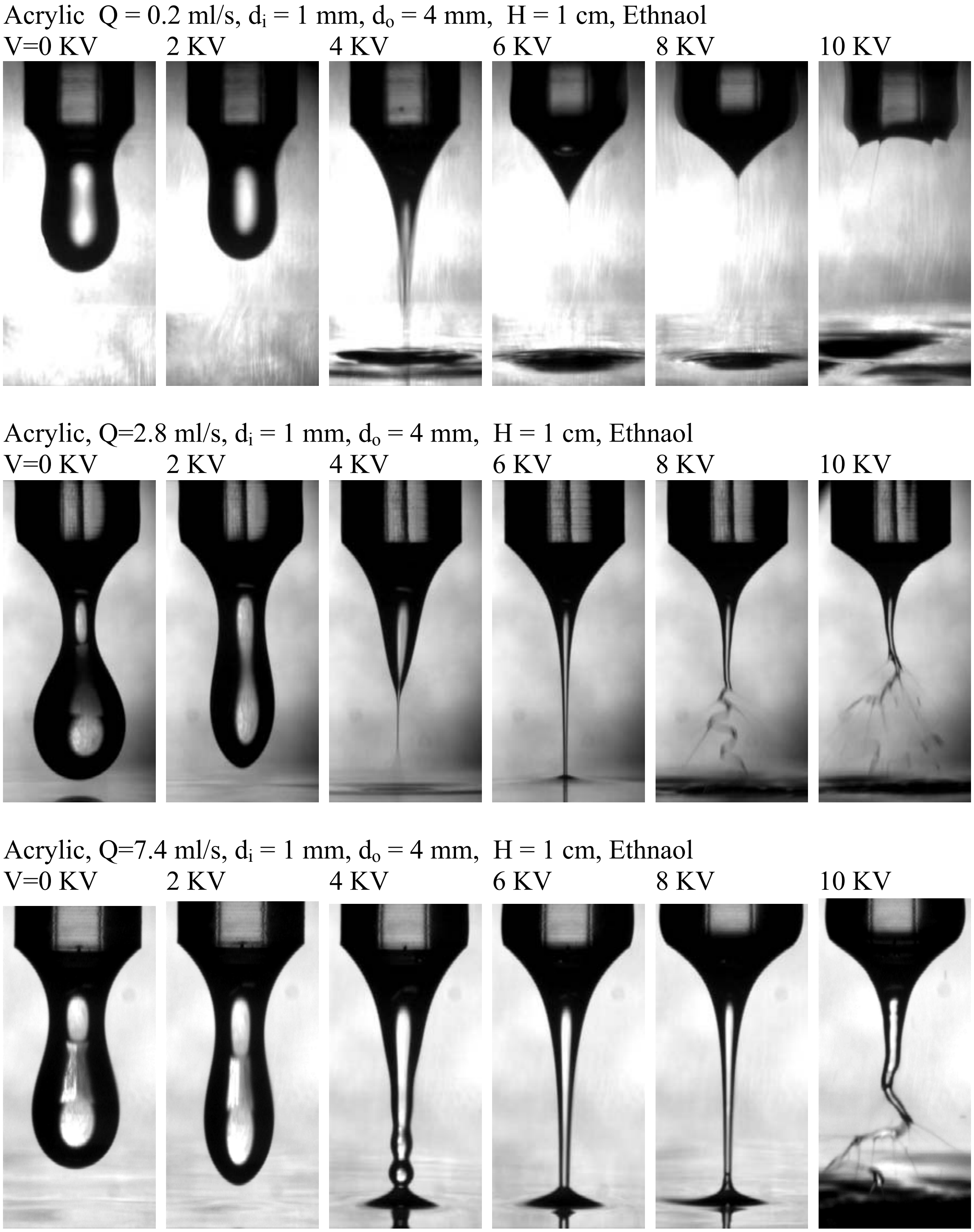

Acrylic Q = 0.2 ml/s, d_i = 1 mm, d_o = 4 mm, H = 1 cm, Ethnaol

Acrylic, Q=2.8 ml/s, d_i = 1 mm, d_o = 4 mm, H = 1 cm, Ethnaol

Acrylic, Q=7.4 ml/s, d_i = 1 mm, d_o = 4 mm, H = 1 cm, Ethnaol

Fig. 85 Comparison the effect of nozzle material on EHDA modes (acrylic nozzle)

The outside diameter of EHDA nozzle could affect the flow pattern. We show two sets of images in Fig. 86, and testing parameters are listed. At low applied voltage, a large liquid meniscus would be generated under the influence of large D_o. At high applied voltage, there are several cone jet sprays generated at the rim of the nozzle, no mater with relative low flowrate or high flowrate.

Q = 0.2 ml/s, Ethanol, Brass, d_i = 0.25 mm, d_o = 9 mm, H = 1 cm

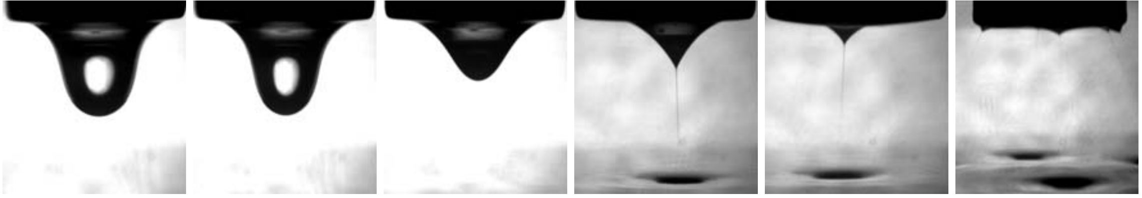

Q = 2.8 ml/s, Ethanol, Brass, d_i = 0.25 mm, d_o = 9 mm, H = 1 cm

Fig. 86 High speed images of EHDA from a nozzle with a large outside diameter

As the applied voltage, we had tested several types of voltage form, such as positive DC, negative DC and positive or negative AC. Three types of AC wave forms, such as sine, triangular and rectangular wave, had been tested during the EHDA impingement cooling with AC source. We found that the wave form does not have obvious influence on the EHDA mode or heat transfer performance. But there is an AC frequency limitation for EHDA process. We found that the EHDA phenomena gradually disappeared in our setup when the frequency above 1 kHZ. In Fig. 87, we illustrate the EHDA impingement cooling with two kinds of AC voltage. The testing parameters are listed in the figures. We could observe the propulsion wave on the surface of liquid jet when the voltage turning on. The propulsion time is about 0.5 ms, which matches with our previous observation about the frequency limitation. The EHDA flow patterns are different under two different frequency voltages. But from the temperature measurement, we have not found obvious difference by two different frequency voltages during EHDA impingement cooling.

Stainless Steel Nozzle, d_i = 0.25 mm, d_o = 0.47mm, H = 0.75 cm, Q = 3ml/min
f =10Hz 0-7 kV Rectangular Pulse, Duty Cycle = 50%, Heat Flux = 30 W/cm^2

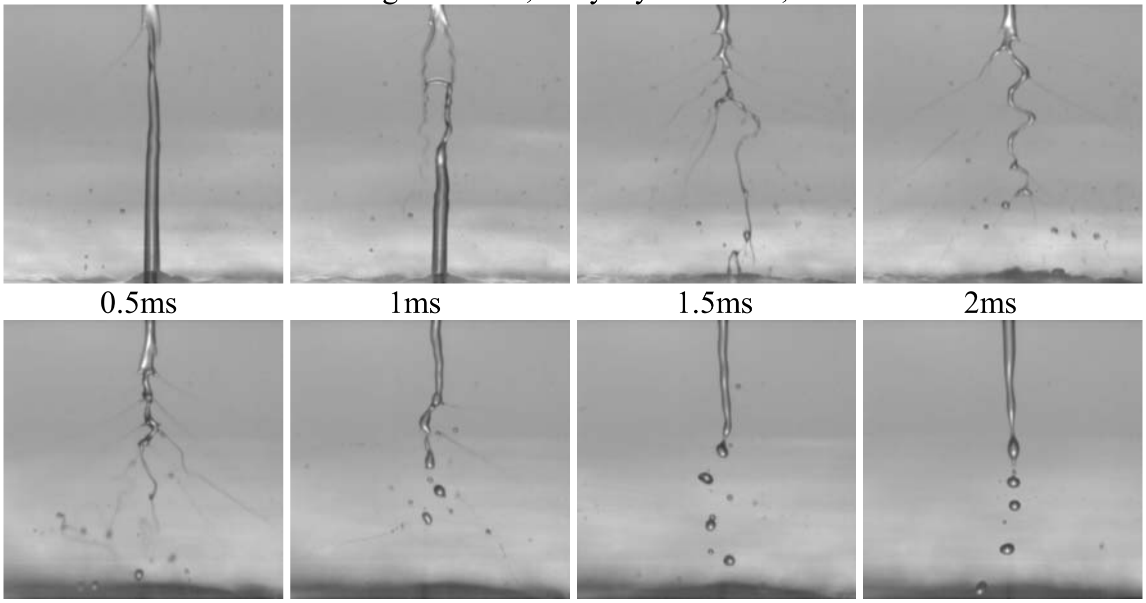

0.5ms 1ms 1.5ms 2ms

50ms 50.5ms 51ms 52ms

Stainless Steel Nozzle, d_i = 0.25 mm, d_o = 0.47mm, H = 0.75 cm, Q = 3ml/min
f =100Hz 0-7 kV Rectangular Pulse, Duty Cycle = 50%, Heat Flux = 30 W/cm^2

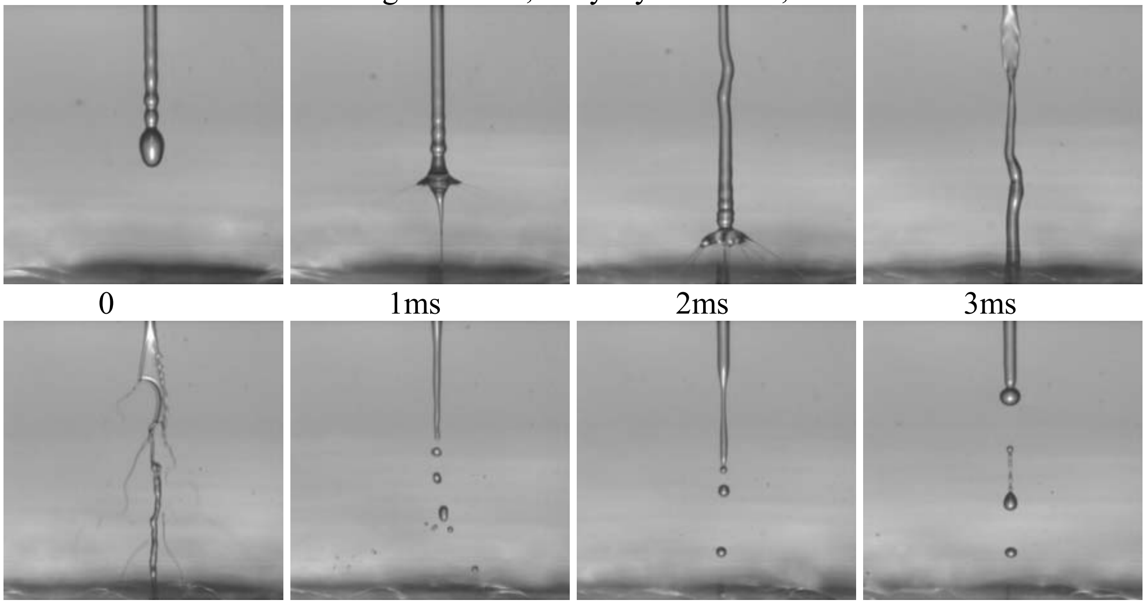

0 1ms 2ms 3ms

4ms 5ms 6ms 7ms

Fig. 87 Dynamic images of EHDA impingement cooling under different AC voltages

III. Experimental Observation of EHDA Mode with HFE7000

Some interesting EHDA phenomena are observed with HFE 7000. Since the conductivity of HFE7000 is so low (<10^{-6} S/m), applied voltage could reach 28 kV without arcing. Here are two sets of EHDA images about HFE7000.

The first set of images is captured at a relative high flowrate and small height and testing parameters are listed in the figure. (See Fig. 88) We could observe that bridging mode at 10 kV. When the applied voltage exceeds about 12 kV, we find a new EHDA mode. In that case, the liquid bridge is over charged so that extra charges would pull out liquid and form quite a few of "fingers" near the electronode. Due the external electric field, those fingers would be attracted to the ground plane.

Stainless Steel Nozzle, d_i = 0.25 mm, d_0=0.47mm, H=0.75 cm, Q = 4.41ml/min

0kV

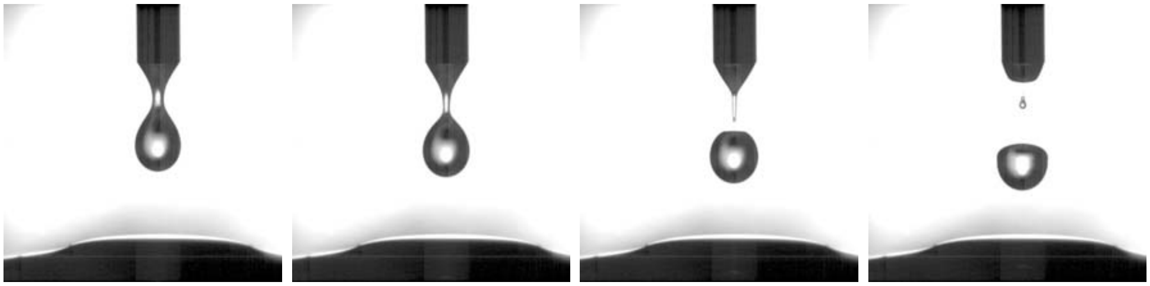

0 2ms 4ms 6ms

5kV

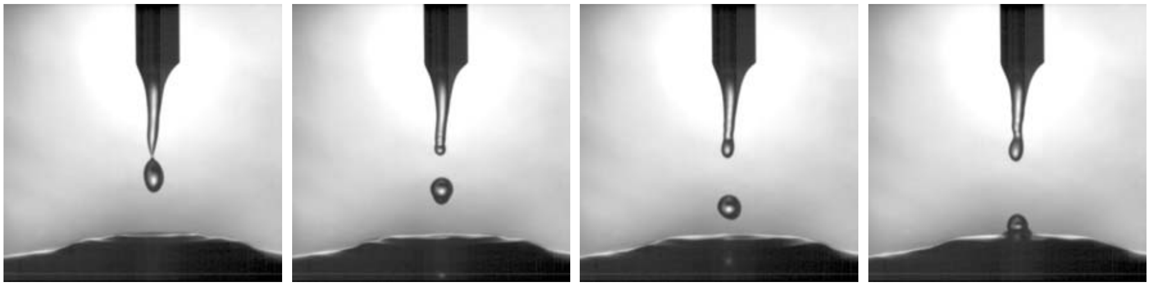

0 2ms 4ms 6ms

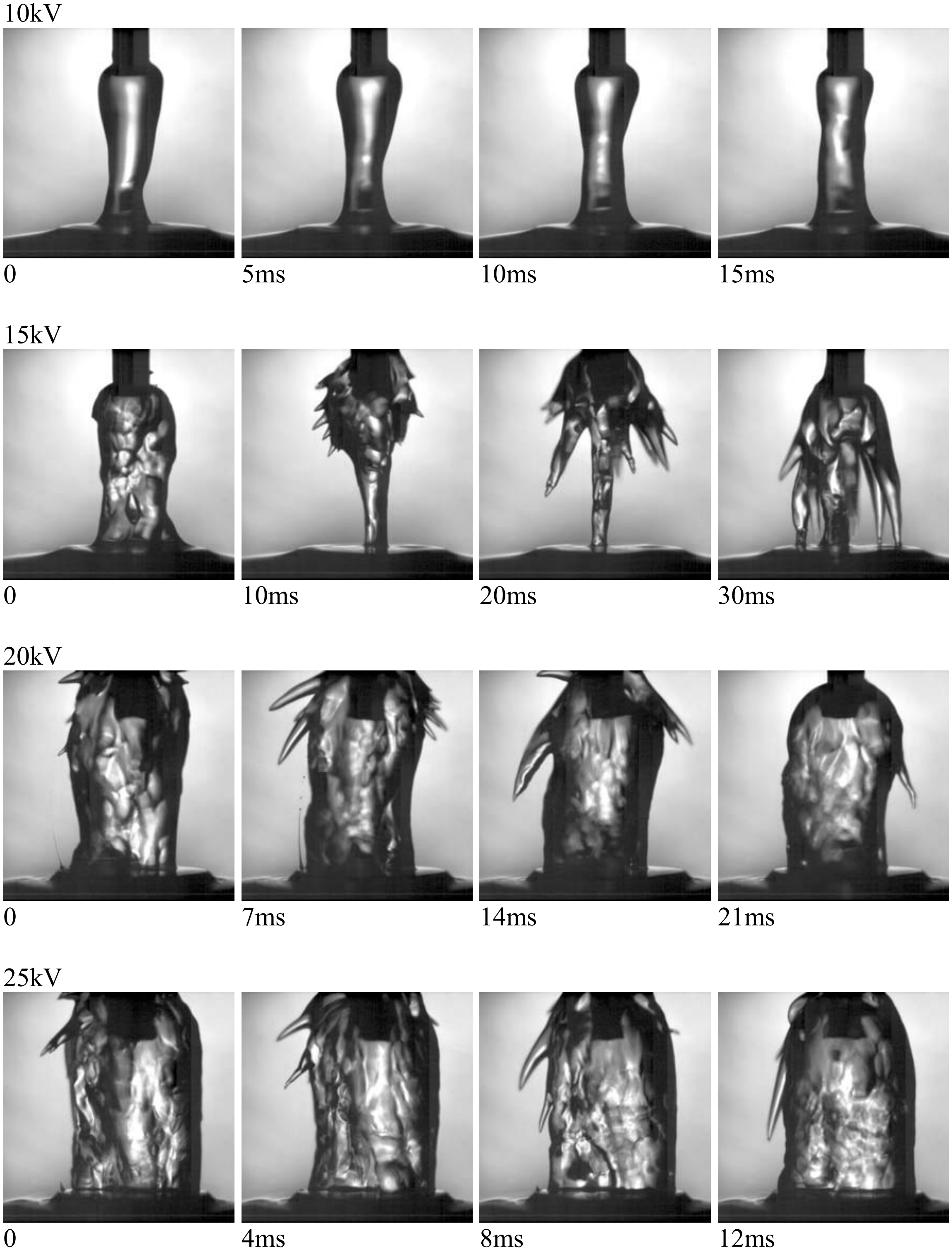

Fig. 88 Dynamic images of EHDA mode of HFE7000 with H=0.75 cm, Q = 4.41ml/min

The second set of images is captured at a relative low flowrate and large height. (See Fig. 89) By increasing the applied voltage, a new EHDA mode is observed that several liquid cones grow with applied voltage at the tip of S.S nozzle. It is suspected that each liquid cone should be a single cone jet spray. The gravity and electrostatic forces among those cones are well stabilized within the cones.

Stainless Steel Nozzle, $d_i = 0.25$ mm, $d_0 = 0.47$ mm, $H = 2$ cm, $Q = 0.6$ ml/min

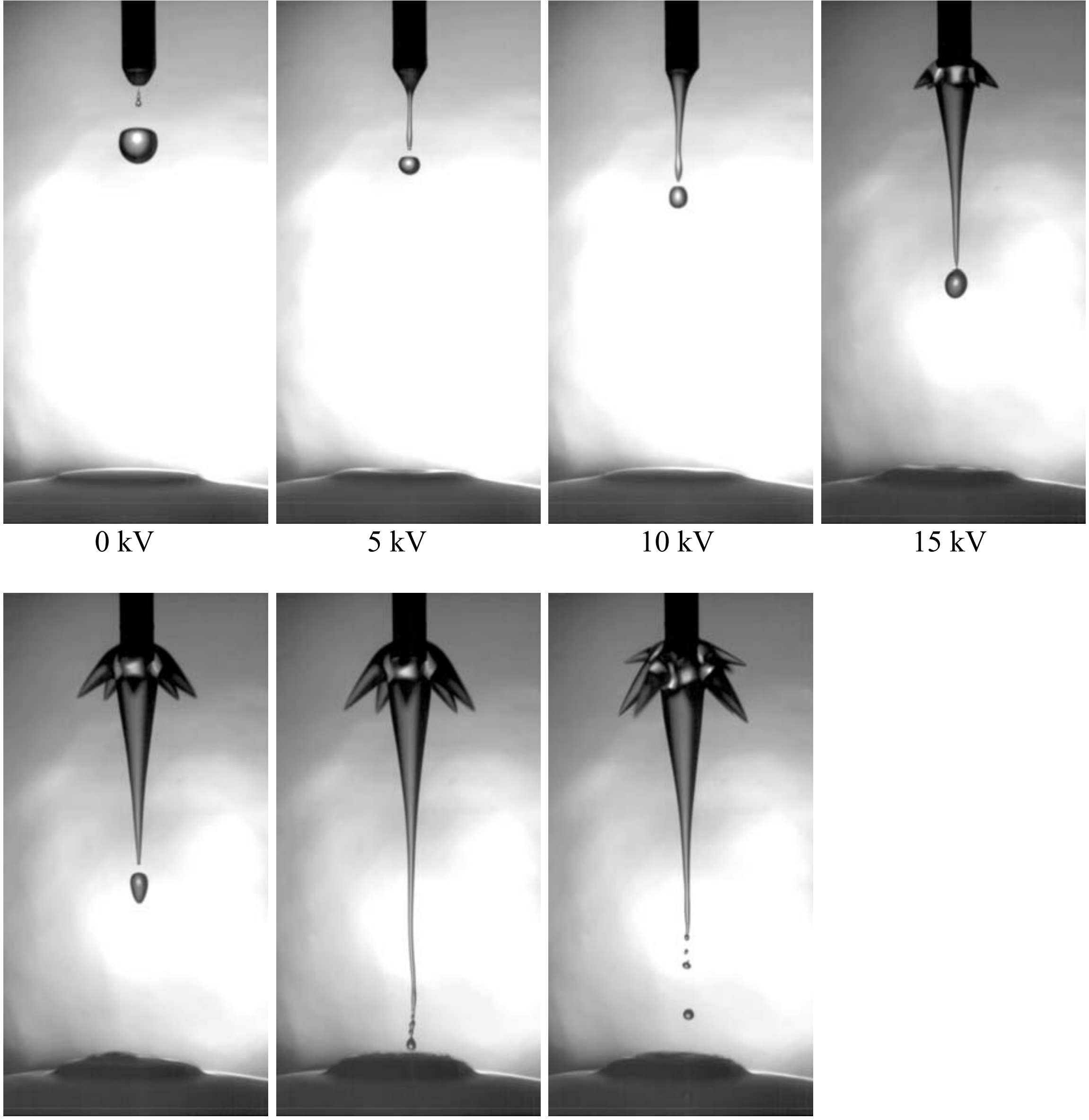

0 kV 5 kV 10 kV 15 kV

20 kV 25 kV 28 kV

Fig. 89 Static images of EHDA mode of HFE7000 with H = 2 cm, Q = 0.6 ml/min

Appendix B. Mode Data of EHDA with Ethanol

Table 23 Mode Data of EHDA with ethanol (Part 1)

H (cm) **0.5**

d_i (mm) **0.25**

d_o (mm) **4**

Q (ml/min)	We	Applied Voltage, + dc (kV)										
		0	1	2	3	4	5	6	7	8	9	10
0.1	0.04	OB	OB	OB	OB	B	B	B	B	B	B	B
0.2	0.21	OB	OB	OB	OB	B	B	B	B	B	B	B
0.6	1.4	OB	OB	OB	OB	B	B	B	B	B	B	B
1.1	4.9	OB	OB	OB	J/B	B	B	B	B	B	B	B
2.2	21	OB	BD	J	J	B	B	B	B	B	B	B
2.8	34	BD	BD	J	J	B	B	B	B	B	B	B
3.9	69	J	J	J	J	B	B	B	B	B	B	B
5.5	133	J	J	J	J	J	B	B	B	B	B	B
7.4	242	J	J	J	J	J	B	B	B	B	B	B
13.7	829	J	J	J	J	J	J	B	B	B	B	B

H (cm) **1**

d_i (mm) **0.25**

d_o (mm) **4**

Q (ml/min)	We	Applied Voltage, + dc (kV)										
		0	1	2	3	4	5	6	7	8	9	10
0.1	0.04	TD	TD	TD	TD	SS	CJS	CJS	CJS	CJS	CJS	MCS
0.2	0.21	TD	TD	TD	TD	SS	CJS	CJS	CJS	CJS	CJS	MCS
0.6	1.4	TD	TD	TD	TD	SS	SS	SS	CJS	CJS	CJS	OMS
1.1	4.9	TD	TD	TD	TD	SS	SS	CJS	RJS	RJS	RJS	RJS
2.2	21	TD	TD	TD	J	J	J	J	J/RJS	J/RJS	RJS	RJS+CJS
2.8	34	TD	TD	J	J	J	J	J	J	J	RJS	RJS+CJS
3.9	69	J	J	J	J	J	J	J	J	J	RJS	RJS
5.5	133	J	J	J	J	J	J	J	J	J	J	J
7.4	242	J	J	J	J	J	J	J	J	J	J	J
13.7	829	J	J	J	J	J	J	J	J	J	J	J

H (cm) **2**

d_i (mm) **0.25**

d_o (mm) **4**

Q (ml/min)	We	Applied Voltage, + dc (kV)										
		0	1	2	3	4	5	6	7	8	9	10
0.1	0.04	D	D	D	D	D	SS	SS	SS	CJS	CJS	CJS
0.2	0.21	D	D	D	D	D	D	SS	SS	SS	SS	CJS
0.6	1.4	D	D	D	D	D	SS	SS	SS	SS	ORS	CJS
1.1	4.9	D	D	D	D	D	SS	SS	ORS	ORS	ORS	ORS
2.2	21	D	D	D	D	SS	SS	ORS	ORS	ORS	RJS	RJS
2.8	34	D	D	D	D	D	SS	J	RJS	RJS	RJS	RJS
3.9	69	D	D	D	D	D	SS	J	J	J	RJS	RJS
5.5	133	OJ	OJ	OJ	J	J	J	J	J	J	J	RJS
7.4	242	J	J	J	J	J	J	J	J	J	J	J
13.7	829	J	J	J	J	J	J	J	J	J	J	J

Table 24 Mode Data of EHDA with ethanol (Part 2)

H (cm)
3

d_i (mm)
0.25

d_o (mm)
4

Q (ml/min)	**We**	**Applied Voltage, + dc (kV)**										
		0	**1**	**2**	**3**	**4**	**5**	**6**	**7**	**8**	**9**	**10**
0.1	0.04	D	D	D	D	D	D	SS	SS	SS	CJS	CJS
0.2	0.21	D	D	D	D	D	D	D	SS	SS	SS	SS
0.6	1.4	D	D	D	D	D	D	SS	SS	SS	SS	SS
1.1	4.9	D	D	D	D	D	D	SS	SS	SS	ORS	ORS
2.2	21	D	D	D	D	D	D	SS	SS	ORS	ORS	RJS
2.8	34	D	D	D	D	D	D	SS	RJS	RJS	RJS	RJS
3.9	69	D	D	D	D	D	D	RJS	RJS	RJS	RJS	RJS
5.5	133	D	D	D	D	D	D	RJS	RJS	RJS	RJS	RJS
7.4	242	OJ	OJ	OJ	OJ	OJ	OJ	OJ	J	J	J	J
13.7	829	J	J	J	J	J	J	J	J	J	J	RJS

H (cm)
4

d_i (mm)
0.25

d_o (mm)
4

Q (ml/min)	**We**	**Applied Voltage, + dc (kV)**										
		0	**1**	**2**	**3**	**4**	**5**	**6**	**7**	**8**	**9**	**10**
0.1	0.04	D	D	D	D	D	D	D	SS	SS	SS	SS
0.2	0.21	D	D	D	D	D	D	D	D	SS	SS	SS
0.6	1.4	D	D	D	D	D	D	D	SS	SS	SS	SS
1.1	4.9	D	D	D	D	D	D	SS	SS	ORS	ORS	ORS
2.2	21	D	D	D	D	D	D	SS	SS	ORS	ORS	RJS
2.8	34	D	D	D	D	D	D	SS	DS	RJS	RJS	RJS
3.9	69	D	D	D	D	D	D	RJS	RJS	RJS	RJS	RJS
5.5	133	D	D	D	D	D	D	RJS	RJS	RJS	RJS	RJS
7.4	242	D	D	D	D	D	D	RJS	RJS	RJS	RJS	RJS
13.7	829	J	J	J	J	J	J	J	J	J	J	J

H (cm)
5

d_i (mm)
0.25

d_o (mm)
4

Q (ml/min)	**We**	**Applied Voltage, + dc (kV)**										
		0	**1**	**2**	**3**	**4**	**5**	**6**	**7**	**8**	**9**	**10**
0.1	0.04	D	D	D	D	D	D	DS	SS	SS	SS	SS
0.2	0.21	D	D	D	D	D	D	D	D	SS	SS	SS
0.6	1.4	D	D	D	D	D	D	D	SS	SS	SS	SS
1.1	4.9	D	D	D	D	D	D	D	SS	SS	SS	ORS
2.2	21	D	D	D	D	D	D	SS	SS	ORS	ORS	ORS
2.8	34	D	D	D	D	D	D	DS	DS	RJS	RJS	RJS
3.9	69	D	D	D	D	D	D	DS	DS	RJS	RJS	RJS
5.5	133	D	D	D	D	D	DS	DS	DS	RJS	RJS	RJS
7.4	242	D	D	D	D	DS	DS	DS	RJS	RJS	RJS	RJS
13.7	829	OJ	OJ	OJ	OJ	OJ	OJ	OJ	RJS	RJS	RJS	RJS

Table 25 Mode Data of EHDA with ethanol (Part 3)

H (cm) 0.5

d_i (mm) 1

d_o (mm) 4

Q (ml/min)	We	Applied Voltage, + dc (kV)										
		0	1	2	3	4	5	6	7	8	9	10
0.1	0.00	T	T	T	CJS	CJS	B	B	B	B	B	B
0.2	0.00	T	T	T	CJS	B	B	B	B	B	B	B
0.6	0.01	T	T	T	T	B	B	B	B	B	B	B
1.1	0.02	T	T	T	T	B	B	B	B	B	B	B
2.2	0.08	T	T	T	T	T	CJS/B	B	B	B	B	B
2.8	0.13	T	T	T	T	T	B	B	B	B	B	B
3.9	0.27	T	T	BD	BD	BD	B	B	B	B	B	B
5.5	0.52	T	BD	BD	BD	BD	BD	B	B	B	B	B
7.4	0.94	T	BD	BD	BD	BD	BD	BD	B	B	B	B
13.7	3.24	BD	BD	BD	BD	BD	BD	BD/B	BD/B	B	B	B

H (cm) 1

d_i (mm) 1

d_o (mm) 4

Q (ml/min)	We	Applied Voltage, + dc (kV)										
		0	1	2	3	4	5	6	7	8	9	10
0.1	0.00	TD	TD	TD	TD	SS	SS	CJS	CJS	CJS	OMS	OMS
0.2	0.00	TD	TD	TD	TD	SS	SS	CJS	CJS	CJS	OMS	OMS
0.6	0.01	TD	TD	TD	TD	SS	SS	SS	CJS	CJS	OMS	OMS
1.1	0.02	TD	TD	TD	TD	SS	SS	ORS	ORS	ORS	CJS	CJS/RJS
2.2	0.08	TD	TD	TD	TD	SS	SS	ORS	ORS	RJS	RJS	RJS
2.8	0.13	TD	TD	TD	TD	SS	SS	ORS	ORS	ORS	ORS	RJS
3.9	0.27	TD	TD	TD	TD	SS	SS	J	J	RJS	RJS	RJS
5.5	0.52	TD	TD	TD	TD	J	J	J	J	J	RJS	RJS
7.4	0.94	TD	TD	TD	TD	J	J	J	J	J	J	RJS
13.7	3.24	J	J	J	J	J	J	J	J	J	J	J

H (cm) 2

d_i (mm) 1

d_o (mm) 4

Q (ml/min)	We	Applied Voltage, + dc (kV)										
		0	1	2	3	4	5	6	7	8	9	10
0.1	0.00	D	D	D	D	D	D	SS	SS	SS	CJS	CJS
0.2	0.00	D	D	D	D	D	D	SS	SS	SS	SS	CJS
0.6	0.01	D	D	D	D	D	D	SS	SS	SS	SS	CJS
1.1	0.02	D	D	D	D	D	D	SS	SS	SS	ORS	ORS
2.2	0.08	D	D	D	D	D	D	SS	ORS	ORS	ORS	ORS
2.8	0.13	D	D	D	D	D	SS	SS	ORS	ORS	ORS	ORS
3.9	0.27	D	D	D	D	D	SS	ORS	ORS	ORS	ORS	ORS
5.5	0.52	D	D	D	D	D	D/J	J	J	RJS	RJS	RJS
7.4	0.94	D	D	D	D	D	D	J	J	J	J	RJS
13.7	3.24	J	J	J	J	J	J	J	J	J	J	J

Table 26 Mode Data of EHDA with ethanol (Part 4)

H (cm) 3

d$_i$ (mm) 1

d$_o$ (mm) 4

Q (ml/min)	We	Applied Voltage, + dc (kV)										
		0	1	2	3	4	5	6	7	8	9	10
0.1	0.00	D	D	D	D	D	D	SS	SS	SS	SS	SS
0.2	0.00	D	D	D	D	D	D	D	SS	SS	SS	SS
0.6	0.01	D	D	D	D	D	D	SS	SS	SS	SS	SS
1.1	0.02	D	D	D	D	D	D	SS	SS	SS	ORS	ORS
2.2	0.08	D	D	D	D	D	D	SS	SS	SS	ORS	ORS
2.8	0.13	D	D	D	D	D	D	SS	SS	ORS	ORS	ORS
3.9	0.27	D	D	D	D	D	D	SS	SS	ORS	ORS	ORS
5.5	0.52	D	D	D	D	D	SS	RJS	RJS	RJS	RJS	RJS
7.4	0.94	D	D	D	D	D	SS	RJS	RJS	RJS	RJS	RJS
13.7	3.24	J	J	J	J	J	J	J	J	J	J	RJS

H (cm) 4

d$_i$ (mm) 1

d$_o$ (mm) 4

Q (ml/min)	We	Applied Voltage, + dc (kV)										
		0	1	2	3	4	5	6	7	8	9	10
0.1	0.00	D	D	D	D	D	D	D	SS	SS	SS	SS
0.2	0.00	D	D	D	D	D	D	D	SS	SS	SS	SS
0.6	0.01	D	D	D	D	D	D	D	SS	SS	SS	SS
1.1	0.02	D	D	D	D	D	D	D	SS	SS	SS	SS
2.2	0.08	D	D	D	D	D	D	SS	SS	SS	SS	ORS
2.8	0.13	D	D	D	D	D	D	SS	SS	SS	ORS	ORS
3.9	0.27	D	D	D	D	D	D	SS	SS	ORS	ORS	ORS
5.5	0.52	D	D	D	D	D	D	SS	RJS	RJS	RJS	RJS
7.4	0.94	D	D	D	D	D	D	SS	RJS	RJS	RJS	RJS
13.7	3.24	D	D	D	D	D	D	RJS	RJS	RJS	RJS	RJS

H (cm) 5

d$_i$ (mm) 1

d$_o$ (mm) 4

Q (ml/min)	We	Applied Voltage, + dc (kV)										
		0	1	2	3	4	5	6	7	8	9	10
0.1	0.00	D	D	D	D	D	D	D	SS	SS	SS	SS
0.2	0.00	D	D	D	D	D	D	D	SS	SS	SS	SS
0.6	0.01	D	D	D	D	D	D	D	SS	SS	SS	SS
1.1	0.02	D	D	D	D	D	D	D	SS	SS	SS	SS
2.2	0.08	D	D	D	D	D	D	D	SS	SS	SS	SS
2.8	0.13	D	D	D	D	D	D	D	SS	SS	ORS	ORS
3.9	0.27	D	D	D	D	D	D	SS	SS	ORS	ORS	ORS
5.5	0.52	D	D	D	D	D	D	SS	RJS	RJS	RJS	RJS
7.4	0.94	D	D	D	D	D	D	SS	RJS	RJS	RJS	RJS
13.7	3.24	D	D	D	D	D	DS	DS	RJS	RJS	RJS	RJS

Appendix C. Stability Analysis for EHDA

After Taylor written a series of papers on EHD phenomena, D.A Saville first did the stability analysis for a simplified EHD jet [71] [72]. His model interpreted the reason why Rayleigh instability is suppressed by increasing the electrical field. This phenomenon usually takes place when the electrical field is weak. Many people have been observed it, including our tests.

A. J. Mestel explored the limitation from viscosity with influence from conductivity [73, 74]. He found for low viscous and high conductive fluid, the surface stress caused by surface charge would suppress Rayleigh instability, while for moderate conductive fluid, the charge relaxation instability appears.

With different application background, M. Hohman et al. analyzed the mechanics of electrospining for an intermediate conductive fluid [42, 43]. He considered the influence of viscosity, conductivity, surface charges on stability. And he classified three instability modes, Rayleigh mode, axisymmetric conducting mode and whipping conducting mode. The first and second modes are similar with Saville's and Mestel's mode. And the whipping conducting mode strongly depends on the local electric field near the jet. When it is dominated by its own static charge density, the third instability mode would take over the other two modes.

If we borrow Hohman's theory to our research background, we could find at least three EHDA mode that represent those three instability mode. And some other EHDA modes looks like the transition modes between those three modes.

Rayleigh mode:

$$\varpi^2 = \frac{\sigma}{\rho R_0^3} kR_0 \frac{I_1(kR_0)}{I_0(kR_0)}\left(1-(kR_0)^2\right) \tag{18.9}$$

Axisymmetric conducting mode:

$$\varpi^3 + \varpi^2\left(\frac{4\pi K^*\Lambda}{\delta\sqrt{\beta}} + 3\nu^* k^2\right) + \omega\left[3\nu^* k^2 \frac{4\pi K^*\Lambda}{\delta\sqrt{\beta}} + \frac{1}{2} k^2(k^2-1) + 2\pi\sigma_0^2 k^2\left(\frac{8L}{\delta}-1\right) + \frac{\Lambda\Omega_0^2}{\delta 4\pi}k^2\right]$$
$$+ \frac{4\pi K^*\Lambda}{\delta\sqrt{\beta}}\left[\frac{1}{2} k^2(k^2-1) + 2\pi\sigma_0^2 k^2 + \frac{\delta\Omega_0^2}{\Lambda 4\pi}k^2 + \frac{E_0\sigma_0}{\sqrt{\beta}} ik\left(\frac{1}{L} - 4\right)\right] = 0$$

(18.10)

Whipping conducting mode

$$\varpi^2 = -\frac{3}{4}\nu^*\varpi k^4 - 4\pi\sigma_0^2 k^2 Ln(k) - ik\frac{2\sigma_0\Omega_0}{\sqrt{\beta}} - \frac{ik\Omega_0}{\sqrt{\beta}}(\sigma_0 k^2 + C) - k^2$$
$$+ \left(\Omega_0\left[-\frac{1}{4\pi} + \frac{(\beta+1)k^2}{16\pi\beta}\right] + \frac{ik\sigma_0}{\beta}\right) \times \frac{\sqrt{\beta}}{\beta+2}\left[k^2\sqrt{\beta}\Omega_0 + ik\left(4\pi C + 2\pi\beta\sigma_0 k^2\right)\right] \tag{18.11}$$

$$C = -\frac{ik\frac{2K^*\Omega_0}{\beta+2} + \frac{4\pi\sqrt{\beta}K^*}{\beta+2}\sigma_0 k^2}{\frac{4\pi\sqrt{\beta}K^*}{\beta+2} + \varpi} \tag{18.12}$$

Without surface charge (C = 0, $\sigma_0 = 0$):

$$\varpi^2 = A\nu^*\varpi k^4 - k^2 - \left(\frac{1}{4\pi} - \frac{(\beta+1)k^2}{8\pi\beta}\right)\frac{\sqrt{\beta}}{\beta+2}\Omega_0^2 k^2 \tag{18.13}$$

Without surface charge:

$$\varpi = -\frac{3}{4\nu^{*}k^{2}}\left(1 + 4\pi\sigma_0^{2} Ln(k)\right) \tag{18.14}$$

We could first adopte the axisymmetric conducting mode to verify the EHD effect in ethanol.

Using Mathematic, the stability equation could be numerically solved. The results for both ethanol and water are shown in Fig. 90. Total 6 level of Ω_0 are calculated in order to represent 6 voltage grades. The red curve shows the Rayleigh instability without electrical field, in which $\Omega_0 = 0$, which is agree with the existing solution. The maximum growth rate occurs at k about 0.7. As the electric intensity increasing, that type instability was suppressed. This argument has been proved by Saville and other researchers. Some of our experiment results also support this argument, for example the set of condition in Fig. 91.

Then we compare our results with M. Hohman's results. The two figures are almost exact same, except for k less than 0.2. In our calculation, we found a non-converge spot. By analysis the equation **Error! Reference source not found.**, we notice that that spot is caused by the last term in the equation. The 1/δ should be in form of $\frac{1}{2 - \beta Ln(\chi)k^{2}}$, which has to generate the spot at $k = \sqrt{\frac{2}{\beta Ln(\chi)}}$. This question could be one of our future works. During our testing, we could notice at another type of instability would be strengthened when in electrical field above 4 ~ 6 kV. Following pictures show that the Rayleigh instability is suppressed under 6 kV and then another high frequency instability take the dominant role. According to the Hohman's analysis, it could be the instability of whipping conducting mode. He mentioned that, for dielectric flow with finite surface charges, when $B_1 = \frac{4\pi^2 d^2 \sigma_0^2}{\varepsilon_0} \log k^{-1}$ is larger than $A_1 = \pi d\sigma + \frac{d^2 E_\infty^2 (\beta + 2)}{4}$, the self-repulsion effect would overcome the enhancement of tension due to the applied electrical field. Thus, it causes high frequency instability.

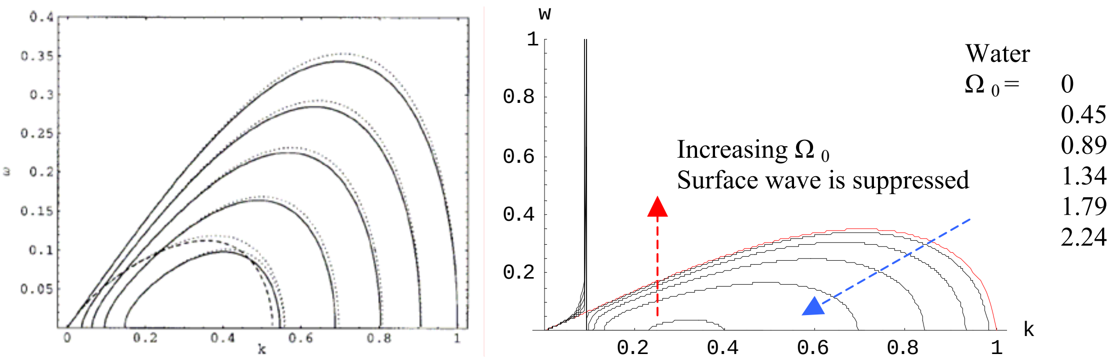

Fig. 90 Compare of M. Hohman's dispersion relation as function of field strength. (β = 77, σ = 0.078, μ = 0.001, K = 0.0001, r_0 = 0.001, H=0.01)

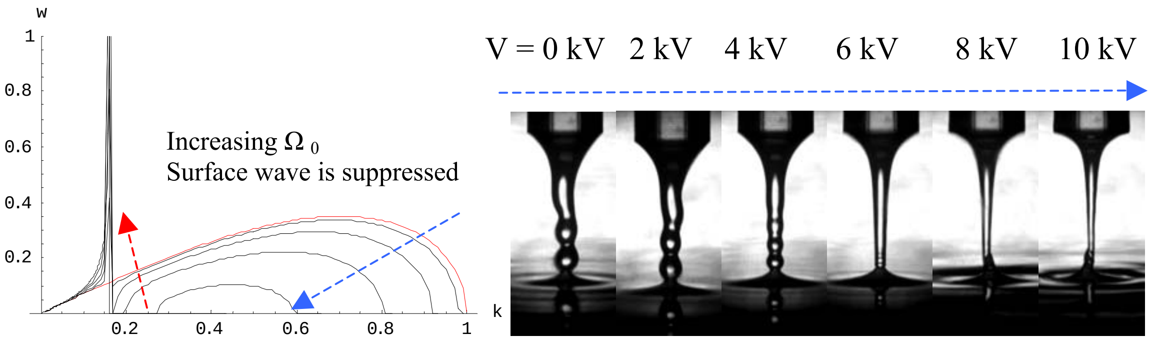

Fig. 91 The Rayleigh instability is suppressed by electric field (Ethanol flow be stabilized by electric field at Q = 13.7 ml/min, Di = 1mm, H = 1cm)

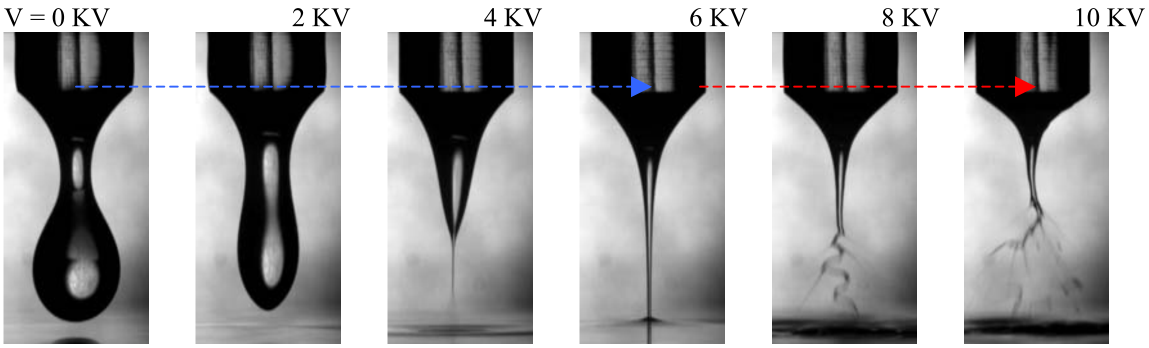

Fig. 92 Ethanol flow be effected by electric field at Q= 3.9 ml/min, Di = 1mm, H=1cm

Appendix D. Micro Jet impingement Cooling on the Structure Surface

D.C. Wadsworth and I. Mudawar [75] studied confined jet impingement cooling. In his testing regime, they found that the large pin-fin surface showed the best cooling performance in their comparison. They also noticed that effect of large subcooling could help to release the vapor buildup on the enhanced surface. According to their results, the CHF on microgroove structure would be higher than that on micro stud.

D. Copeland investigated thin long fins structures for single and two phase cooling [76]. By comparable testing, he found that CHF showed a strong dependence on pin fin ratio (F_{PF} = 1+H/W). The highest CHF he got was on the surface of fins' size of W = 0.1 mm and H = 0.5 mm. In the testing condition, the inlet velocity was from 0.05 to 0.4 m/s. We could found the CHF at the highest flowrate were about 4 times of the CHF at lowest flowrate.

D. Priedeman et al. tested large structured surface under a 7 mm jet impingement [77]. The result showed that higher Nu number could be achieved by increasing H and W and decreasing the fin density. The conclusion conflicted with the result from Copeland, but their testing surface size had a large difference. Relative works on structure surface impinged by jet impinging are summarized in Table 27.

Table 27 Study Jet Impinging on Structure Surface

Group	Fluid	Surface (mm)	Correlation
I. Mudawar D.E. Maddox [78]	FC-72 Parallel flow	W_S: 0.305 L_S: 0.305 H_S: 0.25,0.51, 1.02,11.7 D: 12.7	$\frac{q''_m}{\rho_v H_{fg} u_e} = C1\left(\frac{\rho_l}{\rho_v}\right)^{15/23}\left(\frac{\sigma}{\rho_l u_e^2 L}\right)^{8/23}$ $\left(1+\frac{Cp\Delta T_{sub}}{H_{fg}}\right)^{7/23}\left(1+C_{sub}\frac{\rho_l}{\rho_v}\frac{Cp\Delta T_{sub}}{H_{fg}}\right)^{16/23}$
D. Priedeman, V. Callahn, B.W. Webb [77]	Water, FC-77 dn: 7mm	W: 0.8, 1.59 L: 0.8, 1.59 H: 1.59, 3.18 Heater S=2.9 cm^2	Best structure (Stud): 1) W = 1.59, H/W = 2, W/L =1 2) W = 0.8, H/W = 4, W/L =1 3) W = 0.8, H/W = 2, W/L =1 Worst structure: W/L = 0.5
D.C. Wadsworth I. Mudawar [75]	FC-72 Confined slot jet	W: 0.305 L:0.305 H:1.02 1.61 cm^2 D: 12.7mm	Two phase: Microgroove is better in such confined jet, the CHF enhancement is less than area ratio. CHF=411W/cm^2@12.9m/s
D. Copeland 1994 [76]	FC-72 dn: 1,2 Confined jet	W: 0.1, 0.2 L:0.1,0.2 H:0.1~1 S=1 cm^2	Two phase: $q''_{CHF} = 58Q^{0.51}Ar^{0.35}W^{-0.02}$ CHF=369W/cm^2@0.4m/s (10cm^3/s) Best structure (Stud): 1) W =0.1, H/W = 5, W/L =1 2) W =0.2, H/W = 5, W/L =1 3) W =0.2, , H/W = 2.25, W/L =1 Worst structure: W =0.2, H/W = 1, W/L =1
Eric A. Silk [13]	2-2 Swirl nozzles Spray	W =1 H =1 L =1 S=1 cm^2	Straight fins surface is the best compare with Cubic and Pyramid surface, CHF=1.4MW/m^2 @ θ=30º,γ=90º. Drainage could cause the fluid column existing at the surface center.

In order to study the effect of structure surface, single and multi MJIC experiments are carried out with ethanol. The tests with structure surface are conducted in atmosphere pressure. From CHF results and high speed images, shown in Fig. 93, we observed the following. By using structured surface at flowrate greater than $2.7 \cdot 10^{-7}$ m3/s, the CHF enhancement was 45% for the jet array and 28% for the single jet.

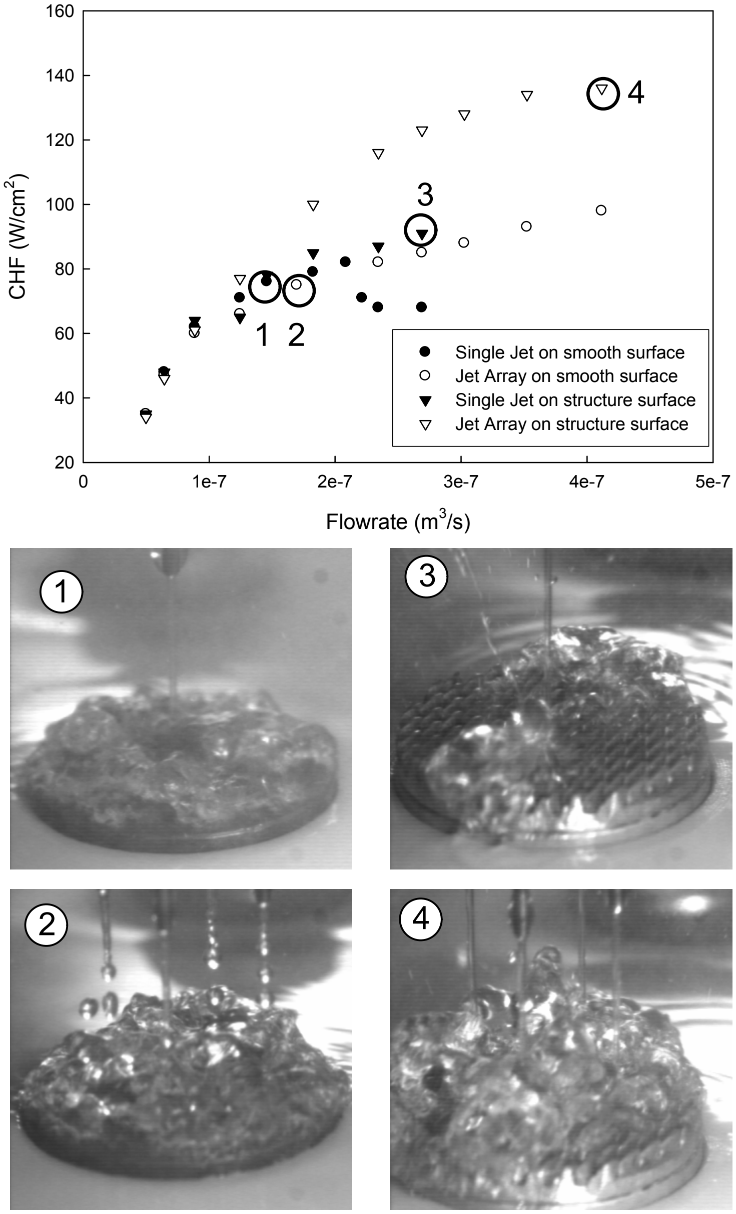

Fig. 93 Effect of surface condition during single and multi MJIC with ethanol